UNIVERSITY OF OKLAHOMA

GRADUATE COLLEGE

STUDY OF ADVANCED RESONANT PHOTONIC GRATINGS IN THE MID-INFRARED SPECTRUM FOR THE CHEMICAL SENSING APPLICATIONS

A DISSERTATION

SUBMITTED TO THE GRADUATE FACULTY

in partial fulfillment of the requirements for the

Degree of

DOCTOR OF PHILOSOPHY

By

TAHERE HEMATI

Norman, Oklahoma

2023

Downloaded from SHAREOK. Persistent Handle URL: https://hdl.handle.net/11244/338849

STUDY OF ADVANCED RESONANT PHOTONIC GRATINGS IN THE MID-INFRARED SPECTRUM FOR THE CHEMICAL SENSING APPLICATIONS

A DISSERTATION APPROVED FOR THE
SCHOOL OF ELECTRICAL AND COMPUTER ENGINEERING

BY THE COMMITTEE CONSISTING OF

Dr. Binbin Weng, Chair

Dr. Hjalti Sigmarsson

Dr. Zhisheng Shi

Dr. Patrick McCann

Dr. Michael Santos

© Copyright by TAHERE HEMATI 2023
All Rights Reserved.

To my parents and the love of my life, Peyman.

Acknowledgments

First and foremost, I am extremely grateful to my research advisor Dr. Binbin Weng for his continuous support. His immense knowledge, patience, and plentiful experience have always encouraged me in my academic research journey. I could not have imagined a better advisor and mentor.

I would also like to thank my committee members Dr. Zhisheng Shi, Dr. Patrick McCann, Dr. Hjalti Sigmarsson, and Dr. Michael Santos, for their valuable expertise, kind help, and support in advising my dissertation. I am appreciative of their insightful comments and perspectives.

I am grateful for the financial support from Oklahoma Center for the Advancement of Science and Technology (OCAST), OU Graduate Collage (OU Alumni Graduate Fellowship), and Gallogly College of Engineering (Clyde L Farrar Scholarship, William H Barkow Scholarship, Nettie Vincent Boggs Scholarship, Thomas I Brown Jr Scholarship, PH robinson Fellowship, Farzaneh Scholarship, and Dissertation Excellence Award), and School of Electrical and Computer Engineering (Journal Paper Awards). My appreciation also goes out to the staff members at the School of Electrical and Computer Engineering (ECE), especially Dr. Rodney C. Keele, for his kind help. I would like to extend my sincere appreciation to the research scientists at the Noble Microscopy Lab for their support in material characterization. Their expertise and assistance have played a vital role in the success of my research. Additionally, I am grateful

to the scientists at the MREC cleanroom for their training and support in device fabrication and characterization. Their guidance has been invaluable in developing my skills in this area. I would like to offer my special thanks to all my friends for being an enduring source of support and strength.

I would like to thank my family for their endless support and tremendous sacrifice over the past few years. None of this work would have been possible without them. My gratitude to them is beyond words.

Finally, I would like to thank the love of my life, Peyman Hekmatpour, for his endless love and support throughout these years. This accomplishment would not have been possible without his unwavering support and belief in me.

Table of Contents

Acknowledgments **v**

Abstract **xix**

1 Introduction **1**

2 Theoretical Background **8**

2.1 High Contrast Gratings (HCGs) 8

2.1.1 Analytical Solutions 10

2.1.2 Phase Selection Rules 18

2.2 Parity-time (PT)-Symmetric Systems 25

2.2.1 PT-Symmetry and PT-Symmetry Breaking 28

2.2.2 PT-Symmetry In Photonics 30

3 Mid-IR Photodetector Engineering Via Photonic Gratings **41**

3.1 Results and Discussion 46

4 Photonic Gratings Enhancing Light-Absorption in a Miniaturized Gas Sampling Cell **54**

4.1 SHCG Enabled Light-Absorption in Gas Sampling Cell 56

4.2 CHCG Enhanced Light-Absorption in Gas Sampling Cell 60

5 PT-Symmetry Photonic Gratings for Enabling Nontrivial Light Sources **65**

5.1 Theory and Analytical Solutions 68

5.2 Numerical Simulations 74

6 Lead-Selenide-based Mid-Infrared Material Engineering **83**

6.1 Introduction of Deposition Mechanism 85

6.2 Experimental Setting 87

6.3 Results Analysis and Discussion 89

6.4 New Growth Model Discussion 100

7 Experimental Investigation of the Large-Area Patterning Method for Grating Fabrication **104**

7.1 Sample Prepration 104

7.2 Experimental Settings 106

7.3 Laser Interference Lithography (LIL) Patterning Method 108

7.4 Optimization of the RIE Dry Etching Method 111

7.4.1 Ion Charging Effect to Improve RIE Etched Profile 113

8 Conclusion and Future Works **121**

Appendix **153**

List of Figures

1.1 The absorption fingerprint of some typical trace gas molecules in the Mid-IR range [5]. 1
1.2 Schematic view of conventional optical sensors. 2
1.3 Schematic view of the used nanophotonic structures such as WGM, HCG, PhCs resonators, and plasmonic NPs for downsizing Mid-IR sensors [17]–[20]. 4

2.1 Schematic view of three operation regimes in optical gratings, including diffraction, near-wavelengths, and sub-wavelengths regimes. 9
2.2 Schematic cross-sectional view of an HCG, showing three divided regions. z=0, and z=D are input and output planes, respectively. **a**, **s**, and Λ are grooves' width, bars' width, and the grating period, respectively. 10
2.3 Dispersion curves of TE/TM-polarized, surface-normal incidence HCG, exciting four even modes. The air and dielectric light lines are displayed by gray dash lines. *a*, *b*, and *c* indicates cutoff frequencies [43]. 15

2.4 **a)** Reflectivity contour map of a TE-polarized, surface-normal incident light to an HCG. The checkerboard pattern is created via changing grating thickness over wavelengths, indicating three operation regimes. **b)** Analytical solutions of FP resonance conditions (2.23) plotted on the contour map (solid white lines). A zoomed-in view of crossing and anti-crossing points are shown as well. 19

2.5 Two-mode cancellation at the output plane of the HCG resulting 0% transmissivity and 100% reflectivity (dash black lines). Pink and red curves show the amplitude of the zero-order and second-order modes, respectively. The blue curve indicates the phase difference between these two modes at different wavelengths [43]. 22

2.6 Intensity profile inside the grating at the crossing and anti-crossing points. The anti-crossing point indicates 10^6 intensity enhancement, compared to the crossing point. 23

2.7 **a)** Reflection spectrum, exhibiting three dramatic changes at 2.18, 2.35, and 2.45 (Λ). **b)** Satisfied HCG resonance condition. The mode positioned at 2.18 (Λ) indicates the closest value to zero. **c)** Q-factor value of two different supermodes. The blue curve is related to the shown reflection spectrum, while the reflection spectrum of the pink curves has not been plotted. In comparison, the Q_1 is dominant [43]. 24

2.8 **a)** Schematic view of a PT-coupled waveguide (green and yellow parts represent gain and loss respectively). **b)** Complex refractive index profile (blue and red curves, stand respectively for real and imaginary parts) [61]. 27

2.9 Intensity profile of the **a)** suppressed mode and **b)** amplified mode in a 1D structure. Intensity profile of the **c)** amplified mode in a 2D structure [72]. 33

2.10 **a)** Schematic illustration of the PT-symmetric laser. Distributions of the electric field intensity, where **b)** modes are evenly confined in the gain and loss (PT-Symmetry), and **c)** modes are mostly confined in the gain part (broken PT-Symmetry) [85]. 34

2.11 **a)** Emission spectrum of a single microring, exhibiting the multi-mode operation. **b)** Emission spectrum of a PT-symmetric two coupled microrings, exhibiting the single-mode operation [62]. . . 35

2.12 Schematic view of **a)** an active PT-symmetric [87] Bragg reflector and **b)** a passive PT-symmetric Bragg grating [88]. **c)** In the passive grating, the incident light from forward shows no reflection from the hand above the structure. However, the entering wave from backward experiences enhanced reflection and shows the hand pattern [88]. 36

2.13 Frequency splitting of a Hermitian (red line) and non-Hermitian (blue line) system according to the perturbation strength [96]. . . 39

3.1 Schematic view of diffracted waves from a grating structure. . . . 46

3.2 Schematic view of a PbSe photoconductive detector with the integration of the grating structure under normal incidence. . . . 47

3.3 **a)** Changing pattern of transmission according to manipulating lattice period, **b)** Changing pattern of transmission according to manipulating fill factor. 48

3.4 **(a)** Transmission comparison of the Mid-IR photodetector device with and without the optimized grating structure under the PbSe thin film, **(b)** Reflection and transmission spectra of the grating reflector in logarithm scale. (Note: the simulated light is of TM polarization) 49

3.5 Comparison between absorption value with and without the grating structure as the reflector (PbSe thickness=1.26 μm). 50

3.6 Comparison between reflection value when I use the grating structure and silver as the reflector (PbSe thickness=1.26 μm), normal incidence. 50

3.7 Comparison between absorption value with and without the grating structure (Λ=2.4, F=0.49, d_1=1.48 μm, d_2=1.26 μm), TM polarization under normal incidence. 52

4.1 **a)** 3D schematic view of the SHCG, made of silicon with SiO_2 substrate (relative to the grating thickness, the substrate thickness is infinite). **b)** Cross-sectional view of the SHCG. The grating layer thickness D_1, the fill factor F, and the grating period Λ are demonstrated in the figure. 57

4.2 **a)** Changing pattern of the light-absorption given by manipulating the period. The optimized period $\approx$ 4.3 μm. **b)** Changing pattern of the light absorption given by manipulating the fill factor. The optimized fill factor $\approx$ 0.57. 58

4.3 **a)** Absorption spectra of CO_2 with and without SHCG from 4.29 μm to 4.31 μm. (Λ=4.336 μm, F=0.5775, and D_1=1.832 μm). The bandwidth of absorption peak=1.2 nm. **b)** Intensity and distribution of the confined electric field at 4.3 μm on the SHCG. The colored bar shows the intensity of the electric field. unit $(V/\mu m)^2$. 59

4.4 **a)** 3D schematic view of the CHCG, made of silicon with SiO_2 substrate. **b)** Cross sectional view of the HCG. The bottom grating layer thickness D_1, the air gap thickness D_2, the top grating layer thickness D_3, the substrate thickness T, the fill factor F, and the grating period Λ are shown in the figure. This structure is supposed to be located in the gas chamber. 61

4.5 **a)** Absorption spectra of CO_2 with and without CHCG from 4.29 μm to 4.31 μm; D_1=1.832 μm, D_2=1.14 μm, D_3=1.55 μm, T=infinite, Λ=4.336 μm, and F=0.5775. The bandwidth of absorption peak=0.25 nm. **b)** Intensity and distribution of the confined electric field at 4.3 μm on the CHCG. The colored bar shows the intensity of the electric field. unit $(V/\mu m)^2$. 62

4.6 **a)** Absorption spectra of CO_2, given by optimization CHCG with a finite substrate, from 4.29 μm to 4.31 μm D_1=0.99 μm, D_2=1.15 μm, D_3=1.215 μm, T=1.149 μm, Λ=3.6378 μm, and F=0.5325. The bandwidth of absorption peak=0.1 nm. **b)** Comparison between the absorption value of SHCG, CHCG with an infinite substrate, and CHCG with finite substrate. **c)** Intensity and distribution of the confined electric field at 4.3 μm on the CHCG with the finite substrate. The colored bar shows the intensity of the electric field. unit $(V/\mu m)^2$ 63

5.1 **a)** Real and imaginary parts of a PT-symmetric RI modulation in the x-direction. **b)** Real RI modulation in x- and z-direction. . . 69

5.2 **a)** Real part and, **b)** the imaginary part of eigenvalues according to the γ for a system with the periodicity of 2 μm. The exceptional point is shown by the dashed gray line. 73

5.3 **a)** Real and, **b)** the imaginary parts of eigenvalues according to the period for a PT-symmetric grating. The exceptional point is shown by the dashed gray line. 74

5.4 **a)** 3D schematic of the PT-symmetric gratings; **b)** Cross-sectional schematic of the grating, showing three divided regions: the upper-half vacuum region, the grating region, and the lower-half substrate region. Λ, a, and s are the grating period, gap, and bar width. . . 75

5.5 Electric-field distribution over the PT-symmetric grating where **a)** $\gamma = 0.2$, associated with the symmetry phase. **b)** $\gamma = 0.22$ associated with the symmetry-broken phase (amplified mode). **c)** $\gamma = 0.22$ associated with the symmetry-broken phase (suppressed mode). 76

5.6 **a)** Total transmitted spectra over wavelengths from the grating with $\gamma = 0.18$ (the black dotted line), $\gamma = 0.2$ (the red dashed line), and $\gamma = 0.22$ (the solid blue line), in the logarithm scale. The amplitude distribution of the spectrum with $\gamma = 0.2$ and $\gamma = 0.22$ is displayed over one grating period in the inset. The transmitted emission coefficient map over wavelengths where γ changes from 0 to **b)** 0.18, **c)** 0.2, and **d)** 0.22. 79

5.7 Q-factor of the resonance mode in the logarithm scale with different introduced gain/loss (γ) to the grating. 81

6.1 Location of the substrate in the final solution. 87

6.2 Top-view SEM images of the PbSe thin film deposited by **a)** a poly-crystalline high-temperature bath deposition (IBI); **b)** a low-temperature quantum dots deposition (Cluster); **c)** the oriented-attachment growth mechanism. The appearance of the given films is shown beneath each growth method. 89

6.3 **a)** Top-view SEM image of the PbSe thin film deposited by the IBI mechanism. **b)** Kikuchi pattern, diffracted from sample (a). **c)** EBSD orientation map of sample (a), taken on a 5×5 μm^2 grid. **d)** Top-view SEM image of the PbSe thin film deposited by the OA mechanism. **e)** The Kikuchi pattern, diffracted from sample (d). **f)** EBSD orientation map of sample (d), taken on a 5×5 μm^2 grid. Insets show a 3D view of (100)-oriented NCs (red cube), and (111)-oriented NCs (blue cube). . . 91

6.4 **a)** Reflection of the IBI-grown sample in the Mid-IR optical range. **b)** Reflection of the OA-grown sample in the Mid-IR optical range. **c)** Normalized PL emissions given by OA and IBI samples. 92

6.5 **a)** Plot of the growth rate as a function of growth time, labeled by three different growth mechanisms. Top-view SEM imaging of the films deposited at 45°C, pH∼10, for **b)** 3 minutes; **c)** 6 minutes; **d)** 20 minutes. 93

6.6 Top-view SEM imaging of **a)** the successively grown film deposited at 30°C, pH 9.9, (7 runs, each run 8 minutes); **b)** the deposited film at 30°C, pH 9.9 for 60 minutes, 1 run. 95

6.7 Top-view SEM imaging of the film deposited at 40°C, for 10 minutes, when **a)** added NaOH=0.4 M; **b)** added NaOH=0.3 M; **c)** added NaOH=0.2 M. 95

6.8 Top-view SEM imaging of the film deposited at 45°C, pH∼9.8, for ten minutes when the preparation temperature is **a)** 55°C, **b)** 60°C, and **c)** 65°C . **d)** The plot of size-dependent PL peak position of the deposited films. 97

6.9 **a)** SEM image of the cluster-based film. **b)** X-ray diffraction patterns of sample (a). **c)** SEM image of the IBI-based film. **d)** X-ray diffraction patterns of sample (c). **e)** SEM image of the OA-based film. **f)** X-ray diffraction patterns of sample (e). 99

6.10 Steps of the suggested growth model for the unique OA growth on the glass substrate; **a)** Forming lead hydroxide in the Se-free solution. **b)** Bonding lead hydroxide with the oxygen-terminated glass. **c)** Starting the Selenization process. **d)** Forming a seed layer of orthorhombic PbSe NCs. **e)** Synthesizing pyramidal-shaped NCs on top of the seed layer by IBI growth. **f)** Synthesizing OA NCs from (100) faces of pyramidal facets. 101

7.1 Numerical simulation of FWHM changes due to the introduced roughness (RMs). 10 nm, 20 nm, 30 nm, 40 nm, and 50 nm are introduced. 105

7.2 **a)** SEM photo and **b)** AFM photo of the OA-deposited sample. **c)** 3D view of the sample (a) taken on a 0.75×0.75 μm^2 surface. . . . 106

7.3 Schematically view of Lloyd's mirror interferometer. 109

7.4 **a)** AFM photo of the grating pattern under 15.6 mJ/cm^2 exposure dose. **b)** AFM photo of the grating pattern under 31.2 mJ/cm^2 exposure dose. **c)** AFM photo of the grating pattern under 62.4 mJ/cm^2 exposure dose. 109

7.5 **a)** Trend of fill factor changes under different exposure doses. **b)** Grating period size for 10°, 13°, and 15° rotating angle. 110

7.6 **a)** SEM photo of the etched profile of a grating with 200 W RF power and 15 mTorr process pressure. **b)** SEM photo of the etched profile of a grating with 350 W RF power and 25 mTorr process pressure. The RIE was performed in CH_4/H_2/Ar plasma atmosphere with the ratio of 10/10/5, respectively. Insets show a higher magnification of each grating. 112

7.7 **a)** Tilted SEM image of the etched profile of a grating with a slot width of 4 μm. The inset shows a 2D profilometry view of this grating. **b)** Tilted SEM image of the etched profile of a grating with a slot width of 2.1 μm. The inset shows a 2D profilometry view of this grating. The reference line is displayed by a solid yellow line at the grating area. 114

7.8 Plot of the etching rate according to slot width changes in grating structures. The blue circles are related to the grating with no metallic layer. The red circle shows the accelerated etching rate due to the introduced metallic layer (Cu) for narrow-slot gratings. The arrows show that by increasing the etching rate, the etch profile improves. 115

7.9 **a)** 2D schematical view of the etched profile of a PbSe grating showing the ion-focusing effect resulting in the rounded shape of the trench's bottom. **b)** Numerical simulation of the potential contour map in the slot in a grating. The colored bar shows the potential values of the counter map [218]. 116

7.10 **a)** Tilted SEM image of the etched profile of the grating without a Cu layer. The inset shows a zoomed-in view. **b)** Tilted SEM image of the etched profile of the grating with 70 nm of Cu layer. The inset shows a zoomed-in view. 118

8.1 Schematic view of the PT-symmetry grating. 127

8.2 Gas sensors' development and their global market [222]. 129

Abstract

This dissertation focuses on developing advanced Mid-IR optical devices for chip-scale chemical sensing. Various Mid-IR techniques based on Beer-Lambert's law offer valuable insights into molecular interactions but suffer from bulkiness and high cost. Towards the compact and cost-effective sensing purpose, many efforts have been made in light sources (e.g., QCLs), photodetectors (e.g., PbSe, MCT detectors), and gas sampling chambers via on-chip photonic waveguides. Despite the progress achieved through these new technologies, there is still plenty of room for enhancing the performance and cost-effectiveness of miniaturized Mid-IR gas sensing systems.

Thus, this dissertation explores new photonic engineering pathways to address existing challenges through on-chip integration and downsizing in three core mid-IR gas sensing components, including the light source, detector, and interaction path. In this dissertation, a simple yet versatile and powerful resonant grating platform has been utilized as the foundation to develop innovative engineering methods. Herein, due to the nontrivial properties of High Contrast Gratings (HCGs), such as broadband reflectivity, and high Q factor resonance, I focus mostly on these types of grating resonators.

Through a new design, HCGs are used to enhance absorption in uncooled PbSe-based photodetectors. Moreover, for shrinking the interaction path, a high Q factor HCG resonator was designed, showing 600 times light absorption

enhancement in a micro-size path length. Furthermore, integrating active HCGs with Parity-Time (PT) symmetry concept offers near-zero bandwidth photonic resonant emission with application in Mid-IR light sources. Besides the exploration of new photonic design methods, another important aspect of this work has been focused on the development of a suitable mid-IR material platform to allow the implementation of the aforementioned photonic design methods.

Specifically, a modified chemical deposition method is used to synthesize Oriented-Attached (OA) PbSe nanocrystals (NCs) on amorphous substrates with strong quantum confinement and broad size-tunability. This optimized and cost-effective growth technique demonstrates promising illumination in the Mid-IR range, contributing to the potential of OA PbSe NCs synthesized by this novel method as a material for fabricating Mid-IR photonic components. At the end of this dissertation, an experimental exploration of a low-cost and large-area patterning nanofabrication method is also presented as an extended effort from the core photonic design and novel material synthesis works towards the overarching goal to develop smaller, cost-effective, and efficient on-chip mid-IR optical devices for chemical sensing applications.

Chapter 1

Introduction

The Mid-IR spectral region covers wavelengths from 2 to 20 μm, which also contains two atmospheric transmission windows of 3-5 μm (known as mid-wave infrared) and 8-12 μm [1] (known as long-wave infrared). These atmospheric windows are significant for various applications in thermal imaging (night vision, surveillance, and industrial inspection) [2], and free space communications [3]. The Mid-IR region, often referred to as the molecular fingerprint region, encompasses the fundamental and distinctive molecular vibration modes of numerous chemical molecules like CO_2, CO, and CH_4. This characteristic makes it a crucial wavelength range for diverse applications in different areas, such as medical diagnosis, environment protection, and industrial process control [4].

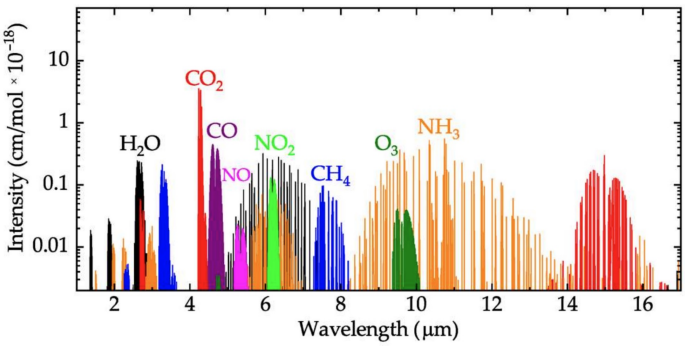

Fig. 1.1: The absorption fingerprint of some typical trace gas molecules in the Mid-IR range [5].

Figure 1.1 shows the Mid-IR fingerprint of a list of important gas species. The unique absorption arises due to gas molecules' characteristic vibrational modes. These modes correspond to specific energy levels, and when exposed to Mid-IR radiation, the molecules selectively absorb photons at frequencies that match their vibrational transitions. The precise wavelengths at which absorption occurs serve as the gas's "fingerprint," enabling the development of highly sensitive and selective gas sensing techniques.

Various Mid-IR techniques have been explored through interacting light with molecules, mainly based on Beer-Lambert's law. This law describes the relationship between the concentration of an absorbing species in a sample and the amount of light it absorbs [6]. Figure 1.2 displays a schematic view of conventional optical sensors. Usually, mirrors are used to increase the interaction path.

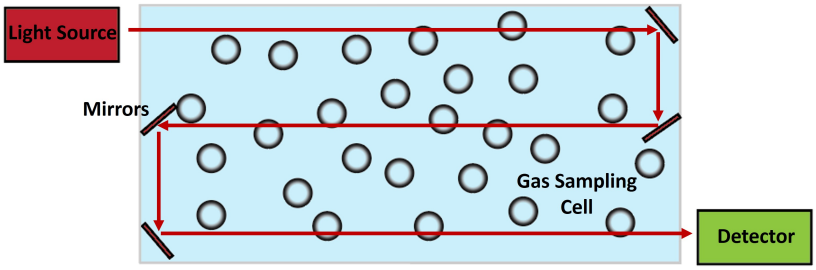

Fig. 1.2: Schematic view of conventional optical sensors.

According to Beer-Lambert's law, the absorbance of a solution is directly proportional to the concentration of the absorbing species and the interaction path length of the sample. A light source emits a specific wavelength of light, which then transmits through the sample. A detector on the other side of the sample measures the intensity of the transmitted light. By comparing the intensity of the transmitted light with the intensity of the incident light, the

absorbance can be calculated. To determine the concentration of the analyte, a calibration curve is typically constructed using samples with known concentrations of the substance.

Fourier Transform Infrared Spectroscopy (FTIR) [7], Attenuated Total Reflectance (ATR) [8], Laser-Induced Breakdown Spectroscopy (LIBS) [9], and Cavity Ring-Down Spectroscopy (CRDS) [10] are some examples of Mid-IR techniques that offer valuable insights into molecular interactions. These techniques, due to their high stability, selectivity, and sensitivity, are increasingly being used in our lives today. However, improving the sensor's performance has led to generally bulky and expensive systems.

Along with emerging technologies such as the Internet of Things (IoT), sensing device miniaturization is considered a global trend for future industries. In recent years, numerous efforts have been made to develop a transformative and low-cost on-chip Mid-IR sensor in the three core parts, shown in figure 1.2, (the light source, the interaction length, and the detector). For instance, using Quantum Cascade Lasers (QCL) as compact, semiconductor-based laser sources indicating wide wavelength coverage, high output power, narrow linewidth, and high tunability enables portable and handheld Mid-IR spectroscopy instruments [11]. Moreover, PbSe-based detectors indicating suitable performance at room temperature and compatibility with low-cost fabrication methods can significantly reduce the cost and size [12]. Small-size Mercury Cadmium Telluride (MCT) Quantum Dots (QDs) offering enhanced sensitivity and wide wavelength range can be another candidate for downsizing chemical sensors [13].

Furthermore, advanced nanophotonic structures recently offer enhanced sensitivity and miniaturization. For instance, plasmonic nanosensors based on metal nanoparticles or nanohole arrays exhibit strong light-matter interactions,

enabling label-free detection of gases. Similarly, Photonic Crystal (PhC) resonators, Whispering Gallery Mode (WGM) resonators, and optical gratings with engineered light confinement have demonstrated enhanced sensitivity to specific gas molecules, including CO_2, NH_3, and nitrogen dioxide NO_2 [14]–[16]. Figure 1.3 shows some used nanophotonic technologies for chemical and gas sensing.

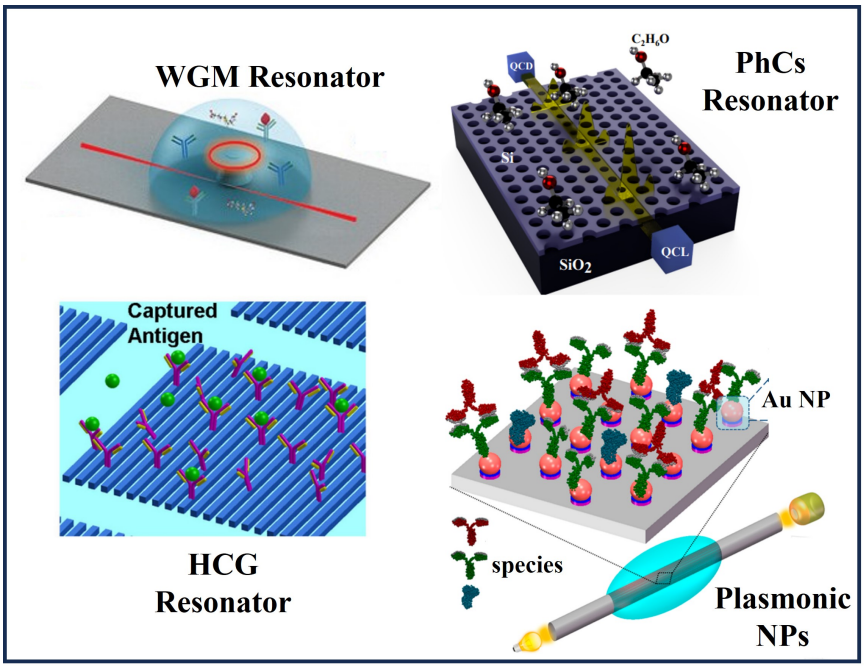

Fig. 1.3: Schematic view of the used nanophotonic structures such as WGM, HCG, PhCs resonators, and plasmonic NPs for downsizing Mid-IR sensors [17]–[20].

While significant progress has been made in downsizing core components in the Mid-IR sensing system, several challenges still need to be addressed to achieve truly low-cost, small-size, and high-performance Mid-IR gas sensors. For instance, finding materials compatible with Mid-IR wavelengths that can be integrated into compact sensor systems is challenging. Additionally, while QCLs have significantly advanced Mid-IR spectroscopy, further improvements are needed to enhance cost-effectiveness. Thus, there is room to improve the small size and low weight, power

consumption, and cost (SWaP-C) sensor devices.

Therefore, in this dissertation, I aim to address some existing obstacles and limitations in light sources, interaction paths, and detectors of optical sensors toward the realization of fully integrated Mid-IR on-chip sensors. To achieve this goal, I use a simple and straightforward one-dimensional resonant photonic gratings structure which is also known as High Contrast Gratings (HCGs). HCGs are periodic structures consisting of alternating layers with high and low refractive indices to manipulate light propagation efficiently [21]. The physical mechanism and properties of HCGs will be discussed in detail in Chapter 2. In this dissertation, I numerically design and optimize three HCG structures, each serving for developing different parts of Mid-IR sensors, including the light source, the interaction path, and the detector. Chapter 3 focuses on designing a passive HCG structure to enhance the performance of room-temperature PbSe-based uncooled photodetectors in the Mid-IR range. I design and optimize a broadband HCG reflector to enhance absorption, particularly in weak absorbing energy band-tail. This offers decent performance at its cut-off band-edge area with no need for an additional cooling system [22].

In Chapter 4, the numerical simulations show the impact of the high-quality-factor HCG cavity in improving light-matter interaction in a shortened length path. In this study, I use CO_2 as a sample gas. Results show that compared to a system where no HCG has been involved, the light absorption increased 600 times. These promising results show the potential of HCGs to shrink the interaction path [23].

Then in Chapter 5, I propose a fundamental concept in quantum physics named Parity-Time (PT) Symmetry and indicate that integrating active HCGs with the PT-Symmetry concept can lead to a nontrivial single mode and

near-zero bandwidth photonic resonant emission benefiting the integration of the light source to a monolithic substrate [24]. The PT-Symmetry theory has already been developed in Chapter 2. The primary method used for simulations is the Rigorous Coupled-Wave Analysis (RCWA), which allows a full vectorial solution of Maxwell's equations in a Fourier domain.

After presenting novel simulation designs for photonic gratings and indicating the potential of HCGs in developing different parts of Mid-IR sensors, I will discuss the potential materials to fabricate the designed structures in Chapter 6. Indium Antimonide (InSb), Indium Gallium Arsenide (InGaAs), and Lead Selenide (PbSe) are known materials operating in the Mid-IR spectrum. Among these materials, PbSe Nanocrystals (NCs) showing strong quantum confinement, the broad size-tunability of the bandgap energies, large Bohr radius, low Auger recombination rates, and proper room-temperature performance can be promising candidates for fabricating Mid-IR sensors. Therefore, here a simple and low-cost chemical deposition method named Chemical Bath Deposition (CBD) is introduced. Moreover, three different chemical deposition methods (cluster, Ion-by-Ion (IBI), and Oriented Attachment (OA)), leading to different morphology and photoluminescence (PL) properties, will be discussed [25], [26]. In the end, the ultimate deposition method, which addresses the limitation of the common OA growth method, is selected to deposit high-quality thin films of PbSe NCs [27].

In Chapter 7, to extend the major efforts on design and material preparation, I further explore using a low-cost photonic patterning method called Laser Interference Lithography (LIL) which allows fast and on-chip large-area patterning. In addition, I also investigate the dry-etching method on the PbSe material using the Reactive-Ion-Etching (RIE) method, which is known to be

challenging due to the low volatile nature of the Pb compound that etching gas can form with, to which a novel solution to address the charging effect on the RIE-etched profile is introduced to achieve a smooth etched profile. In the end, I summarize the performed studies and discuss research gaps to show potential directions for future works in Chapter 8.

Overall, this dissertation aims to overcome challenges in light sources, interaction paths, and detectors of Mid-IR optical sensors to achieve fully integrated on-chip sensors. By leveraging HCGs, novel material synthesis methods, and advanced fabrication techniques, the dissertation contributes to the development of smaller, more efficient, and cost-effective Mid-IR sensor devices for chip-scale chemical sensing applications.

Chapter 2

Theoretical Background

In this section, I discuss the underlying physics of HCGs and present analytical and numerical solutions for visualizing HCG spectral response to Transverse Electric (TE) and Transverse Magnetic (TM) polarized light. Herein, I introduce the phase selection rule and explain how this rule can benefit us in designing broadband reflectors, absorbers, and filters. Moreover, I discuss the PT-Symmetry concept in a separate section and elaborate on the importance of this concept in the realization of novel optical phenomena, including single-mode lasing, asymmetric diffraction, and directional emission. In fact, this chapter builds a foundation for understanding the underlying mechanisms and physics of the designed and fabricated structures in the following chapters.

2.1 High Contrast Gratings (HCGs)

Optical gratings are one of the well-known optical components in optoelectronic areas. They attracted special attention due to their applications in various areas, including spectroscopy [28], telecommunications [29], astronomy [30], and sensing [31]. By optimizing grating parameters, including the period, thickness, and fill factor, I can modulate the amplitude and phase of the incident wave for various light manipulation purposes, including optical filters [32], reflectors [22],

[33], absorbers [34], and resonators [23], [35]. Based on the relative length of the grating period (Λ) and operation wavelengths (λ), they can be categorized into three regimes; i: diffraction regime ($\Lambda \gg \lambda$) [36], [37], ii: Near-wavelengths (N-WL) regime ($\lambda \approx \Lambda$) [38], [39], and iii: Sub-wavelengths (Sub-WL) regime ($\lambda \gg \Lambda$) [40], [41]. Figure 2.1 shows these three regimes. Near-wavelength HCGs are designed by disturbing low and high-refractive index materials in a periodic manner. For instance, SiO_2 and air are commonly used as low-index materials, and group IV and III-V materials are chosen as high-index materials [22], [42].

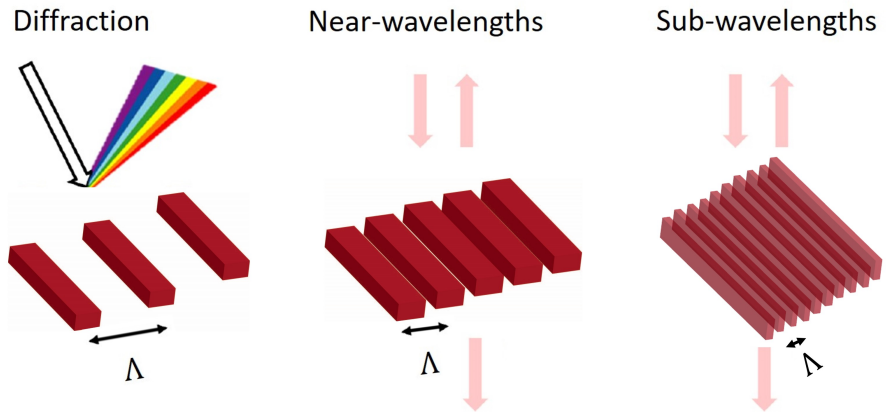

Fig. 2.1: Schematic view of three operation regimes in optical gratings, including diffraction, near-wavelengths, and sub-wavelengths regimes.

The unique phase selection rule in HCGs leads to extraordinary phenomena such as ultra-broad-band high reflectivity or transmissivity and high-quality factor resonance [43], [44]. The broad-band high reflectivity feature of HCGs makes them promising candidates for integrating with Vertical-Cavity Surface-Emitting Lasers (VCSELs). Utilizing HCGs instead of commonly used Distributed Bragg Reflectors (DBRs) can significantly increase tuning speed in a tunable VCSEL and implement polarization control [45], [46]. Moreover, HCGs can be used for the fabrication of high-Q factor cavities [47] monolithic filters [48], and hollow-

core waveguides [49], [50]. Besides, the application of HCGs in optical sensing has been shown in several studies [19], [23], [51]–[53].

In order to obtain a comprehensive understanding of HCGs, an analytical study of propagating waves along the grating structure will be conducted in the next section.

2.1.1 Analytical Solutions

Without loss of generality, to simplify the formulation, the incident light is considered normal-surface TM-polarized. Figure 2.2 shows a cross-sectional view of a substrate-free HCG, which is periodic in the x-direction and infinite in the y-direction. The input and output planes are located at z=0 and z=D, respectively. The width of grooves and bars are shown by **a** and **s**, respectively, while the Λ is the grating period. As we can see, the HCG divides space into three regions; reflection, grating, and transmission. I refer to these three regions as r, g, and t and show them by subscripts in the equations.

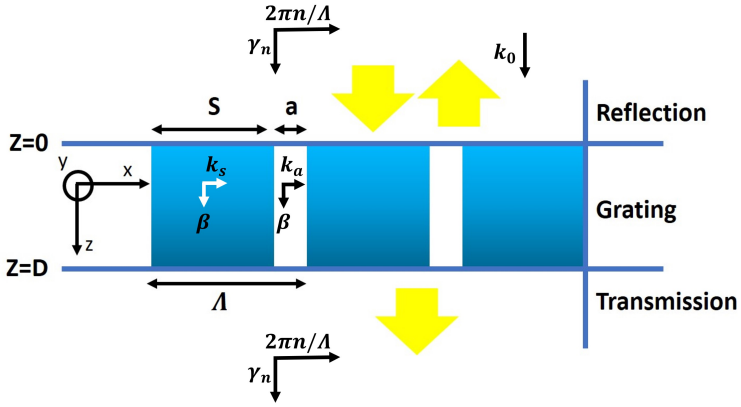

Fig. 2.2: Schematic cross-sectional view of an HCG, showing three divided regions. z=0, and z=D are input and output planes, respectively. **a**, **s**, and Λ are grooves' width, bars' width, and the grating period, respectively.

In the first step, I calculate the magnetic and electric fields in the reflection and transmission regions, where waves propagate in the air. Because there is no periodic structure in these two regions, the lateral magnetic and electric field profiles in the reflection and transmission regions are equal. Then I calculate magnetic and electric fields in the grating layer, and by satisfying period boundary condition and dispersion relation, the modes are derived.

In the reflection region, the magnetic and electric fields consist of the incident plane wave ($e^{-ik_0 z}$) and the summation of multiple reflected modes where n is the reflected mode number starting from n=0. The magnetic (2.1) and electric (2.2) fields in the reflection region are calculated [43].

$$H_y^r(x,z) = e^{-ik_0 z} - \sum_{n=0}^{\infty} r_n \mathcal{H}_{y,n}^r(x) e^{i\gamma_n z} \tag{2.1}$$

$$\mathcal{H}_{y,n}^r(x) = \cos[(2n\pi/\Lambda)(x - a/2)]$$

In these equations, $\mathcal{H}_{y,n}^r(x)$, and $\mathcal{E}_{x,n}^r(x)$ are lateral magnetic and electric field profile, respectively. In the reflection region, the periodicity of the grating structure introduces phase shifts and interference effects. As a result, the electric and magnetic fields exhibit periodic behavior in the reflection region. In the transmission region, where there is no physical periodic structure, the periodicity in the electric and magnetic fields arises due to energy conservation and waves' interference. r_n is the reflection coefficient; γ_n is the propagation coefficient, where n is the order of the reflected modes. Here, μ_0 and ε_0 are the vacuum permeability and permittivity, respectively. The air-gap center ($x = a/2$) is selected as the symmetry plane for the reflected modes.

$$E_x^r(x,z) = e^{-ik_0 z}\sqrt{\mu_0/\varepsilon_0} + \sum_{n=0}^{\infty} r_n \mathcal{E}_{x,n}^r(x) e^{i\gamma_n z} \tag{2.2}$$
$$\mathcal{E}_{x,n}^r(x) = (\gamma_n/k_0)\sqrt{\mu_0/\varepsilon_0} H_{y,n}^r(x)$$

$$k_0 = 2\pi/\lambda, \qquad {\gamma_n}^2 = {k_0}^2 - (2n\pi/\Lambda)^2 \tag{2.3}$$

Similarly, the magnetic and electric fields in the transmission region are given by (2.4) and (2.5), where D is the grating thickness, and τ is the transmission coefficient. It should be noted that because there is no periodic structure in transmission and reflection regions and both regions have the same refractive index, the lateral magnetic and electric field profile in reflection and transmission regions are equal (2.6).

$$H_y^t(x,z) = \sum_{n=0}^{\infty} \tau_n \mathcal{H}_{y,n}^t(x) e^{-i\gamma_n(z-D)} \tag{2.4}$$

$$E_x^t(x,z) = \sum_{n=0}^{\infty} \tau_n \mathcal{E}_{x,n}^t(x) e^{-i\gamma_n(z-D)} \tag{2.5}$$

$$\mathcal{H}_{y,n}^r(x) = \mathcal{H}_{y,n}^t(x), \qquad \mathcal{E}_{x,n}^r(x) = \mathcal{E}_{x,n}^t(x) \tag{2.6}$$

Then, the electric and magnetic fields in the grating region (2.7) and (2.8), which bridges reflection and transmission regions, are calculated. There are m waveguide-array modes in this region, with lateral magnetic and electric fields of $\mathcal{H}_{y,m}^g(x)$ and $\mathcal{E}_{x,m}^g(x)$, respectively. The propagating constant in the longitudinal direction is β_m, where the amplitude of the forward (+z) and backward (-z) propagating modes are shown by a_m and b_m, respectively.

$$H_y^g(x,z) = \sum_{m=0}^{\infty} \mathcal{H}_{y,m}^g(x)[a_m e^{-i\beta_m(z-D)} - b_m e^{+i\beta_m(z-D)}] \tag{2.7}$$

$$E_x^g(x,z) = \sum_{m=0}^{\infty} \mathcal{E}_{x,m}^g(x)[a_m e^{-i\beta_m(z-D)} + b_m e^{+i\beta_m(z-D)}] \tag{2.8}$$

Lateral magnetic and electric fields ($\mathcal{H}_{y,m}^g(x)$ and $\mathcal{E}_{x,m}^g(x)$) in grooves and bars, exhibiting different distributions are shown in (2.9) and (2.10), respectively.

In grooves

$$\mathcal{H}_{y,m}^g(x) = A\cos[k_{a,m}(x-a/2)] + B\sin[k_{a,m}(x-a/2)] \tag{2.9}$$
$$\mathcal{E}_{x,m}^g(x) = (\beta_m/k_0)\sqrt{\mu_0/\varepsilon_0}\mathcal{H}_{y,m}^g(x)$$

In bars

$$\mathcal{H}_{y,m}^g(x) = C\cos[k_{s,m}(x-\{(a+\Lambda)/2\})] + D\sin[k_{s,m}(x-\{(a+\Lambda)/2\})] \tag{2.10}$$
$$\mathcal{E}_{x,m}^g(x) = n_{bar}^{-2}(\beta_m/k_0)\sqrt{\mu_0/\varepsilon_0}\mathcal{H}_{y,m}^g(x)$$

Here, k_a and k_s are the lateral wavenumbers inside grooves and bars, respectively. In the case of surface-normal incidence, $\mathcal{H}_{y,m}^g(x)$ and $\mathcal{E}_{x,m}^g(x)$ are even functions because there is no preferred direction among +x and -x, and therefore the modes have a standing wave (cosine) lateral profile [39]. Thus, B and D constants are zero in this case. Satisfying the periodic boundary conditions (2.11) in the x-direction determines the value of A and C constants (2.12).

$$\mathcal{H}^g_{y,m}(x) = \mathcal{H}^g_{y,m}(x + l\Lambda), \quad l = 1, 2, 3, ... \tag{2.11}$$

$$\mathcal{E}^g_{x,m}(x) = \mathcal{E}^g_{x,m}(x + l\Lambda)$$

$$A = \cos(k_{s,m}S/2), \qquad C = \cos(k_{a,m}a/2) \tag{2.12}$$

On the other hand, the definition of longitudinal modes (β_m) leads to deriving a relation between lateral modes in grooves and bars (2.13).

$$\beta_m^2 = (2\pi n_{air}/\lambda)^2 - k_{a,m}^2 = (2\pi n_{bar}/\lambda)^2 - k_{s,m}^2 \tag{2.13}$$
$$k_{s,m}^2 - k_{a,m}^2 = (2\pi n_{air}/\lambda)^2(n_{bar}^2 - 1)$$

The equation between the lateral wavenumbers k_a and k_s can be solved by matching the boundary conditions at $x = 0$ and $x = a$ to describe the waveguide array:

$$n_{bar}^{-2}k_{s,m}tan(k_{s,m}S/2) = -n_{air}^{-2}k_{a,m}tan(k_{a,m}a/2) \tag{2.14}$$

The dispersion relations resulting from (2.13) and (2.14) are shown in figure 2.3. Figure 2.3, displays the dispersion relation in a TE/TM-polarized, surface-normal incidence HCG, exciting four even waveguide array modes. While in the case of normal incidence, only even modes are excited, for oblique angle incidence cases, odd modes should be considered. Gray dash lines show the air and dielectric light lines. Moreover, *a*, *b*, and *c* show cutoff frequencies. The cutoff frequencies determine the operating regime in gratings. Thus, the

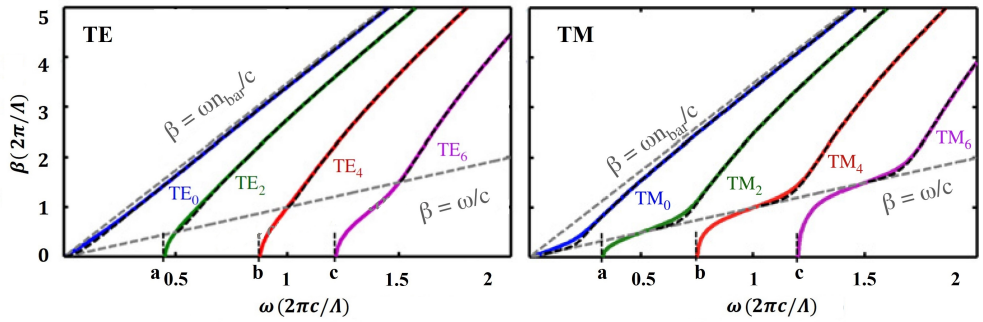

Fig. 2.3: Dispersion curves of TE/TM-polarized, surface-normal incidence HCG, exciting four even modes. The air and dielectric light lines are displayed by gray dash lines. a, b, and c indicates cutoff frequencies [43].

Near-WL regime is positioned between the two first cutoff frequencies ($\omega = a$ and $\omega = b$), where only two modes exist (TE_0 and TE_2), called the dual-mode regime. As we can see, HCGs share some similarities with other typical waveguides, such as emerging more modes in higher frequencies. However, in contrast to the continuum modes spectra in slab waveguides for $\beta < \omega/c$, HCGs show a discrete range. Generally, the TE and TM dispersion curves are the same. However, the slope of the TM curve changes significantly near the air light line, while for TE light, the slope is nearly constant. This difference can lead to the different properties of TE and TM-polarized HCGs.

The waveguide array structure exhibits multiple orthogonal propagating modes in the grating region, which do not interact with each other as they propagate. However, when these modes encounter the boundaries in the z direction (at z = 0 and z = D) the array waveguide modes can couple with plane waves in reflection and transmission regions, as well as with each other due to the sudden change in boundaries. Once the waveguide array modes in the grating region move forward and hit the output plane at z=D, they may be reflected back and simultaneously coupled to each other. The same phenomenon can happen when modes move backward and approach the input plane. Vectors $\mathcal{F}$, and $\mathcal{B}$ describe

the coefficients of the forward and backward modes, respectively.

$$\mathcal{F} \equiv (\mathcal{F}_0 \;\; \mathcal{F}_1 \;\; \mathcal{F}_2 \;\; ...) \tag{2.15}$$

$$\mathcal{B} \equiv (\mathcal{B}_0 \;\; \mathcal{B}_1 \;\; \mathcal{B}_2 \;\; ...)$$

The reflection matrix (ρ) relates forward and backward modes (2.16).

$$\mathcal{B} = \rho\mathcal{F} \tag{2.16}$$

The non-diagonality of matrix ρ indicates that the HCG modes in the grating region couple together at the reflection plane. Furthermore, the propagation matrix Φ describes the accumulated phase when each mode propagates from z=0 to z=D (2.17). In contrast with the reflection matrix, the propagation matrix is diagonal, resulting in non-coupled orthogonal modes. It means that the modes do not couple with each other in the grating layer.

$$\Phi_{n,m} = \begin{cases} e^{-i\beta_m D}, & \text{if } n = m \\ 0, & \text{otherwise} \end{cases} \tag{2.17}$$

Now matrix ρ and consequently reflectivity and transmissivity by matching the boundary conditions of H_y and E_x at the input (z=0) and output (z=D) planes can be calculated. The first boundary condition is considered as having continuous H_y and E_x at the output plane (2.18).

$$\begin{aligned} \sum_{n=0}^{\infty} \tau_n \mathcal{H}^t_{y,n}(x) &= \sum_{m=0}^{\infty} \mathcal{H}^g_{y,m}(x)(\mathcal{F}_m - \mathcal{B}_m) \\ \sum_{n=0}^{\infty} \tau_n \mathcal{E}^t_{x,n}(x) &= \sum_{m=0}^{\infty} \mathcal{E}^g_{x,m}(x)(\mathcal{F}_m + \mathcal{B}_m) \end{aligned} \tag{2.18}$$

By applying the Fourier integral on both sides of (2.18), the transmission coefficients (τ_n) can be expressed in terms of the overlaps between lateral magnetic field profiles [43]. The transmitted coefficients in a matrix format can be rephrased as below.

$$\boldsymbol{\tau} = \mathbf{H}(\boldsymbol{F} - \boldsymbol{B}) = \mathbf{E}(\boldsymbol{F} + \boldsymbol{B}) \tag{2.19}$$

By substituting (2.16) in (2.19), the transmission coefficient would be

$$\boldsymbol{\tau} = \mathbf{H}(\mathbf{I} - \boldsymbol{\rho})\boldsymbol{F} = \mathbf{E}(\mathbf{I} + \boldsymbol{\rho})\boldsymbol{F} \tag{2.20}$$

where the reflection matrix ρ is

$$\boldsymbol{\rho} = \frac{(\mathbf{I} - \mathbf{H}^{-1}\mathbf{E})}{(\mathbf{I} + \mathbf{H}^{-1}\mathbf{E})} \tag{2.21}$$

Similarly, by matching the boundary conditions at the input plane the reflection coefficient is derived as

$$\mathbf{r} = \frac{(\boldsymbol{\chi} - \mathbf{I})}{(\boldsymbol{\chi} + \mathbf{I})} \tag{2.22}$$

where

$$\boldsymbol{\chi} = \frac{\mathbf{E}(\mathbf{I} + \boldsymbol{\Phi}\boldsymbol{\rho}\boldsymbol{\Phi})}{\mathbf{H}(\mathbf{I} - \boldsymbol{\Phi}\boldsymbol{\rho}\boldsymbol{\Phi})}$$

Finally, the HCG reflectivity and transmissivity are

$$\mathbf{R} = \mid \mathbf{r} \mid^2 \qquad \mathbf{T} = \mid \boldsymbol{\tau} \mid^2$$

where in a lossless material

$$\mathbf{T} + \mathbf{R} = 1$$

In this section, I analytically studied waveguide array modes in the grating

region and investigated the wave behavior at input and output boundaries. Moreover, I defined reflection and propagation matrices, which have a significant impact on HCG behavior. In the end, by matching the field profile at the exiting planes, transmissivity and reflectivity were calculated. In the next section, I will discuss the unique phase selection rule in Near-WL HCGs and its results in extraordinary phenomena such as broad-band reflectivity and high-quality factor resonance.

2.1.2 Phase Selection Rules

As I mentioned in the previous section, HCGs' non-trivial properties come from their unique manner of selecting the phase. Thus, to fully understand this particular phase selection, I need to investigate the wave propagation inside the grating and study its behavior at input and output planes. The grating structure divides the space into three regions; reflection region, grating region, and transmission region (figure 2.2). The waveguide array structure in the x-direction stimulates propagating modes in the grating region. These propagated modes do not interact with each other due to their orthogonality. However, at the input (z=0) and output (z=D) boundaries, these modes may be confined in the grating region and form a cavity in the z-direction.

At the plane's boundaries, propagating modes can couple to the reflection and transmission plane, as well as they can couple into adjacent modes. This does not disagree with the orthogonality of the modes in the grating region, which is related to the diagonality of the matrix Φ because the reflection involves interaction with the external modes coming from the transmission region, which are not orthogonal to the modes in the grating layer [54]. Interference of these modes at input and output boundaries may result in fascinating phenomena, such as broad-band

reflectivity. Coupling modes together and to the boundary's planes can affect the magnitude and phase of each waveguide array mode. Herein, to understand the phase evolution of the propagating modes, the reflectivity contour map of a normal TE incident light according to normalized wavelengths and grating thickness was displayed in figure 2.4.a).

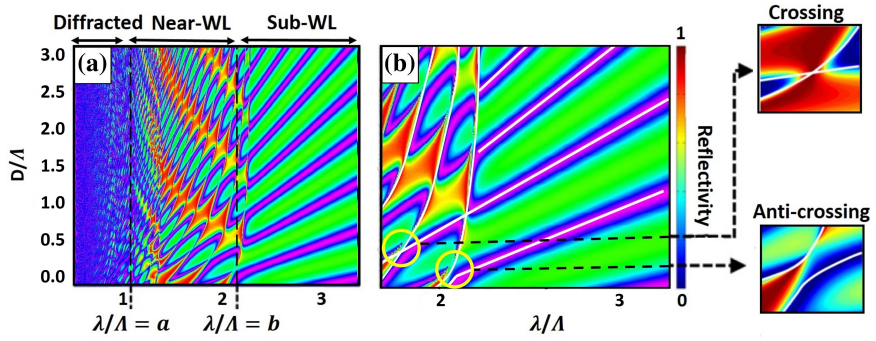

Fig. 2.4: **a)** Reflectivity contour map of a TE-polarized, surface-normal incident light to an HCG. The checkerboard pattern is created via changing grating thickness over wavelengths, indicating three operation regimes. **b)** Analytical solutions of FP resonance conditions (2.23) plotted on the contour map (solid white lines). A zoomed-in view of crossing and anti-crossing points are shown as well.

The given reflection pattern clearly shows three grating regimes, including, Diffraction, Sub-WL, and Near-WL regions. For wavelengths shorter than λ/Λ=a, the grating operates at the diffraction region, where numerous modes emerge and form a disordered pattern. However, between λ/Λ=a, and λ/Λ=b, a highly ordered checkerboard pattern is formed by two excited modes in this region, named the dual-mode regime. In this region, half of the checkerboards show high reflectivity (dark red parts), whereas the other half indicates a lower reflectivity. Indeed, the interference of the two modes at the output plane is responsible for this interesting pattern. By increasing λ/Λ, the system moves into a new regime, where only one mode exits (Sub-WL regime).

In this study, I am interested in the dual-mode region and its consequent

extraordinary phenomena. As I mentioned, due to the boundary condition, the HCG can act as a cavity. The behavior of this cavity is controlled by the propagation (Φ) and the reflection (ρ) matrix. In the dual-mode regime, the size of Φ and ρ are reduced to a 2×2 matrix. The order of given eigenvalues from $\rho\Phi$ matrix after one round-trip in the grating is defined by m. The related phase to the m_{th} mode is displayed by ψ_m. Similar to a simple Fabry-Perot (FP) cavity, HCG supports a self-sustainable mode, satisfying the round-trip condition inside the cavity. This round-trip condition is shown by (2.23), where n is positive integer numbers [43].

$$\psi_m = n\pi \tag{2.23}$$

The analytical solutions of (2.23) are displayed over the checkerboard reflection pattern, shown by solid white curves in figure 2.4.b). I can observe two families of curves; one linear and the other parabolic. The linear curves are related to the zero-order mode ψ_0=$n\pi$, and parabolic curves correspond to the second-order, ψ_2=$n\pi$. The analytical solutions of the FP condition are well-matched with the reflectivity contour. This excellent agreement testifies that the physical mechanism, which makes the HCG spatial, resides in (2.23).

$$\mid \Delta\psi \mid = \mid \psi_2 - \psi_0 \mid = l\pi \qquad l = 0, 1, 2, ... \tag{2.24}$$

As you can see in figure 2.4.b), linear and parabolic curves intersect at specific wavelengths and grating thickness. This intersection can be interpreted as reaching the FP condition for both modes at the same time. When the phase-difference of intersected modes is an odd factor of π ($l = 1, 3, 5, ...$), the modes cross each other, named crossing points. However, when phase difference is an even factor of π ($l = 0, 2, 4, ...$), two curves repel each other and make

anti-crossing points. Equation (2.24) indicates this phenomenon clearly. In the next section, I will discuss the role of crossing and anti-crossing points in creating extraordinary phenomena in HCGs, such as broad-band reflectivity and high-quality-factor resonating.

2.1.2.1 100% Reflectivity and Transmissivity

In the previous part, I discussed the two-mode nature of the Near-WL regime. I found out this dual-mode regime is strongly affected by grating thickness. Therefore, by optimizing grating thickness, I can manipulate the amplitude and phase of these two modes to cancel each other at the output plane (z=D), resulting in zero transmissivity and 100% reflectivity. To achieve this goal, two modes are supposed to have the same amplitude and opposite phase (phase-difference $=\pi$) at the output plane. Figure 2.5 evidently displays this process.

In figure 2.5, pink and red curves show the amplitude of the zero-order and second-order mode, respectively, while the blue curve indicates the phase-difference between these two modes at different wavelengths, located at the output plane. The intersection of red and pink curves indicates the same amplitude for both modes. If this intersection matches with π phase-difference between these two modes, they cancel each other at the output plane, resulting in 0% transmissivity and, consequently, 100% reflectivity. The black dashed lines in figure 2.5 display the points that two modes have the same amplitude and π phase difference. It is notable that through a proper design, 100% reflection points can couple together and cover a broad range of wavelengths, resulting in a broad-band high-reflection mirror.

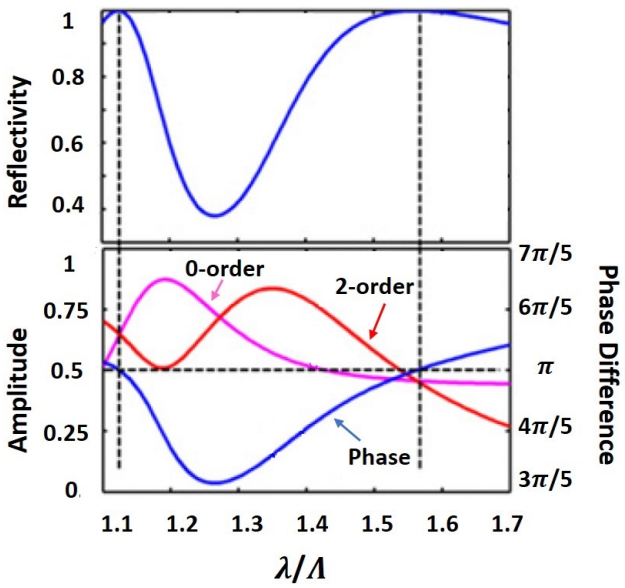

Fig. 2.5: Two-mode cancellation at the output plane of the HCG resulting 0% transmissivity and 100% reflectivity (dash black lines). Pink and red curves show the amplitude of the zero-order and second-order modes, respectively. The blue curve indicates the phase difference between these two modes at different wavelengths [43].

Similarly, by taking advantage of the interference concept, the 100% transmissivity can be explained. In the case of 100% transmissivity, grating modes at the output plane should have the same amplitude as the modes at the input plane. Hence when the granting modes outcouple to the transmission region, they indicate the same amplitude as incident modes from the input plane, resulting in 100% transmissivity [43]. We should note that input and output modes, in addition to having the same amplitude, should be in-phase. Besides the 100% reflectivity and transmissivity, the dual-mode regime indicates high-quality-factor points. The mechanism of creating these high-Q-factor resonances in HCGs will be studied in the following.

2.1.2.2 High Quality-Factor Resonance

I have already discussed crossing and anti-crossing points, where crossing points show the intersection of two modes with opposite phases, and anti-crossing indicates the intersected in-phase modes. Therefore, I expect that due to having the same phase and amplitude, anti-crossing points show a more significant intensity profile overlap, leading to a strong coupling between them. This strong coupling results in the high-quality-factor resonance. Figure 2.6 shows the intensity profile of a crossing and anti-crossing point, respectively, at the grating region. While the anti-crossing point offers a giant field intensity in order of 10^7, the crossing point shows only 25 [43].

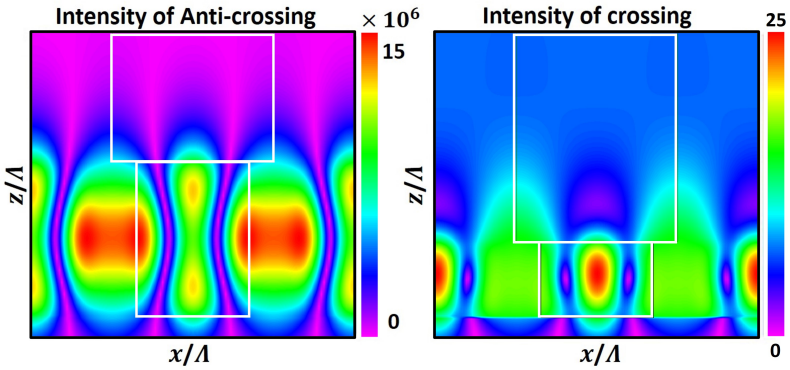

Fig. 2.6: Intensity profile inside the grating at the crossing and anti-crossing points. The anti-crossing point indicates 10^6 intensity enhancement, compared to the crossing point.

The resonance mechanism in HCGs is totally different from trivial FP cavities. In FP cavities, modes are entirely orthogonal and do not couple together at input and output planes. On the contrary, HCG modes can strongly be coupled at exiting planes, resulting in sudden changes in the refractive index's spatial distribution. Despite the non-orthogonality nature of HCG modes, someone can define $\rho\Phi$ matrix on a new basis, where the given eigenstates would be orthogonal. This new set of modes are named supermodes.

When a self-sustainable supermode satisfies the round-trip condition, or in other words, satisfies (2.24), the high-Q factor mode is generated. Figure 2.7 shows how the sudden change in reflectivity is related to the high-Q-factor resonance and how well this point is matched with the HCG resonance condition (2.25).

$$\det[I - (\rho\Phi)^2] = 0 \tag{2.25}$$

HCG cavities offer two advantages compared to trivial FP resonators. First, HCGs are ultra-thin, in order of half-wavelengths. Second, they can indicate high-Q-factor with no need for extra high-reflectivity mirrors.

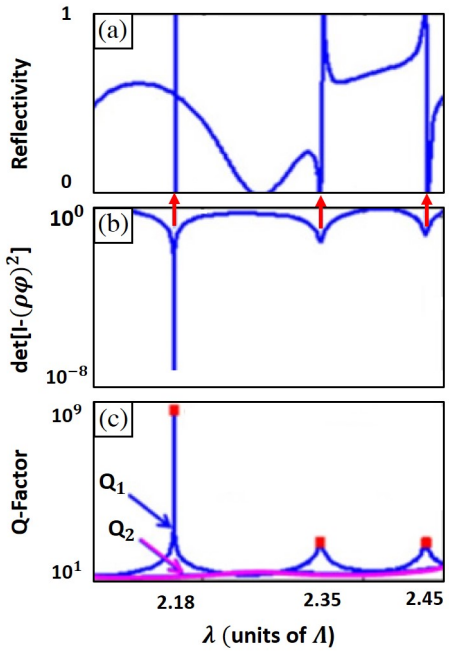

Fig. 2.7: **a)** Reflection spectrum, exhibiting three dramatic changes at 2.18, 2.35, and 2.45 (Λ). **b)** Satisfied HCG resonance condition. The mode positioned at 2.18 (Λ) indicates the closest value to zero. **c)** Q-factor value of two different supermodes. The blue curve is related to the shown reflection spectrum, while the reflection spectrum of the pink curves has not been plotted. In comparison, the Q_1 is dominant [43].

As we can see in figure 2.7.b), (2.25) has predicted three resonances. Among these resonate modes, the one that drops closest to zero indicates the highest Q-factor (figure 2.7.c)). In an HCG under a continuous excitation, several supermodes may be excited. However, The supermode with the highest Q-factor will build up energy faster and be dominant. The Q-factor of each supermode can be calculated by (2.26), where Q_j is the Q factor of j_{th} supermode, D is the grating thickness, n_{gr} is the effective refractive index, and r_j is the j_{th} eigenvalue of the $\rho\Phi$ matrix [43].

$$Q_j = 2\pi D(n_{gr}/\lambda) \mid r_j/(1 - {r_j}^2) \mid \tag{2.26}$$

Hence the maximum value of the Q-factor would be the overall Q-factor of the HCG. Blue and pink curves in figure 2.7.c) show two supermodes owning two different Q-factor, where the Q_1 has been dominated. In this section, first, we got familiar with HCGs and their extraordinary properties. Then, I thoroughly discussed the physical mechanisms behind non-trivial phenomena, such as broad-band reflectivity and high-Q-factor resonance. As I mentioned, integrating the concept of Parity-Time (PT) Symmetry with HCG offers the potential for a unique single mode and nearly-zero bandwidth photonic resonant emission, which can facilitate the integration of light sources into a monolithic substrate. Thus, in the next section, I will review the Party-time (PT)-symmetry concept and its following exciting phenomena.

2.2 Parity-time (PT)-Symmetric Systems

In quantum physics, each system is described by a matrix, called Hamiltonian. Hamiltonians can predict the behavior of the system. Thus, the Hamiltonian eigenvalues determine the energy of the system, and eigenvectors describe the

states. Conveniently, Hamiltonians can be Hermitian or non-Hermitian. For a long time, it was believed that only Hermitian systems, which are in equilibrium with the environment, possess real eigenvalues [55]. However, in 1998 Bender and Boettcher [56] questioned this claim and indicated that non-Hermitian systems, which are not in equilibrium, can have real spectra as well.

They showed that if a Hamiltonian remains invariant under spatial reflection ($p \rightarrow -p$, $x \rightarrow -x$) and time-reversal ($p \rightarrow -p$, $x \rightarrow x$, $i \rightarrow -i$) still can have real eigenvalues. While it is still doubted that PT-Symmetry is a basic property of nature, it shows the same feature with naturally transpired symmetries [57]. PT-symmetric systems indicate spontaneous symmetry breaking, followed by a phase transition from real to complex eigenvalues. Moreover, this transition can go in a backward direction restoring the broken symmetry [58].

Despite the potential implications of the PT-symmetric concept, the full realization of PT-symmetric systems in quantum physics is still unsettled. Challenges such as many-body interactions, decoherence effects, and generally, the difficulty in achieving non-Hermiticity in a PT-symmetric form are burdens to obtain a fully quantum-based PT-symmetric system [59]. However, recently, it has been realized that optics and photonics can accommodate a fertile ground to practically fulfill the PT-symmetric concept. The analogy between the Schrödinger equation and Maxwell's theory, especially in the paraxial approximation, provides a powerful platform to test the PT-Symmetry concept in practice [60].

The first theoretical study on optical PT-symmetric structures came back to 2007 [61], where two identical coupled waveguides were selected as the PT-symmetric platform. The suggested platform is shown in figure 2.8.a), where the green part represents gain and yellow stands for loss. Moreover, figure 2.8.b)

shows the complex Refractive Index (RI) profile, in which the blue and red curves stand for the real and imaginary parts, respectively. Three years later, in 2010 [60], the anticipated theoretical results were observed in practice. Besides two coupled waveguides, the other two components systems, such as coupled microrings [62]–[64] and coupled silica microtoroid [65]–[67], have shown PT-symmetric properties. Moreover, introducing more than two coupled components could scale up the system leading to new functionalities [68]–[70].

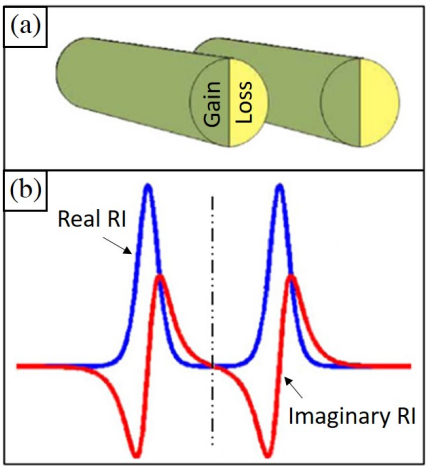

Fig. 2.8: **a)** Schematic view of a PT-coupled waveguide (green and yellow parts represent gain and loss respectively). **b)** Complex refractive index profile (blue and red curves, stand respectively for real and imaginary parts) [61].

The efforts in the design and comprehension of optical PT-symmetric systems have resulted in extraordinary phenomena, which had not been observed in trivial Hermitian systems. Single-mode lasing [63], [71], [72], asymmetric diffraction [73]–[75], reflectionless unidirectionality [76]–[78], and enhanced RI-sensitivity [79], [80] are the most well-known non-trivial effects observed in PT-symmetric systems. In the following, I will explain the required conditions for PT-Symmetry and PT-Symmetry breaking in detail. Furthermore, optical PT-symmetric systems accompanied by their non-trivial properties will be elaborated.

2.2.1 PT-Symmetry and PT-Symmetry Breaking

In order to obtain a better understanding of the PT-Symmetry condition, a simple two-component system, containing two complex frequencies is considered. The related Hamiltonian is described as [57]:

$$H = \begin{bmatrix} \omega_1 - \gamma_1 & k \\ k & \omega_2 - \gamma_2 \end{bmatrix}$$

ω_1 and ω_2 are real part of frequencies and γ_1 and γ_2 correspond loss or gain. Moreover, k shows the coupling strength between these two components. The eigenvalues of this system are calculated in (2.27).

$$\omega_{\pm} = \frac{\omega_1 + \omega_2}{2} - i\frac{\gamma_1 + \gamma_2}{2} \pm \sqrt{k^2 + (\frac{\omega_1 - \omega_2}{2} + i\frac{\gamma_1 - \gamma_2}{2})^2} \tag{2.27}$$

To simplify the discussion, I rephrased the eigenvalues by new parameters,

$$\omega_{\pm} = \omega_0 - i\eta \pm \sqrt{k^2 + \delta^2} \tag{2.28}$$

where

$$\omega_0 = \frac{\omega_1 + \omega_2}{2},\ \ \eta = \frac{\gamma_1 + \gamma_2}{2},\ \ \delta = \alpha + i\beta,\ \ \alpha = \frac{\omega_1 - \omega_2}{2},\ \ \beta = \frac{\gamma_1 - \gamma_2}{2}$$

In (2.28), if $\sqrt{k^2 + \delta^2} = 0$, the two eigenvalues will coalesce at a specific point called an Exceptional Point (EP). In contrast to Hermitian systems, in which only the eigenvalues coalesce, but the eigenvectors can be orthogonal to each other (Diabolic point), at the EP, both eigenvalues and eigenvectors coincide, such that the Hamiltonian is not diagonalizable anymore. This feature can lead to unique functionality for non-Hermitian PT-symmetric systems.

I have mentioned that the uniqueness of PT-symmetric systems is indicating real eigenvalues despite its non-Hermitian Hamiltonian. Hence to satisfy this property, in (2.28) two conditions should be hold i) $\eta = 0$ and ii) $k^2 + \delta^2 \geq 0$. In other word $\frac{\gamma_1+\gamma_2}{2} = 0$, leading $\gamma_1 = -\gamma_2$. The second condition introduce an imaginary part $2i\beta\alpha$, which should be zero, due to the first condition β cannot be zero, therefore $\alpha = 0$, leading $\omega_1 = \omega_2$. Consequently to fully satisfy the second condition $k^2 \geq \beta^2$. By forcing these conditions ($\gamma_1 = -\gamma_2 = \gamma$ and $\omega_1 = \omega_2 = \omega$) the Hamiltonian can be rewrite as:

$$H = \begin{bmatrix} \omega - \gamma & k \\ k & \omega + \gamma \end{bmatrix}$$

and eigenvalues are rephrased as:

$$\omega_{\pm} = \omega \pm \sqrt{k^2 - \gamma^2} \tag{2.29}$$

Therefore in this notation, the only condition to have real eigenvalues is that the coupling strength should be larger than loss and gain ($k \geq \gamma$). The PT-symmetric phase is broken, and its spectra become complex when $k < \gamma$. Moreover, the EP occurs when the coupling strength is precisely equal to the loss/gain ($k = \gamma$). In this section, we got familiar with the PT-symmetric Hamiltonian and the necessary conditions to have real spectra in a non-Hermitian system. In the next part, I elaborate on the analogy between the Schrödinger equation and the paraxial equation. Indeed the similarity between these two equations has inspired the concept of optical PT-symmetric systems.

2.2.2 PT-Symmetry In Photonics

This section investigates the resemblance between the Schrödinger equation and the paraxial equation to obtain a more comprehensive understanding of optical PT-symmetric system operation. The paraxial equation of diffraction (2.30) describes the spatial dispersion of a light beam, in which only a small amount of it spreads transversely, and the light travels roughly parallel to the propagation direction [61], [81],

$$i\frac{dE(x,z)}{dz} + \frac{1}{2k}\frac{d^2E(x,z)}{dx^2} + k_0[n_r(x) + in_i(x)]E(x,z) = 0 \tag{2.30}$$

where $E(x,z)$ is the electric field, $n_r(x)$ is the real refractive index and $n_i(x)$ is the imaginary part of the refractive index, $k = k_0 n_0$ is the wavevector, $k_0 = 2\pi/\lambda$ (λ is the wavelength and n_0 is the substrate index). The Schrödinger equation (2.31) illustrates the temporal evolution of a particle in a defined potential [82].

$$i\hbar\frac{d\psi(x,t)}{dt} + \frac{\hbar^2}{2m}\frac{d^2\psi(x,t)}{dx^2} - V(x)\psi(x,t) = 0 \tag{2.31}$$

Here, $\psi(x,t)$ is the amplitude of the probability, $\hbar$ is Planck's constant, m is the mass, and $V(x)$ is the potential. By comparison (2.30) and (2.31), someone can find out the similarity ($z = t$, $E(x,z) = \psi(x,t)$, $k = m/\hbar$, $n(x) = -V(x)/k_0\hbar$). In the paraxial equation, the electric field behaves like the probability function, and the refractive index and z parameter play the role of potential and time, respectively [57]. After finding the similarity between these two equations, I first investigate the Schrödinger equation under the PT operator, and then isomorphically, I conclude that the same condition can be applied to the paraxial equation to be PT-symmetric.

$$\xrightarrow{PT} i\hbar\frac{d\psi^*(-x,-t)}{dt} + \frac{\hbar^2}{2m}\frac{d^2\psi^*(-x,-t)}{dx^2} - V^*(-x)\psi(x,t) = 0 \tag{2.32}$$

In quantum physics theory $\psi^*(-x,-t) = \psi(x,t)$ [82]. Thus, to have an invariant equation under the PT operator, the potential should satisfy the condition of $V(x) = V^*(-x)$. If I rewrite the potential in a complex form ($V(x) = V_r(x) + iV_i(x)$), to satisfy this condition, the real part of the potential should be an even function of x, and the imaginary part should be an odd function of x. Similarly, in the optical format, in which the refractive index plays the potential role, the real part of the refractive index should be a symmetric function of x, while the imaginary part (loss/gain) is an asymmetric function of x. The most straightforward way to achieve this optical potential is using a coupled two identical component system (waveguides or resonators), one having loss and the other having gain. It should be noted that although the analogy of Schrödinger and the paraxial equation is evident, the PT-symmetric concept is not only limited to the paraxial wave equation, and it can appear in different optical formats as well [74], [83], [84].

In this section, I derived the analogy between the paraxial wave equation and the Schrödinger equation, which led to obtaining meaningful information about the system potential. I found out that to satisfy the PT-Symmetry in an optical format, the refractive index's real and imaginary parts should be an even and odd function of x, respectively. In the following, I will study the optical PT-symmetric systems with various applications in different areas.

2.2.2.1 Single-mode PT-Symmetric Lasing

Almost four years after establishing the optical PT-Symmetry theory, in 2012, Miri et al. [72], for the first time, suggested a simple PT-symmetric platform to design a single-mode-operation laser. In this letter, they used two coupled identical multimode waveguides, one exhibiting gain, and the other showing an equal amount of loss. Via coupled-mode theory, they investigated the amplitude evolution of the m_{th} mode in these two waveguides. Equations (2.33) and (2.34) show the coupled-mode equations, where a_m and b_m are modal amplitudes of waveguides one and two, β_m is the propagation constant, k_m is the coupling strength and $\pm\gamma_m$ is the modal gain or loss of the m_{th} mode.

$$\frac{da_m}{dz} = i\beta_m a_m + ik_m b_m + \gamma_m a_m \tag{2.33}$$

$$\frac{db_m}{dz} = i\beta_m b_m + ik_m a_m - \gamma_m b_m \tag{2.34}$$

The coupled-mode equations' solution leads to the formation of two supermodes, which in symmetry regime ($k_m \geq \gamma_m$), none of them experience gain and remain neutral. However, in the PT-Symmetry broken regime, where gain/loss exceeds the coupling coefficient, one of the two supermodes is amplified, while the other is suppressed exponentially with distance. By knowing the fact that the coupling is commonly stronger between higher-order modes [72], I can conclude that I need a greater amount of gain and loss for breaking the PT-Symmetry in higher orders. In other words, I can design the system in a way that only fundamental modes experience PT-Symmetry breaking, while the rest of the modes remain in the symmetry regime. Hence I can amplify fundamental modes with the optimized level of gain and loss, keeping other

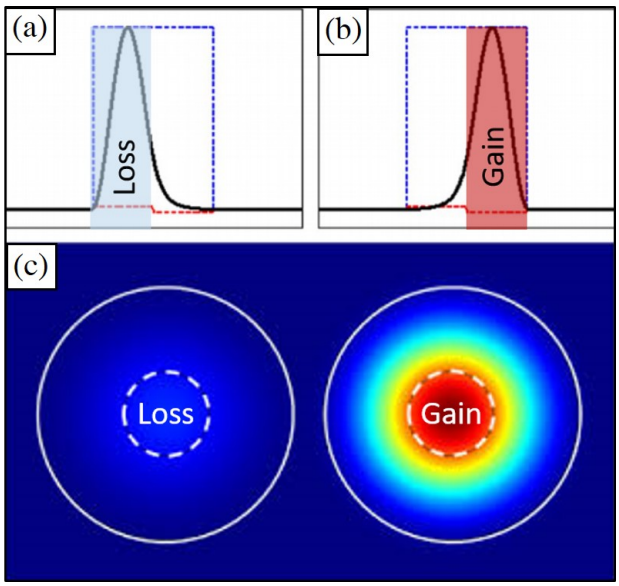

Fig. 2.9: Intensity profile of the **a)** suppressed mode and **b)** amplified mode in a 1D structure. Intensity profile of the **c)** amplified mode in a 2D structure [72].

modes neutral and bounded.

The finite element simulation of two coupled waveguides (30 μm thickness each), operating at 1 μm, showed that only the fundamental supermode (TE_0) experienced PT-breaking. Furthermore, Miri et al. [72] investigated 2D PT fibers, in which the high-order modes break easier than fundamental modes. However, with the design modulation, they could recover the breaking of the fundamental modes. Figure 2.9 shows the intensity profile of the first broken supermode in 1D and 2D structures. Figure 2.9.a) and 2.9.b) represent the suppressed and the amplified modes, respectively, in a 1D structure. Figure 2.9.c) illustrates the confined mode in the gain, leading to a significant amplification, in a 2D structure. Moreover, they indicated that the net effect of any imperfection and perturbation only appeared in shifting the optimized gain/loss, and still, the single-mode operation is possible.

In 2014 Feng et al. [85] reported the first experimental demonstration of the

PT-symmetric laser. In this work, they took advantage of the continuous rotational symmetry of Whispering-Gallery-Modes (WGMs) to reduce the laser threshold. They designed a microring resonator with 500 nm-thick InGaAsP Multiple Quantum Wells (MQWs) on an InP substrate. The gain and loss are periodically introduced by Germanium and Chrome, respectively, on the InGaAsP in an azimuthal direction (figure 2.10.a)).

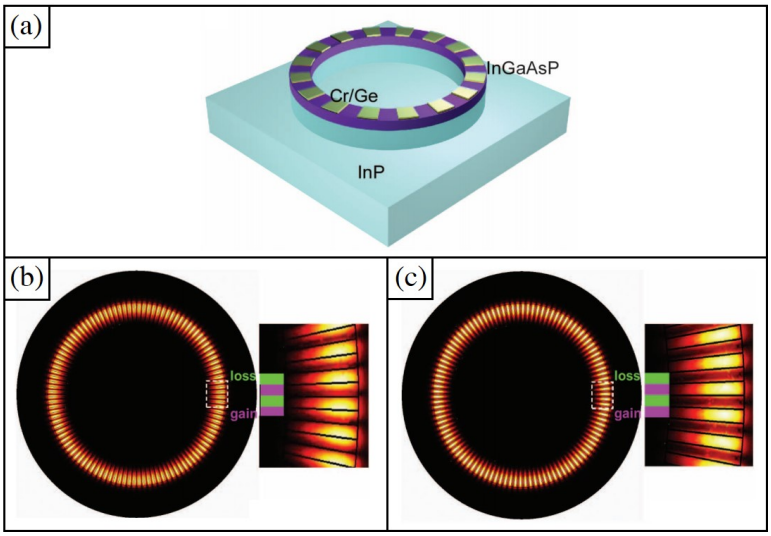

Fig. 2.10: **a)** Schematic illustration of the PT-symmetric laser. Distributions of the electric field intensity, where **b)** modes are evenly confined in the gain and loss (PT-Symmetry), and **c)** modes are mostly confined in the gain part (broken PT-Symmetry) [85].

In the suggested design, when the amount of introduced gain/loss exceeds the coupling coefficient, the system transits from the PT-Symmetry phase to the symmetry-broken phase. Figures 2.10.b) and 2.10.c) show the symmetry and symmetry-broken phase, respectively. While in the symmetry phase, the lasing mode overlaps with gain and loss regions equally, in the symmetry-broken phase, the mode overlaps mostly with the gain. Confining the lasing mode, mostly in the gain areas, suppresses all other WGMs by the loss, leading to the single-mode operation. In the same year, Hodaei et al. [62] showed the single-mode operation,

using two separated microrings (one ring as gain the other as loss), which led to an easier fabrication process, compared to Feng's work. Figure 2.11 indicates the single-mode operation of two coupled PT-symmetric microrings, compared to the multi-mode operation of a pumped single ring.

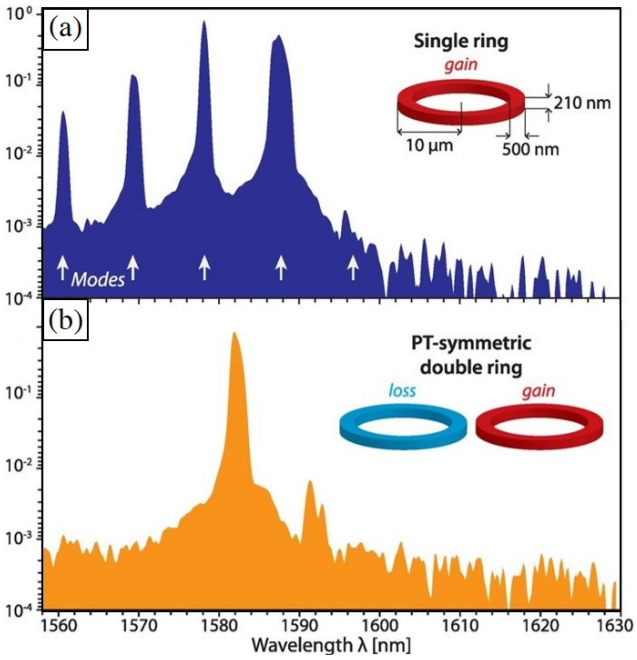

Fig. 2.11: **a)** Emission spectrum of a single microring, exhibiting the multi-mode operation. **b)** Emission spectrum of a PT-symmetric two coupled microrings, exhibiting the single-mode operation [62].

Regardless of the suggested platforms [64], [67], [71], [86], in all these optical structures, the key idea is that the symmetry-breaking threshold depends exclusively on the relation between gain/loss and the coupling coefficient. Thus, by an optimized structure, I can select which mode experiences PT-Symmetry breaking. The beauty of PT-symmetric lasers is that single-mode operation is possible even in an active broad-band medium with several competing modes. In the next part, we will be familiar with another unique property of PT-symmetric systems, named unidirectionality.

2.2.2.2 Asymmetric Diffraction and Directional Emission

In 2011 Lin et al. [87] found a new property induced by the periodic PT-symmetric structure, named unidirectionality. They designed a Bragg grating with distributed gain and loss in a periodic manner. In this structure, the incident light from the left does not see the grating and passes it through unaffected, showing no reflection. However, the light entering from the right-side experiences improved reflection from the exact same grating.

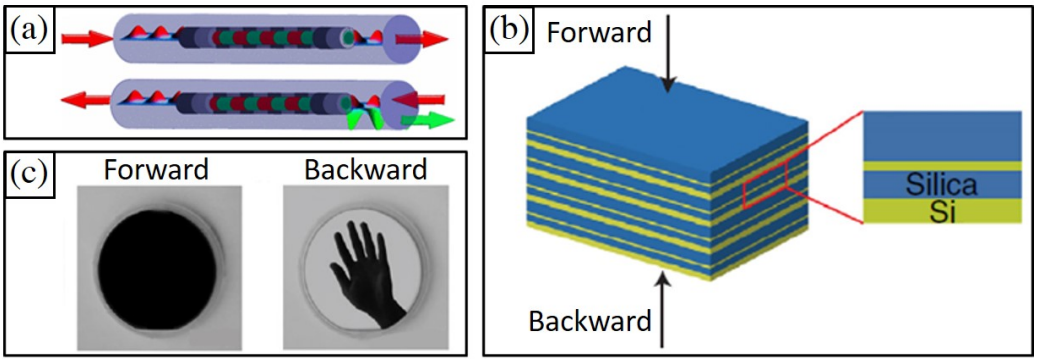

Fig. 2.12: Schematic view of **a)** an active PT-symmetric [87] Bragg reflector and **b)** a passive PT-symmetric Bragg grating [88]. **c)** In the passive grating, the incident light from forward shows no reflection from the hand above the structure. However, the entering wave from backward experiences enhanced reflection and shows the hand pattern [88].

Figure 2.12.a) displays this phenomenon schematically, where green and red arrows show the transmitted and reflected light. In this work, the given eigenvalues from the transfer matrix relate forward and backward wave's amplitude, resulting in two different reflection coefficients for the left and right sides (2.35) and (2.36).

$$R_L = \frac{(n_1 - n_2)^2 k^2 / 4{n_0}^2}{\delta^2 + \mid \lambda \cot(\lambda L) \mid^2} \tag{2.35}$$

$$R_R = \frac{(n_1 + n_2)^2 k^2 / 4{n_0}^2}{\delta^2 + \mid \lambda \cot(\lambda L) \mid^2} \tag{2.36}$$

In these equations, n_0 is the effective refractive index, n_1 and n_2 are the real and imaginary parts of the refractive index, respectively. k is the wavevector. λ is the operating wavelength. L is the grating length, and δ is the period-related factor.

According to (2.35) and (2.36), with no loss/gain modulation ($n_2 = 0$), the left and right-side reflections are the same, and no unidirectionality is observed. Furthermore, at $n_1 = n_2$, the system experiences the highest asymmetry level, where left-hand reflection becomes zero. In 2013 Feng et al. [76] reported an experimental demonstration of PT-symmetric unidirectionality. They used a passive structure, involving only lossy media. Despite non-balanced gain/loss modulation, the expected unidirectionality, derived by the theory, was observed. Indeed, applying the gauge transformation can relieve the hidden PT-Symmetry in exclusively lossy non-Hermitian Hamiltonians [57]. Figure 2.12.b) shows a schematic view of the passive grating, including silica and silicon. Figure 2.12.c) shows the vanished reflection from the hand above the structure when the light comes in the forward direction and the enhanced reflection in the backward direction.

In addition to Bragg gratings [89]–[91], asymmetric diffraction and unidirectionality have been observed in PT-symmetric periodic lattices [92], [93], microrings [77], [94], and PT-symmetric circuits [95]. In all these platforms, the introduced loss manipulates the light direction in a preferred way. This section explored the observed unidirectionality as a non-trivial character of PT-symmetric systems with potential applications in filters, sensors, and

integrated optoelectronic devices. In the next section, I will investigate the impact of PT-symmetric systems in enhancing the sensors' performance.

2.2.2.3 Enhanced Sensing at Exceptional Points

This section aims to indicate the enhanced sensitivity of non-Hermitian systems, especially the PT-symmetric structures, compared to Hermitian systems. The hidden symmetry in many physical systems can manifest itself in degenerate states. Introducing a perturbation breaks this symmetry and leads to the splitting of eigenvalues. This procedure can be used as a detection method to identify the introduced perturbation. Here, I aim to compare the eigenvalue splitting in Hermitian and non-Hermitian systems at singular points.

The first step to calculate the eigenvalue splitting is defining the unperturbed Hamiltonian of Hermitian ($H_{0,1}$) and non-Hermitian ($H_{0,2}$) systems at the diabolic point and exceptional point, respectively. Then a non-Hermitian perturbation (ϵH_1) will be introduced to the system, leading to the eigenvalue splitting. According to (2.37), the splitting in a Hermitian system evolves linearly with the perturbation strength (ϵ). However, in a non-Hermitian system, the splitting scales with the square root of the perturbation strength (2.38) [57].

$$H_{0,1} = \begin{bmatrix} \lambda_0 & 0 \\ 0 & \lambda_0 \end{bmatrix} \quad H_{0,2} = \begin{bmatrix} \lambda_0 & \beta_0 \\ 0 & \lambda_0 \end{bmatrix} \quad H_1 = \begin{bmatrix} \lambda_1 & \beta_1 \\ \beta_2 & \lambda_1 \end{bmatrix}$$

$$\Delta\lambda_{Her} = 2\epsilon\sqrt{\beta_1\beta_2} \tag{2.37}$$

$$\Delta\lambda_{non-Her} = 2\sqrt{\epsilon}\sqrt{\beta_0\beta_2 + \epsilon\beta_1\beta_2} \tag{2.38}$$

Therefore, due to a weak perturbation ($\epsilon \ll 1$, $\beta_0 \gg \beta_1$) a non-Hermitian

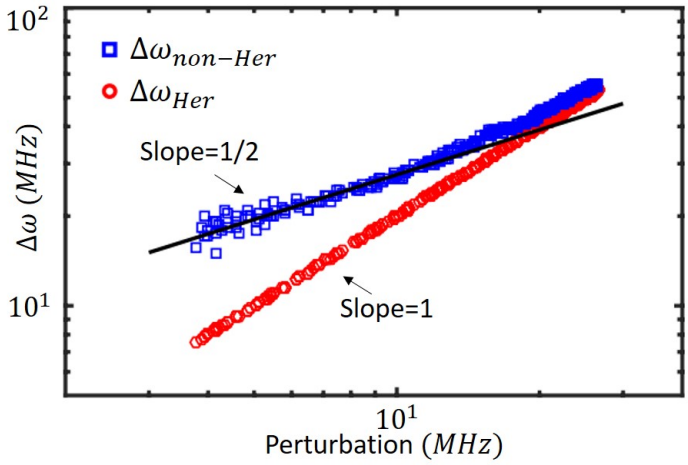

Fig. 2.13: Frequency splitting of a Hermitian (red line) and non-Hermitian (blue line) system according to the perturbation strength [96].

system indicates more splitting compared to a Hermitian system. Figure 2.13 compares the frequency splitting of a Hermitian (red line) and non-Hermitian (blue line) system in a weak perturbation regime. As we can see, the non-Hermitian system shows higher frequency splitting compared to the Hermitian system [96]. In practice, this situation can be associated with two degenerate whispering gallery modes, perturbated by a particle [96], [97]. Thus, this small perturbation, caused by the particle, can make a more significant change in a non-Hermitian system rather than a Hermitian system, which leads to identifying that particle easier.

It can be concluded that the eigenvalue splitting follows $\epsilon^{1/N}$-dependence, where N is the degeneracy order of the exceptional point [98]–[100]. Thus, higher orders of degeneracy lead to higher sensitivity for small perturbations. The order of EP degeneracy can scale up by introducing more than two coupled components. For instance, Hodaei et al. [100] experimentally indicated three-fold sensitivity enhancement in a system consisting of three coupled rings. Two rings showed gain and loss; the third one remained neutral.

EPs show higher eigenvalues splitting compared to diabolic points, and higher-order EPs indicate a higher amount of splitting. However, it is essential that the split eigenvalues would be resolvable. To resolve the split spectra, the total loss of a system should be smaller than splitting. Hence among different non-Hermitian systems, PT-symmetric systems, in which gain balances the introduced loss, can resolve narrower bandwidth. Nevertheless, a totally lossy PT-symmetric system cannot show the same resolvability due to its higher total loss.

In this section, we got familiar with PT-symmetric systems and their unique properties, including unidirectionality, single-mode lasing, and enhanced sensitivity at EPs. Moreover, I studied the mechanism behind PT-Symmetry and breaking PT-Symmetry. Furthermore, I realized that the analogy between traditional PT-symmetric systems, roots in quantum physics, and optical PT-symmetric systems in photonic led to the accomplishment of optical PT-symmetric systems. In the next Chapter, I will present an HCG structure to improve the performance of uncooled PbSe-based photodetectors in Mid-IR sensors.

Chapter 3

Mid-IR Photodetector Engineering Via Photonic Gratings

Mid-IR detectors enable us to broaden our vision to the realm of heat, which help us to perceive the world in a different way. Built upon this technology, the thermal imaging system has developed a broad range of applications, including night vision, failure analyses, infrared astronomy, and medical diagnostic [101], [102]. In comparison to thermal detectors responding to the temperature variations caused by heat, Mid-IR photodetectors, directly converting spectral-dependent infrared radiation into electric charges, are much preferable because of their intrinsic fast response advantages. However, majorly due to their thermally induced device noise and dark current limitations, the room-temperature operation of this type of detector has been a great challenge for decades. Thus, a cooling system is generally required, which makes the imaging system bulky and expensive [102]. As one kind of Mid-IR photodetectors, PbSe photoconductors have remained the choice for many civilian and military sensing applications in 3 to 5 μm spectral region [103], simply because their uncooled functionality and superior detectivity $>3\times10^9$ cmHz$^{1/2}$W^{-1} could satisfy many practical-use requirements [104].

In fact, this level of performance has not been fully optimized and could be potentially improved by almost two orders of magnitudes, considering the

theoretical Background-Limited Infrared Performance (BLIP) limit is at $\sim 10^{11}$ cmHz$^{1/2}$W^{-1} [105]. In recent years, a lot of research efforts have been focused on understanding the material physics and charge transportation behaviors in order to improve the internal quantum efficiency and suppress the noise and dark current impacts [106],[107]. On the other hand, due to a large refractive index contrast between the PbSe material and the ambiance, the overall detection efficiency is also significantly affected by reflection and transmission losses. Therefore, investigating possible methods to reduce the light coupling losses can also be an essential pathway to boost the detector performance significantly.

In 2014, Weng et al. [108], developed an effective strategy to significantly reduce light reflection loss. By using a biomimetic broadband anti-reflective nano-coating, the uncooled PbSe Mid-IR photoconductor exhibited a record-high peak detectivity of 4.2×10^{10} cmHz$^{1/2}$W^{-1} at room temperature. This anti-reflective coating was developed to modify the light and sensor interaction on the top surface of the device. Nevertheless, considering the optical transmission loss from the bottom of the active thin film, a thick layer of the PbSe film still needs to be prepared, which unfortunately induces further issues like the increased Johnson noise [109]. Such a problem offsets the counterpart advantage of enhancing the light-harvesting efficiency. Therefore, developing another solution to modify the light-matter interaction behavior at the bottom surface of the device so that both the absorption enhancement and the device Johnson-noise suppression can be satisfied is of great research interest to further elevate the sensor performance to a higher level.

Traditionally, to achieve this goal, depositing a layer of metal as a mirror reflector has been the most straightforward solution. However, unlike solar cells [110], from the practical viewpoint, using the metallic reflector does not work

in the PbSe detectors scheme since the thin film has to be sensitized at high temperature under active gas ambiance with O_2 and Iodine mixtures. Metal films degrade dramatically in this sensitization process and unavoidably lose their perfect reflective properties [107]. Additionally speaking, by having a layer of metallic film laying down the PbSe thin film, the inherent short-circuit problem can also hardly be addressed. Therefore, in this work, I theoretically propose a unique approach to fulfill the same purpose as aforementioned.

Thus, I propose a one-dimensional grating layer to be implemented and inserted under the PbSe photosensitive layer. Due to the resonance tuning mechanism, this grating layer could uniquely manipulate Mid-IR light-matter interactions. It not only prevents light transmission loss from the backside of the device but also tunes the destructive interference in the reflectance spectra, which consequently maximize the light absorption in the weak-absorbing energy band-tail region. By combining these two capabilities, it is possible to improve the detector's sensitivity significantly. With this goal, several grating parameters, including grating period, fill factor, and grating thickness, will be systematically investigated and optimized using the Rigorous Coupled Wave Analysis (RCWA) method.

To determine a photodetector's overall performance, specific detectivity (D*) is commonly used as the standard figure-of-merit [102].

$$D^* = \frac{\eta}{I_n}[\frac{\lambda q g (A_0 \Delta f)^{1/2}}{hc}] \tag{3.1}$$

where λ is the wavelength, η is quantum efficiency, q is the electron charge, g is the photoconductive gain, A_0 is the optical area, Δf is the band frequency, h is Planck's constant, c is the light velocity, and I_n is the electrical noise which is included Johnson and generation-recombination noises [102]. According to (3.1),

I need to generally consider two major fundamental factors, including quantum efficiency and electrical noise.

Quantum efficiency is the light-to-current conversion efficiency, which tells how many electrons can be collected resulting from an input photon. The expression for quantum efficiency takes the form of:

$$\eta = (1 - \zeta_1 + \zeta_2 e^{-\alpha t})(1 - e^{-\alpha t}) \tag{3.2}$$

Where ζ_1 is Fresnel reflection on the incident surface, ζ_2 is the back-surface reflection, t is the detector thickness in the direction of propagation, and α is the absorption coefficient [109]. One strategy to increase specific detectivity could be increasing the quantum efficiency by increasing the detector thickness. However, by increasing the thickness, the detector resistance will be decreased. So, the equivalent resistance of the load resistor and the detector resistor would be decreased. Consequently, Johnson-noise would be increased. You can see this process clearly in (3.3).

$$i_J = \sqrt{\frac{4KT\Delta f}{R_{eq}}} \tag{3.3}$$

in which i_J is Johnson noise, K is Boltzmann constant, T is temperature, Δf is the frequency band, and R_{eq} is the equivalent resistance [109]. Thus, inherent Johnson noise, unfortunately, offsets its counterpart of light harvesting advantage. On the other hand, the detectivity through (3.4) is dependent on detector thickness

$$D^* = \frac{\lambda}{hc}(1 - e^{-\alpha t})[2(G + R)t^{-\frac{1}{2}}] \tag{3.4}$$

where λ is the wavelength, h is Planck's constant, c is the light velocity, G and R are the generation and recombination rates, t is the detector thickness, and α is the absorption coefficient [102]. Thus, the highest detectivity will be obtained when

$t = 1.26/\alpha$ where $(1 - e^{-\alpha t})t^{-1/2}$ achieves the maximum value. This thickness is a trade-off between high quantum efficiency and low thermal generation. So, for a PbSe layer, the highest detectivity will be obtained when t=1.26 μm in which the average absorption coefficient in the range of 3-4.4 μm is $10^4\ cm^{-1}$. By considering all these discussions, there is a strict limitation on detector thickness. According to (3.2), the other strategy to enhance quantum efficiency is minimizing Fresnel reflection, which has been conducted in previous works and it had had a notable impact on absorption enhancement. Also, it is expected that maximizing back-surface reflection to increase the absorption length could improve the absorption value notably. To achieve this goal, a broadband reflector could be used.

As discussed, using a metallic reflection mirror is not viable for the PbSe detectors. Alternatively, I found that a one-dimensional dielectric grating structure could offer similar broadband reflection functionality as the metallic mirrors but rely on a different physics mechanism, based on coupling resonances in a lateral direction. Such lateral grating structures have demonstrated effective broadband light manipulating capability in various fields, including optical filters, displays, biosensors, and wideband reflectors [111], [112]. The phenomenon occurs when the incident wave is coupled with a lateral resonant mode supported by a grating structure under phase-matching conditions [113]. Conditions will be satisfied by optimizing grating parameters, including lattice period, fill factor, and grating thickness. Due to the resonance effect, the diffracted energy redistributes and manifests as transmission and reflection peaks [114]. Also, electric fields of modes confined to the surface could be intensively enhanced in comparison to the electric field of the excitation source [115], [116]. The mode spectral placement, their spectral density, and levels of interaction are the major factors affecting device operations and functionalities [117].

3.1 Results and Discussion

Herein, I use the Rigorous Coupled-Wave Analysis (RCWA) method to study and design the grating structures for enhancing PbSe Mid-IR photodetector performance. It is a known method to solve Maxwell's equations for electromagnetic diffraction in grating structures [118]. This method analyzes the diffracted waves from a planar grating bounded by two different media. The general approach in the RCWA method is to find solutions that satisfy Maxwell's equations in each of the three (input, grating, output) regions and then match the tangential electric and magnetic fields. In planar diffraction, the incident wave could have TE or TM polarization which is solved independently. Figure 3.1 demonstrates a schematic view of diffracted waves from a grating structure.

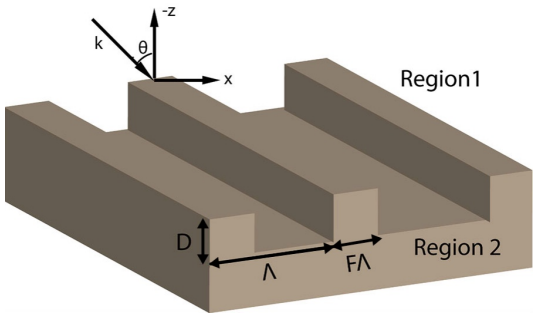

Fig. 3.1: Schematic view of diffracted waves from a grating structure.

Herein, I choose to work with TM-polarized modes because they have a greater Q-factor than TE modes, resulting in stronger absorption [115].

In this study, the grating layer is embedded underneath the PbSe (n_P=4.95) photo-sensitive layer in the device. The schematic view is presented in figure 3.2. As shown, the grating structure consists of periodically distributed dielectric materials of Silicon (n_H=3.489) and SiO_2 (n_L=1.45), which is the same material used for the substrate. The design parameters include the grating layer thickness d_1, PbSe thickness d_2, fill factor F, and lattice period Λ. Meanwhile, the incident wave, reflectance, and transmittance are denoted as **I**, **R**, and **T** respectively.

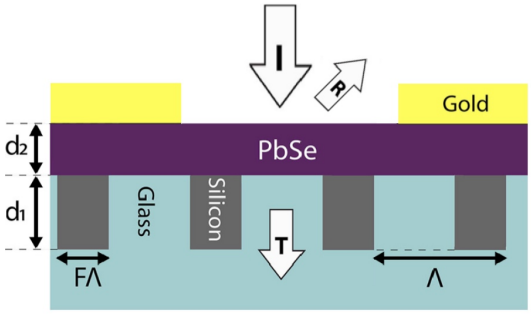

Fig. 3.2: Schematic view of a PbSe photoconductive detector with the integration of the grating structure under normal incidence.

By investigating the impacts of these parameters, as mentioned, a broadband and strong Mid-IR reflection of the grating layer is intended to be achieved. In this way, the backside transmission loss of the PbSe thin film would be strongly suppressed, and the light absorption could be enhanced consequently. The optimization of the lattice period and fill factor has been conducted by investigating transmission patterns. As shown in figure 3.3, a broadband suppression of transmission has been realized when the fill factor and period are in the range of 0.5-0.6 and 2.3-2.5 μm, respectively. It is also necessary to mention that our design in this study focuses on the wavelength range from 3 to 4.4 μm, considering the fact that the uncooled PbSe photodetector can only detect the photons up to $\sim$ 4.4 μm due to the energy bandgap limitation. Therefore, its wavelength-dependent absorption coefficient values have been

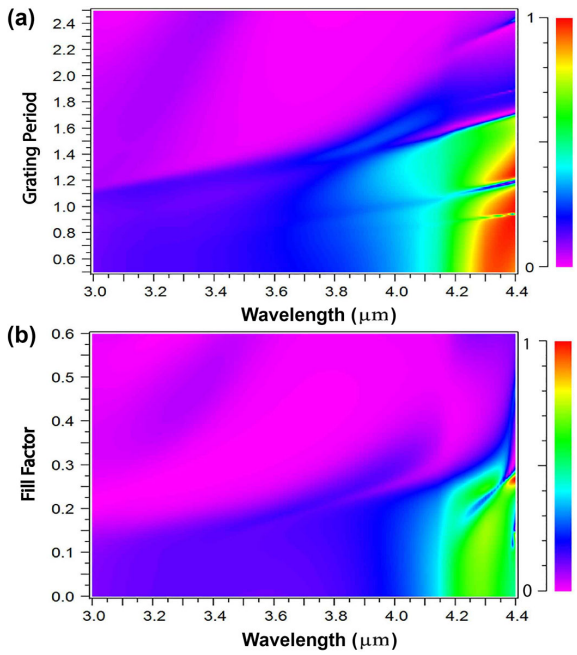

Fig. 3.3: **a)** Changing pattern of transmission according to manipulating lattice period, **b)** Changing pattern of transmission according to manipulating fill factor.

included in our simulation model as well.

As shown in figure 3.4.a), a strong transmission attenuation effect is achieved by applying a grating structure having a period of 2.4 μm, a fill factor of 0.49, and a thickness of 1.22 μm. It is also noted that the top PbSe layer in this design is of the optimized thickness value at 1.26 μm. Clearly, figure 3.4.a) demonstrates a strong suppression of the transmission spectrum in a broad wavelength range from 3 to 4.4 μm. It is notable that close to the bandgap region; the intensity reduces significantly from 65% down to $\sim$15%. The broadband reflection is achieved as shown in figure 3.4.b), which clearly makes this grating structure behaves like a mirror in the Mid-IR region. This broadband reflection is caused by the coupling of two modes in this wavelength range, which is presented as the transmission spectrum dips in figure 3.4.b).

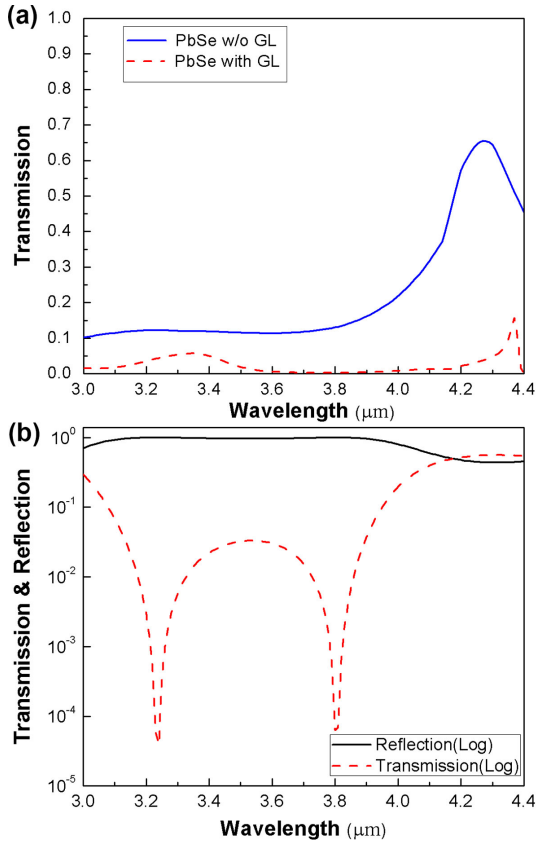

Fig. 3.4: **(a)** Transmission comparison of the Mid-IR photodetector device with and without the optimized grating structure under the PbSe thin film, **(b)** Reflection and transmission spectra of the grating reflector in logarithm scale. (Note: the simulated light is of TM polarization)

Figure 3.5 shows the enhanced absorption due to the grating structure. As can be seen, there are two peaks at 4.1 μm and 3.4 μm. These peaks are the product of the suppression of transmitted waves by coupled modes and the destructive interference of reflected waves at the same time. The calculation of the area under the curve (3-4.4 μm) demonstrates that total absorption enhanced from 0.49 to 0.65. This means that for a thin layer of PbSe (1.26 μm), implanting the grating structure enhances the absorption value by nearly 33%.

Moreover, I also discovered another unique advantage of using this grating layer to enhance the light absorption for the PbSe Mid-IR device, which is the ability

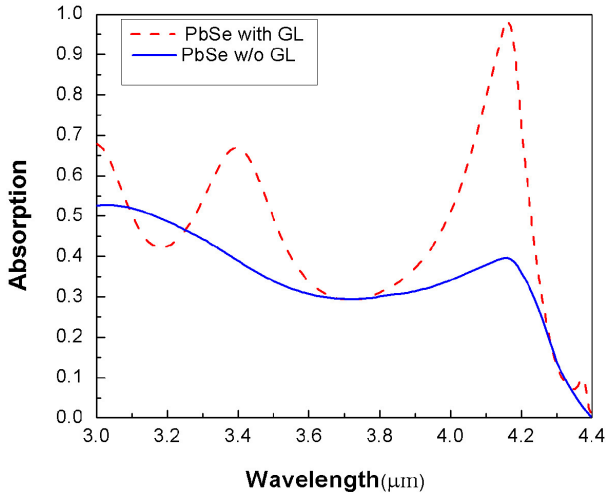

Fig. 3.5: Comparison between absorption value with and without the grating structure as the reflector (PbSe thickness=1.26 μm).

to control the interference peak positions. Besides benefiting the transmission loss suppression from the coupling effect, I could also minimize the reflection loss by controlling the vertical interference effect.

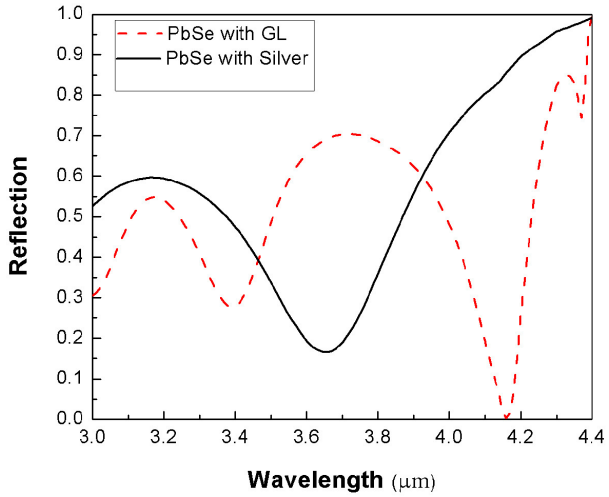

Fig. 3.6: Comparison between reflection value when I use the grating structure and silver as the reflector (PbSe thickness=1.26 μm), normal incidence.

When I use a layer of silver as a metallic mirror, it prevents light penetration and reflects the transmitted light completely. The only destructive wave is made at 3.66 μm (figure 3.6) according to (3.5),

$$2nd = (m - \frac{1}{2})\lambda \tag{3.5}$$

where n, d, m, and λ are the refractive index of PbSe, the thickness of PbSe, diffracted index (integer), and the wavelength, respectively [119]. Thus, the only way to change the position of destructive interference is by changing the thickness of PbSe. However, as described in the methodology section, the PbSe thickness should be set at a fixed value to achieve the best D* performance. Compared with the metallic mirror, this grating layer can be treated as an imaginary uniform layer with a constant effective refractive index, which allows a fraction of transmitted waves to go into the layer. Therefore, combined with the PbSe layer on top, the multilayer wave interference effect can be achieved. With this advantage, I could solely adjust the thickness of the grating layer and then be able to tune the reflection dips position to the energy band tail region where the weak absorption typically locates. Figure 3.6 shows the comparison between the reflected wave from the surface of PbSe when I use a layer of silver and the grating structure as the reflector.

Without changing the PbSe thickness and just by manipulating the grating parameters, I could make two destructive interferences in this range of wavelength. With that, implanting a grating structure at the bottom of the PbSe not only strongly attenuates transmitted waves but also suppresses the reflected waves through destructive interference as well. To provide a demonstration, as shown in figure 3.7, using the grating structure of Λ=2.4 μm, F=0.49, d_1=1.48 μm and d_2=1.26 μm, I would be able to modulate the absorption performance at the

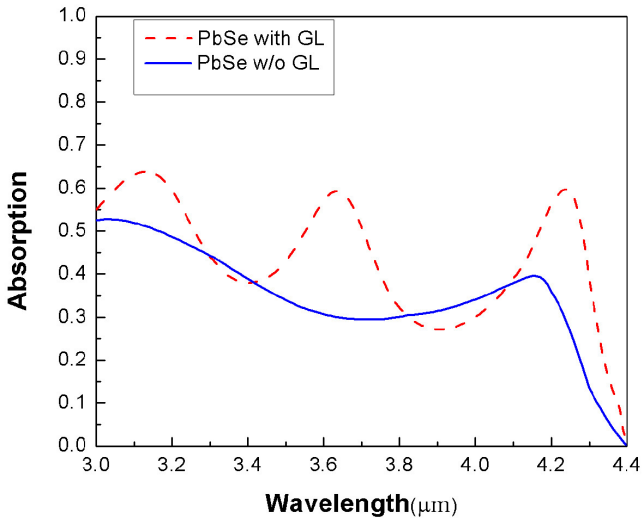

Fig. 3.7: Comparison between absorption value with and without the grating structure (Λ=2.4, F=0.49, d_1=1.48 μm, d_2=1.26 μm), TM polarization under normal incidence.

energy band tail region and the total absorption can be enhanced significantly between 4.2 to 4.4 μm, and the overall enhancement is by $\sim$ 24%.

In conclusion, I presented a new theoretical approach to enhance PbSe-based uncooled photodetectors in the Mid-IR wavelength region. To avoid increasing the device noise by using a thick PbSe film, I proposed a unique solution by using a broadband grating reflector to enhance the device's performance. Such structures behave like a metallic mirror and could prevent the light transmission loss from the backside of the device significantly, from 65% to less than 15%. Consequently, the total absorption was enhanced by nearly 33% by designing the grating layer. Moreover, simply tuning the grating thickness also enables us to adjust the interference pattern and minimize the reflection loss in the interested area. For example, this strategy could help us compensate for the decreased absorption near the band-gap range. By this method, the device could deliver decent performance at its cut-off band-edge area without cooling the material to move the band-edge into the higher wavelength region. This offers advantages

including low cost, low power consumption, and small footprint. They are critical for civilian and military applications, like gas sensing and thermal imaging.

This dissertation aims to address the need for smaller and more cost-effective mid-infrared (Mid-IR) sensors by focusing on the design and optimization of three different High Contrast Grating (HCG) structures. These structures are intended to improve various components of Mid-IR sensors, including the light source, the interaction path, and the detector. Chapter 3 of the dissertation is dedicated to the design of a broadband HCG structure with the goal of enhancing the performance of an uncooled photodetector based on Lead Selenide (PbSe) in the Mid-IR wavelength range. The main objective of this chapter is to improve the photodetector's efficiency and sensitivity. In the next chapter, the focus shifts to enhancing the interaction between light and gases in the Mid-IR range using a micro-size gas cell. The optical behavior of both single-layer and coupled-layer HCG structures will be investigated in the presence of CO_2 gas. This research demonstrates the promising potential of employing HCG structures to enhance light-gas interaction, particularly for on-chip gas sensing devices. Moreover, the integration of HCG structures with other photonic components, such as fibers, opens up possibilities for the development of advanced sensing systems.

Chapter 4

Photonic Gratings Enhancing Light-Absorption in a Miniaturized Gas Sampling Cell

Gas sensing has a variety of vital applications in environmental monitoring [120], disease diagnosis [121], manufacturing control [122], and national security surveillance [1]. Among different sensing methods, mostly thanks to the advanced nano-fabrication technology, chip-scale photonic-based sensors have received increasing attention. They offer multiple advantages, including faster response, higher sensitivity, compact size, low power consumption, and relatively low cost [123]. These properties make them a competitive candidate to be used for many new emerging technologies, such as the Internet of Things (IoTs).

Generally, photonic-based sensing technologies can be categorized into two groups: 1) refractive index-based [124], [125] and 2) absorption-based [126], [127]. In refractive index-based sensors, by introducing a gas or a liquid to a photonic structure, the refractive index changes, and thus the spectrum resonant peak of reflected or transmitted light shifts. Through measuring the shifted value, the gas can be detected [128]. This sensor is sensitive to small changes in the refraction index of the surrounding medium. However, since gas species and the concentration factors can both affect refractive index values, distinguishing between different gases can be challenging [129].

Fortunately, this issue can be addressed by the absorption-based method. Due to the intrinsic molecular vibration modes, the selectivity can be improved. As light passes through an analyte, the reflection or transmission is attenuated at specific wavelengths due to molecule absorptions, which are unique for each gas species. Increasing the gas concentration leads to an increased attenuated value [130]. Nevertheless, to achieve proper sensitivity in the absorption-based approach, I need to increase the light-matter interaction. Traditionally, this goal was attained by increasing the interaction path, which led to the fabrication of large and costly devices. Fortunately, in recent years, the significant progress in the nano-fabrication technology has inspired a significant number of scholars to introduce new photonic structures [131], [132], [133], [134], [135] to increase the light-matter interaction without extending the interaction path.

Among different micro-size structures, the simplicity and effectiveness of gratings have drawn significant attention toward HCGs for sensing applications. Gratings have been widely used in refractive index-based sensors [136], [137], [134], [138], [139]. However, very few works have been reported on using this structure in absorption-based sensors [140]. Normally, light tends to be confined to high-index areas. This tendency can make the grating optimization challenging for absorption-based gas sensors.

In this work, I aim to combine HCGs and an absorption-based method to investigate the light-matter interaction in the Mid-IR range. Here, our test sample is CO_2 because of its significant impacts on environmental, medical [141], and industrial [142] areas. The calculated absorption coefficient for 1% of CO_2, around 4.3 μm (the signature line absorption of CO_2 in the Mid-IR range) was reported to be 0.3 (cm^{-1} Pa^{-1}) [143]. It should be mentioned that by adjusting the grating parameters of the CHCG photonic structure, the technology can be applied to

detecting other gases as well.

Herein, by using the RCWA method, the functionality of the Single High Contrast Grating (SHCG) and CHCG in enhancing light absorption of CO_2 will be studied. Effective parameters in the grating design are grating thickness, air gap thickness, fill factor, and the period which are optimized accurately in this study. Lastly, it is noted that our numerical design is based on TE polarized modes simply because the light wave of TE modes has a much larger spatial coupling volume with gas molecules which could lead to an enhanced gas sensing performance. Specifically, when an electromagnetic (EM) field reaches a dielectric boundary, TM modes tend to stay in high index areas because its nodal plane presents at the boundary, which expels the EM's displacement field back to the high index areas [144]. However, such a nodal plane for TE modes does not exist at the boundary, which allows the energy penetration into the lower dielectric area having gas molecules [145], [146], [147].

4.1 SHCG Enabled Light-Absorption in Gas Sampling Cell

The schematic view of the SHCG consisting of a grating layer of silicon (n_{si}=3.5) and a layer of SiO_2 (n_{sio_2}=1.4) as a substrate is illustrated in figure 4.1.a) and 4.1.b). The design parameters are indicated, including the grating layer thickness D_1, fill factor F, and grating period Λ. Through optimizing the grating parameters, I aim to restrict intense light over the grating layer of the SHCG.

In this way, I am able to increase the chance of interaction of light and gas which leads to enhanced light absorption phenomena. Besides, it is expected that by increasing electric field intensity, the value of enhancement increases as well. Moreover, as much as I could trap the light in low-index areas over the grating

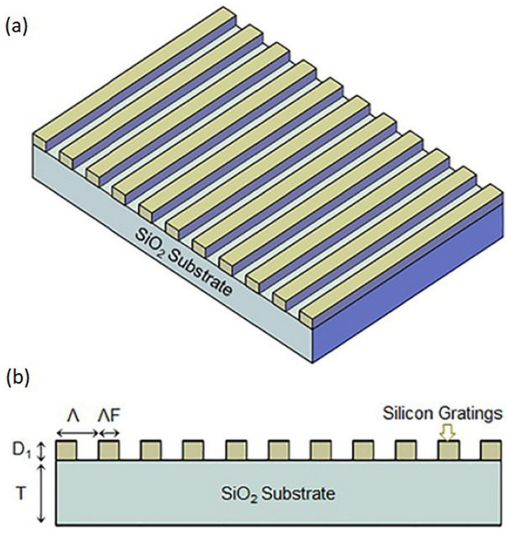

Fig. 4.1: **a)** 3D schematic view of the SHCG, made of silicon with SiO_2 substrate (relative to the grating thickness, the substrate thickness is infinite). **b)** Cross-sectional view of the SHCG. The grating layer thickness D_1, the fill factor F, and the grating period Λ are demonstrated in the figure.

layer, I will have more effective light-matter interaction. However, due to the tendency of light to be confined in the high index area, the optimization process by using SHCG can be challenging.

One of the most effective parameters in the grating optimization is the grating period. According to the grating period, the optical gratings can be categorized into three regimes: 1. diffraction regime (the period is greater than the wavelength) [36], 2. deep-subwavelength regime (the period is much less than the wavelength) [148] 3. near-wavelength regime (the period is almost equal to the wavelength). In the third regime, gratings behave entirely differently and show unusual features such as a broadband high-reflectivity [149] and the high-quality-factor resonance [150] in which the latter one can lead to enhance the light-matter interaction. Hence, I selected the initial value of the period equal to 4.3 μm.

The other notable design parameter is the grating thickness. According to

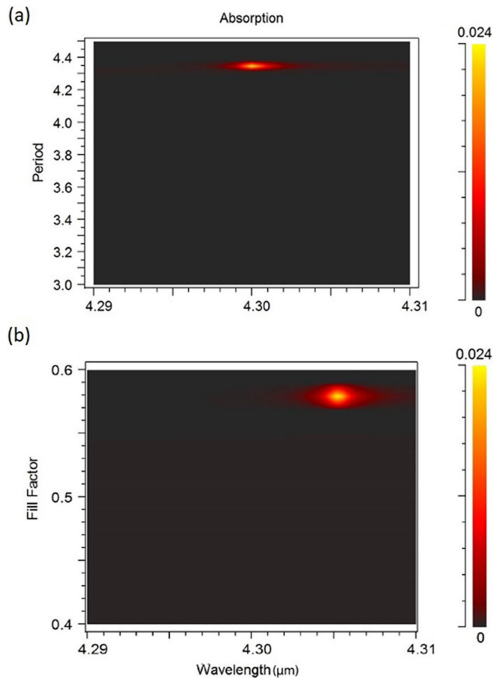

Fig. 4.2: **a)** Changing pattern of the light-absorption given by manipulating the period. The optimized period ≈ 4.3 μm. **b)** Changing pattern of the light absorption given by manipulating the fill factor. The optimized fill factor ≈ 0.57.

the incident light wavelength and the grating size, several waveguide modes are excited. These modes propagate through the grating and accumulate different phases. Due to the extreme mismatch between these modes and the exit plane, modes not only reflect but are also coupled with each other. The grating thickness defines the phase accumulated by the modes and controls their interference [43]. Hence, to achieve a high-quality-factor resonator, I need to choose the grating thickness so that constructive interference is obtained at the exit and input planes.

In order to achieve strong light absorption at the wavelength matching with the CO_2 vibration mode, the grating parameters of the HCG structure need to be modified and optimized. The rule of thumb for the design is to establish constructive light waves in the void low refractive index areas where gas molecules exist [151]. In this way, the strong resonating light energy will be able to spatially

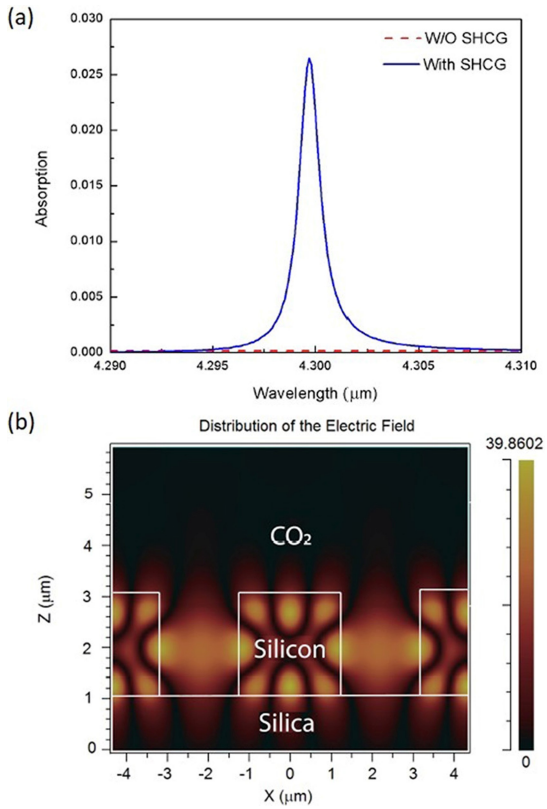

Fig. 4.3: **a)** Absorption spectra of CO_2 with and without SHCG from 4.29 μm to 4.31 μm. (Λ=4.336 μm, F=0.5775, and D_1=1.832 μm). The bandwidth of absorption peak=1.2 nm. **b)** Intensity and distribution of the confined electric field at 4.3 μm on the SHCG. The colored bar shows the intensity of the electric field. unit $(V/\mu m)^2$.

couple with gas molecules effectively. Figure 4.2.a) and 4.2.b) show the optimized value of the grating period $\approx$ 4.3 μm and fill factor $\approx$ 0.57 around 4.3 μm, where the absorption has its highest value. The color in these figures indicates the light absorption strength. From dark black to bright yellowish color, the intensity of the absorption increases. Clearly, it is shown that strong light absorption can be achieved with an optimized grating period and fill factor. On the contrary, without any optimization, the absorption effect can barely be obtained in the grating structure. The same process is done to optimize the grating thickness. It is necessary to mention that, all optimization parameters are correlated with each

other; changing one parameter changes the other. Thus, this correlation makes the optimization process challenging and time-consuming.

The given absorption spectra of CO_2, via the grating optimization (Λ=4.336 μm, F=0.5775, and D_1=1.832 μm) is shown in figure 4.3.a). While the absorption value of CO_2 without the HCG is approximately 10^{-4}, the implementation of the optimized SHCG enhanced this value to $\approx 2\times10^{-2}$. This improvement ($\approx$ 200 times) is emanated from confining the intense electric field to the grating layer. The intensity and distribution of the electric field at 4.3 μm are demonstrated in figure 4.3.b) It is evident if I can confine a more intense electric field over the grating layer, I will have more efficient light-matter interactions. Thus, in the following section, I propose a new coupled HCG (CHCG) design in order to add another vertical optical confinement for concentrating more light energy in the device.

4.2 CHCG Enhanced Light-Absorption in Gas Sampling Cell

Designing a new HCG layer with the same period and fill factor but different thickness, and coupling this new layer with the previous one to make a gap between them, gives us two more parameters to optimize: air gap thickness (D_2) and the thickness of new HCG (D_3). Figure 4.4.a) and .b) show a 3D and a cross-sectional view of CHCG, respectively. In the simulation, a similar optimizing strategy was used for these two new grating parameters.

Compared to figure 4.3.b), this design, through confining a more intense electric field ($\approx$ 2.5 times stronger), as shown in figure 4.5.b), gave us roughly 600 times enhancement. As demonstrated in figure 4.5.a), the maximized absorption value of CO_2 increased from 0.025 in SHCG to 0.2 in the CHCG.

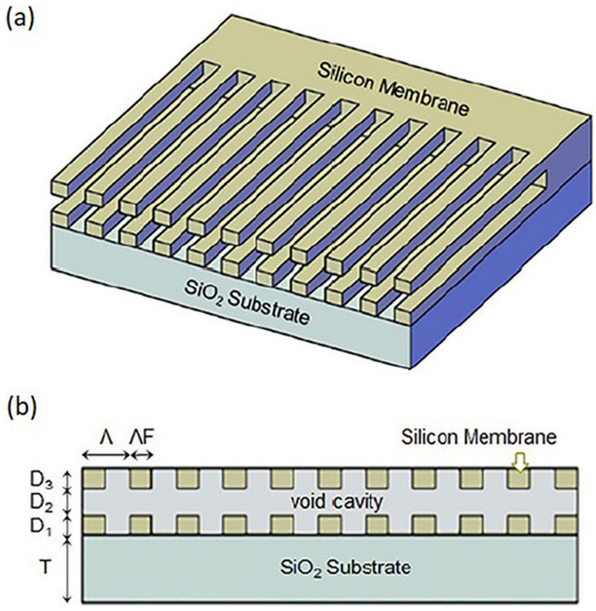

Fig. 4.4: **a)** 3D schematic view of the CHCG, made of silicon with SiO_2 substrate. **b)** Cross sectional view of the HCG. The bottom grating layer thickness D_1, the air gap thickness D_2, the top grating layer thickness D_3, the substrate thickness T, the fill factor F, and the grating period Λ are shown in the figure. This structure is supposed to be located in the gas chamber.

Although the intense electric field has not been confined completely in grooves, where the CO_2 exists, this amount of confinement could still lead to such improved absorption enhancement. Therefore, it is expected that it could lead to even further improvement. Later on, I found that by optimizing the substrate thickness T, which had been considered infinite so far, I could trap the light mostly in low-index areas. Our suggested explanation is that adjusting the thickness of the SiO_2 substrate provides us an additional tuning factor to further improve light confinement or waveguiding effect in the vertical direction, which leads to a strong constructive resonating effect that infinite substrate cannot provide.

Figures 4.6.a) and 4.6.b) show the absorption spectrum of the new CHCG design and a comparison between the enhanced absorption value of the SHCG,

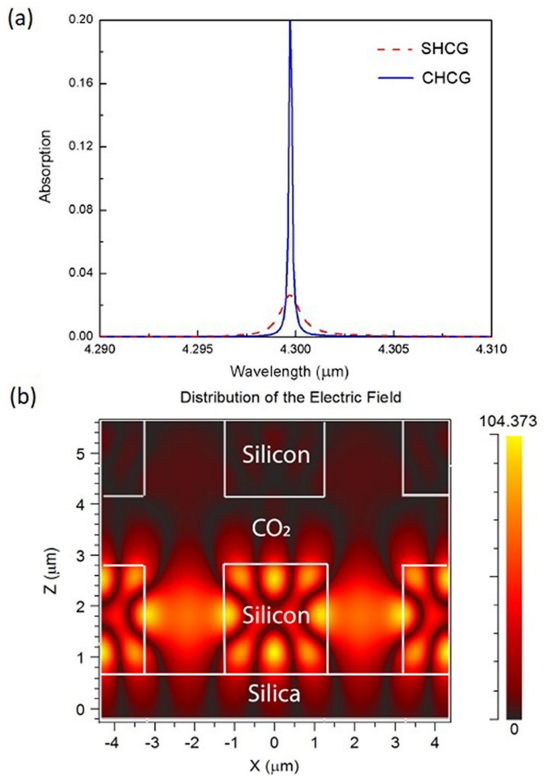

Fig. 4.5: **a)** Absorption spectra of CO_2 with and without CHCG from 4.29 μm to 4.31 μm; D_1=1.832 μm, D_2=1.14 μm, D_3=1.55 μm, T=infinite, Λ=4.336 μm, and F=0.5775. The bandwidth of absorption peak=0.25 nm. **b)** Intensity and distribution of the confined electric field at 4.3 μm on the CHCG. The colored bar shows the intensity of the electric field. unit $(V/\mu m)^2$.

the CHCG with an infinite substrate, and the CHCG with a finite substrate. In this new design, I optimized the substrate (the most bottom layer on which added layers are mounted) thickness. Through this new design (D_1=0.99 μm, D_2=1.15 μm, D_3=1.215 μm, T=1.149 μm, F=0.5325, Λ=3.6378 μm), I could increase absorption value to 1400 times of its initial value where there was no HCG. Figure 4.6.c) shows clearly the origin of this value of enhancement, which comes from trapping the intense electric field mostly in the gap between two grating layers. It should be mentioned although the fabrication of such a thin substrate is challenging, it is fortunately still possible due to advanced current technologies.

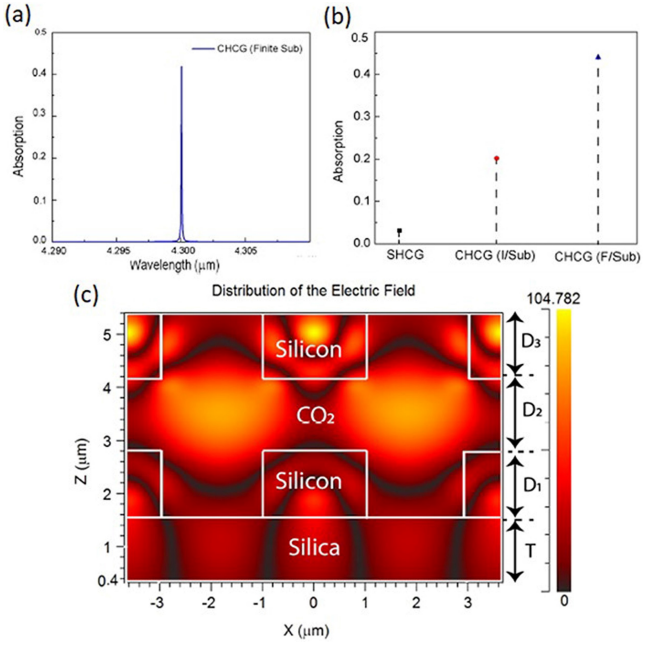

Fig. 4.6: **a)** Absorption spectra of CO_2, given by optimization CHCG with a finite substrate, from 4.29 μm to 4.31 μm D_1=0.99 μm, D_2=1.15 μm, D_3=1.215 μm, T=1.149 μm, Λ=3.6378 μm, and F=0.5325. The bandwidth of absorption peak=0.1 nm. **b)** Comparison between the absorption value of SHCG, CHCG with an infinite substrate, and CHCG with finite substrate. **c)** Intensity and distribution of the confined electric field at 4.3 μm on the CHCG with the finite substrate. The colored bar shows the intensity of the electric field. unit $(V/\mu m)^2$

In conclusion, I presented a theoretical approach to enhance light absorption by an increased light-matter interaction for CO_2 gas sensing applications. To attain this goal, I benefited from the unique properties of CHCGs for localizing an intense electric field in the gap between the two grating layers. In this study, I demonstrated the advantage of CHCGs and TE modes in confining the light with respect to a single layer of HCG. Hence, compared to SHCG, the optimized CHCG can increase light absorption by seven times. Generally, by utilization of the optimized CHCGs, which enables us to trap more intense light over the grating layer, I could increase the absorption value from 3×10^{-4} to 0.2. In other words, I improved the light absorption 600 times. Finally, by optimizing the

substrate thickness, I could confine the intense electric field mostly to low-index areas, which led to more effective light-matter interaction and 1400 times light-absorption enhancement. Our study demonstrated the capability of CHCGs in enhancing the light-absorption at the micro-size level and introduced a promising candidate for a new generation of on-chip absorption-based detectors which can be integrated into other photonic components in the future.

In Chapter 3 and Chapter 4 of the dissertation, the primary focus was on improving the performance of the photodetector and miniaturizing the gas sampling system, respectively. However, the upcoming chapter will shift the emphasis toward the third core component of gas sensors, which is the light source. In this next chapter, the objective will be to design a narrowband and low-cost light source in gas sensors. The theoretical investigation in Chapter 5 will revolve around an active photonic grating with a Parity-Time (PT) symmetric architecture. The optimization of gain/loss contrast and lattice constant parameters will be performed to achieve modulation of the active photonic system between the PT-symmetry and symmetry-broken phases. Unlike the commonly studied unidirectional properties, this theoretical work takes a fresh perspective by exploring new free-space emission modes within the active PT-symmetric photonic gratings. The findings from this research could potentially contribute to the development of novel low-threshold and super-coherent surface-emitting devices.

Chapter 5

PT-Symmetry Photonic Gratings for Enabling Nontrivial Light Sources

Understanding the capabilities and limitations of Mid-IR light sources is essential for optimizing their use in various optical sensing applications. Mid-IR light sources have gained significant attention due to their unique properties, which enable them to interact with specific molecular vibrational modes [152]. This interaction offers selective detection of molecular species by exploiting their characteristic absorption spectra. This specificity allows for highly sensitive and selective identification and quantification of target analytes [153]. Mid-IR light sources possess superior penetration capabilities, enabling the analysis of materials through coatings, films, and other barriers. This attribute facilitates non-destructive testing of samples while preserving their integrity [154]. Moreover, these light sources experience lower background interference from ambient light and scatter, contributing to enhanced signal-to-noise ratios and improved detection limits [155].

However, despite all mentioned advantages, the limited availability of suitable materials that exhibit transparency in the Mid-IR spectral range. This constraint often leads to higher costs and limited choices for light source designs [4]. Additionally, Mid-IR light sources often require high power levels, leading to

increased energy consumption and heat generation [152]. Effective heat dissipation and power management become critical considerations to maintain stable operation and prevent damage to the light source. Historically, Mid-IR light sources have been bulky and complex systems, making integration into compact optical sensors challenging [156]. The complexity and size limitations hinder their deployment in portable and miniaturized sensing platforms. Moreover, while some Mid-IR light sources offer tunability within a certain range, achieving broad tunability across the entire Mid-IR spectrum remains challenging. The ability to precisely tune the output wavelength of a Mid-IR light source to match specific absorption lines is crucial in many sensing applications [157].

Recent advancements in Mid-IR light source technology have focused on improving power efficiency while maintaining high output power. This involves optimizing the design and fabrication processes of QCLs and exploring novel materials for better performance [158], [159]. To address the size limitations of Mid-IR light sources, miniaturization techniques have been employed, including chip-scale integration of Mid-IR lasers, compact fiber-based sources, and micro-size photonic structures. These developments enable the integration of Mid-IR light sources into portable and handheld optical sensors [160]. Furthermore, researchers have made significant progress in expanding the wavelength coverage and tunability of Mid-IR light sources. Advances in laser diode technology and new semiconductor materials have extended the accessible wavelength range, enabling precise targeting of specific molecular absorption lines [161]. Moreover, broadband Mid-IR sources, such as Mid-IR frequency combs, provide coherent and broadband radiation that can be used for high-resolution spectroscopy and sensing applications [162]. These sources utilize

nonlinear frequency conversion techniques and offer comb-like spectra with evenly spaced frequency components.

Considering all recent advancements in performance enhancement and miniaturizing Mid-IR light sources still, there is room to address the aforementioned issues. For instance, QCLs, a dominant choice for Mid-IR sensing applications, indicating high power, tunability, and compatibility with semiconductor fabrication techniques, suffer from high cost and complexity. In the same way, thermal sources offer broad wavelength coverage. However, they tend to have limited power efficiency and require significant cooling mechanisms. Thus I aim to introduce a novel photonic structure toward the realization of low-cost and narrowband Mid-IR light sources.

PT-symmetric systems have shown great potential in light-emitting, such as single-mode lasing properties. The uniqueness of a PT-symmetric system lies in the beneficial role of optical loss, while in trivial systems, loss always has a destructive effect and should be eliminated. Among different photonic platforms for PT-symmetry studies, grating structures [73], [163]–[165], have also attracted some special attention due to their unique light control properties. By far, reported studies have mostly focused on asymmetric diffraction [73], and unidirectional properties [83] based on passive grating designs. Herein, I instead investigate an 'active' type of the PT-symmetric gratings and study the possible new non-trivial emitting properties besides the asymmetric diffraction effect.

This research will theoretically study the emission properties of diffracted modes from an active grating by the Helmholtz equation, driving the related matrix and indicating symmetry, symmetry-broken, and exceptional point regions. Moreover, numerically through the RCWA method, a non-trivial super-narrow emission will be stimulated, and its resonating properties induced

by PT-symmetric diffraction grating will be discussed in detail.

5.1 Theory and Analytical Solutions

As just mentioned, the guiding procedure in gratings lies in the spatial RI modulation. On the other hand, to realize the PT-symmetry, the RI modulation needs to satisfy $n(x) = n^*(-x)$. Therefore, the real part of RI modulation has to be a symmetric function, and its imaginary part should be an asymmetric function. Thus the RI modulation can be defined as:

$$n(x) = n_0 + n\cos(2\pi x/a) + i\gamma\sin(2\pi x/a) \tag{5.1}$$

where a is the period, n_0 is the effective refractive index, and n and γ are the real and imaginary parts of the refractive index modulation, respectively.

Figure 5.1.a) shows the real (solid blue line) and imaginary (dashed red line) parts of the PT-symmetric refractive index distribution. The positive part of the imaginary RI indicates gain, and the negative part shows the induced loss. Figure 5.1.b) displays the real part of the RI modulation in two dimensions where the RI solely changes in the x-direction, and the incident light is perpendicular to the periodicity. A_-, A_0, and A_+ show the amplitude of the -1, 0, and $+1$ orders of diffracted grating modes, respectively.

Here, I study the wave propagation of an incident light entering along the z-axis where the wave $E(x, z)$ obeys the Helmholtz equation [74], [166]:

$$\nabla^2 E + k_0^2 n^2(x) E = 0 \tag{5.2}$$

in which $k_0 = 2\pi/\lambda$. Since the incident light is normal to the periodicity, both x and z components are effective. The general solution for $E(x, z)$ can be derived

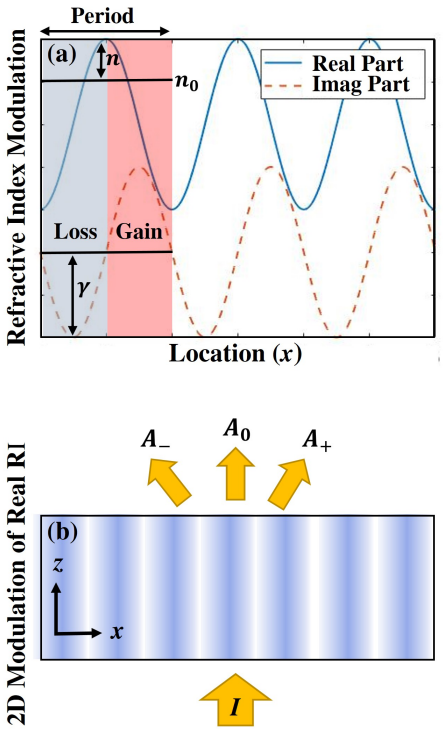

Fig. 5.1: **a)** Real and imaginary parts of a PT-symmetric RI modulation in the x-direction. **b)** Real RI modulation in x- and z-direction.

from Bloch's wave equation.

$$E(x,z) = u(x)e^{i\vec{\beta}.\vec{r}} \tag{5.3}$$

where $u(x)$ is a periodic function in the x-direction

$$u(x) = \sum_{m=-\infty}^{\infty} A_m e^{-i2\pi mx/a} \tag{5.4}$$

and in a 2D plane

$$e^{i\vec{\beta}.\vec{r}} = e^{i\beta_x x}e^{i\beta_z z} \tag{5.5}$$

By substituting (5.4) and (5.5) into (5.3):

$$E(x,z) = \sum_{m=-\infty}^{\infty} A_m e^{i\beta_z z} e^{i(\beta_x - 2\pi m/a)x} \tag{5.6}$$

Considering the normal light incident, the wavenumber in x-direction equals $2\pi m/a$, and consequently, the dispersion relation leads to:

$$\beta_z = \sqrt{k_0^2 n_0^2 - (2\pi m/a)^2} \tag{5.7}$$

If I consider the grating in a diffracted regime where $a >> \lambda$, β_z will be reduced to $\beta_z = k_0 n_0$. Thus, (5.6) can be rephrased as:

$$E(x,z) = \sum_{m=-\infty}^{\infty} A_m e^{-i[mKx - k_0 n_0 z]} \tag{5.8}$$

where A_m is the amplitude of the m_{th} diffracted mode, and $K = 2\pi/a$.

To analytically solve (5.2), in addition to $E(x,z)$ I need to find $n(x)$. Through (5.1), supposing n and γ are significantly smaller than n_0, the RI modulation can be rephrased as:

$$n(x) = \sqrt{n_0^2 + n_0[c^+ e^{iKx} + c^- e^{-iKx}]} \tag{5.9}$$

where $c^+ = n + \gamma$ and $c^- = n - \gamma$. Now, by substituting (5.8) and (5.9) into (5.2), and considering the Raman-Nath approximation the wave coupled equation (5.10) is obtained [163], [167], [168].

$$\frac{\partial A_m}{\partial z} + \frac{im^2 K^2 A_m}{2k_0 n_0} - \frac{ik_0}{2}[c^- A_{m+1} + c^+ A_{m-1}] = 0 \tag{5.10}$$

In contrast with Bragg gratings, in which only two first orders ($m = 0, 1$) at the Bragg angle show non-zero amplitude, higher orders can indicate non-zero amplitude in thin gratings. However, in this active PT grating work with a

normal incident light input, the amplitude of higher orders ($m = \pm 2$) are set to be significantly small [167]. Therefore, neglecting higher orders gives us a reasonable approximation of the exact solution and provides a clear insight into the PT-symmetry concept [163]. Hence, (5.10) is reduced to a set of coupled equations (5.11), which can also be written in a matrix form, shown in (5.12).

$$\begin{aligned} \frac{\partial A_0}{\partial z} - \frac{ik_0}{2}[c^- A_{+1} + c^+ A_{-1}] &= 0 \\ \frac{\partial A_{+1}}{\partial z} + \frac{iK^2 A_{+1}}{2k_0 n_0} - \frac{ic^+ k_0 A_0}{2} &= 0 \\ \frac{\partial A_{-1}}{\partial z} + \frac{iK^2 A_{-1}}{2k_0 n_0} - \frac{ic^- k_0 A_0}{2} &= 0 \end{aligned} \tag{5.11}$$

$$\begin{aligned} M \begin{bmatrix} A_{+1} \\ A_0 \\ A_{-1} \end{bmatrix} &= \frac{i\partial}{\partial z} \begin{bmatrix} A_{+1} \\ A_0 \\ A_{-1} \end{bmatrix} \\ M = \begin{bmatrix} \sigma & -k_0 c^+/2 & 0 \\ -k_0 c^-/2 & 0 & -k_0 c^+/2 \\ 0 & -k_0 c^-/2 & \sigma \end{bmatrix} \end{aligned} \tag{5.12}$$

where $\sigma = K^2/2k_0 n_0$. To solve the equation, the eigenvalues are obtained as follows:

$$\lambda_1 = \sigma \tag{5.13}$$

$$\lambda_2 = 1/2[\sigma + \sqrt{2k_0^2(n^2 - \gamma^2) + \sigma^2}] \tag{5.14}$$

$$\lambda_3 = 1/2[\sigma - \sqrt{2k_0^2(n^2 - \gamma^2) + \sigma^2}] \tag{5.15}$$

While λ_1 is independent of the real and imaginary parts of the refractive index

modulation, λ_2 and λ_3 are dependent on the real and imaginary parts. And once (5.16) is satisfied, the system will be located at its exceptional point, and λ_2 and λ_3 and their related eigenstates coalesce.

$$\gamma = \sqrt{n^2 + \frac{\sigma^2}{2k_0^2}} \tag{5.16}$$

Further, once the imaginary part of the refractive index modulation is $\gamma > \sqrt{n^2 + \frac{\sigma^2}{2k_0^2}}$, the system enters into the symmetry-broken phase, indicating imaginary eigenvalues. Figure 5.2.a) and figure 5.2.b) show the real and imaginary parts of eigenvalues according to the imaginary part of the refractive index (γ), where the dashed blue line indicates λ_2 and the solid red line displays λ_3. As we can see, in the symmetry region, both eigenvalues show a pure real value. However, immediately after the exceptional point, shown here by the dashed gray line, two eigenvalues bifurcates so that one of them possesses a negative imaginary part (λ_3) and the other one indicates a positive imaginary part (λ_2). It can be interpreted that one mode is trapped mostly in gain and the other one captured in loss and suppressed. The bifurcation is the most remarkable property of PT-symmetric systems [169], [170]. This unique property is used in designing single-mode lasers [63], [171], where undesired competing modes are captured in the loss and suppressed, and only confined modes in the gain are amplified.

In gratings that incident light is parallel to the periodicity (along x-direction in figure 5.1.b)), only the ratio between real and imaginary parts of the refractive index (n and γ) determines the phase of the system [87]. However, in our designed grating, where the incident light is perpendicular to periodicity, the period plays an essential role.

Figures 5.3.a) and 5.3.b) show the real and imaginary parts of eigenvalues

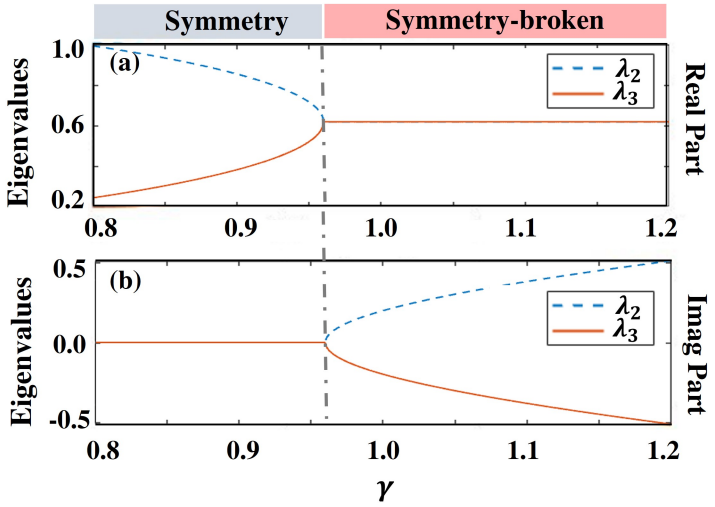

Fig. 5.2: **a)** Real part and, **b)** the imaginary part of eigenvalues according to the γ for a system with the periodicity of 2 μm. The exceptional point is shown by the dashed gray line.

according to different period selections, respectively. This figure indicates that increasing the period will drive the system into the symmetry-broken phase. The dashed gray line shows the location of the exceptional point. As reflected from the (5.16), in addition to real and imaginary parts of RI modulation, period and the effective refractive index can alter the system phase from symmetry to symmetry-broken phase. In other words, more design freedom exists in this unique active photonic grating platform.

This section analytically solved the Helmholtz equation for the dominant grating modes considering the Raman-Nath approximation. I showed the impact of the imaginary part of RI modulation and period to shift the system from a PT-symmetry phase to the symmetry-broken stage. In the following section, I will design a thin grating that follows the theory described above and report the unique PT-symmetric photonic modes solved numerically by the RCWA method. Moreover, the related electric field and amplitude distribution over the grating will be displayed, which will extend the understanding of physical

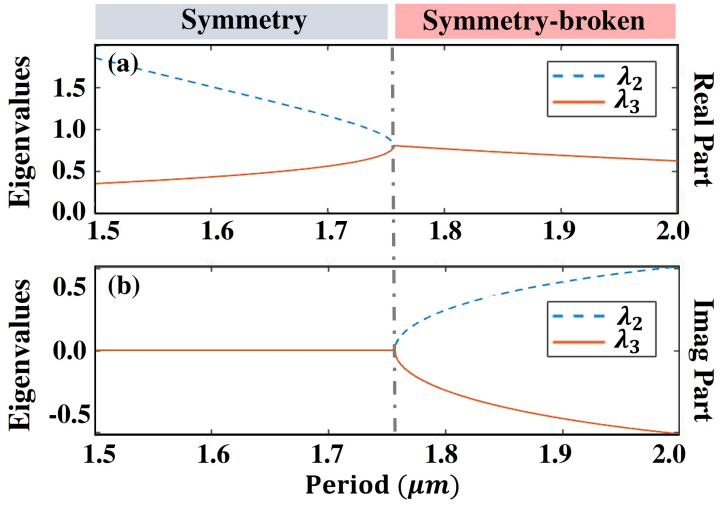

Fig. 5.3: **a)** Real and, **b)** the imaginary parts of eigenvalues according to the period for a PT-symmetric grating. The exceptional point is shown by the dashed gray line.

mechanisms leading to extraordinary phenomena observed in the active PT-symmetric photonic grating structures.

5.2 Numerical Simulations

Figure 5.4 presents both a 3D schematic of the PT grating structure, where yellow and red parts show the gain and loss ($|\gamma|$), as well as its cross-sectional setup for conducting the numerical simulation study in this section. It is noted that the InGaAs material system was adopted for the design and study of the PT-symmetric grating effects, considering their large optical gain and loss tunability and the well-established fabrication process for dimensional accuracy control. Also, it has been the primary choice for studying PT photonics [62], [63], [172] in the near-infrared range. It is noted that conclusions to be made can also be applied to other materials systems in other spectral domains. For example, antimony (Sb)-based III-V [173], [174] and lead-chalcogenide materials [26], [27], [175]–[177] can be options for in the mid-infrared active PT

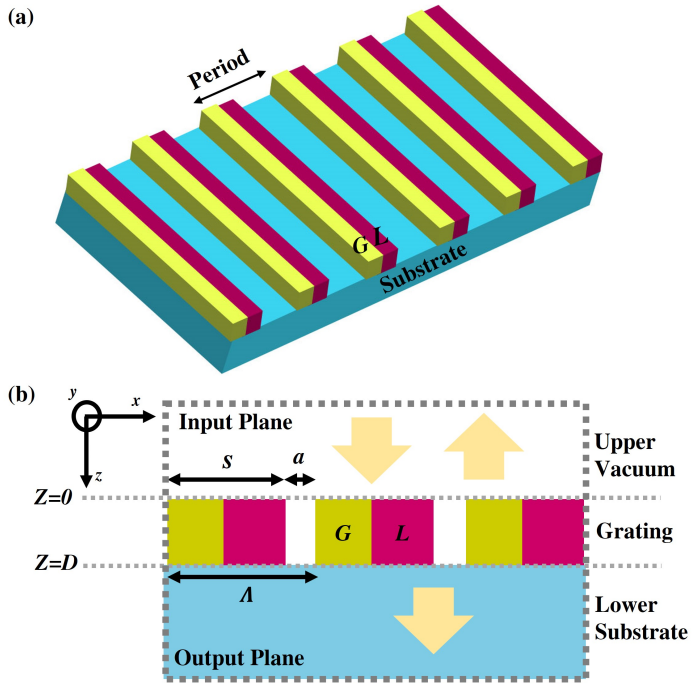

Fig. 5.4: **a)** 3D schematic of the PT-symmetric gratings; **b)** Cross-sectional schematic of the grating, showing three divided regions: the upper-half vacuum region, the grating region, and the lower-half substrate region. Λ, a, and s are the grating period, gap, and bar width.

exploration.

One of the most well-known criteria of PT-symmetric systems is the spatial bifurcation of two modes in the symmetry-broken region. As presented in figure 5.2, in the symmetry-broken phase, two modes with the same real part of eigenvalues show the bifurcation, where one is captured mostly in the gain other is trapped mainly in the loss. Thus, one mode is amplified while the other one is suppressed. This phenomenon is the primary mechanism behind the single-mode lasing in most of the PT-symmetric lasers. I expect that the numerical simulation demonstrates the same mechanism.

Figure 5.5 shows the spatial electric-field distribution over a grating with a period of 1 μm and a thickness of 821 nm. The substrate and gain/loss areas are demonstrated in this figure, where G stands for gain, and L stands for loss.

The grating parameters were selected in a way that satisfies the Raman-Nath approximation criteria (5.17) that was implemented in the theoretical section.

$$\begin{cases} Q'\zeta < 1 \\ Q' = \frac{2\pi\lambda d}{n_0\Lambda^2 cos\theta} \\ \zeta = \frac{\pi n d}{2\lambda n_0} \end{cases} \tag{5.17}$$

In (5.17), λ is the free-space wavelength, d is the grating thickness, n_0 is the effective refractive index, Λ is the grating period, n is the real part of the RI modulation, and θ is the incident angle.

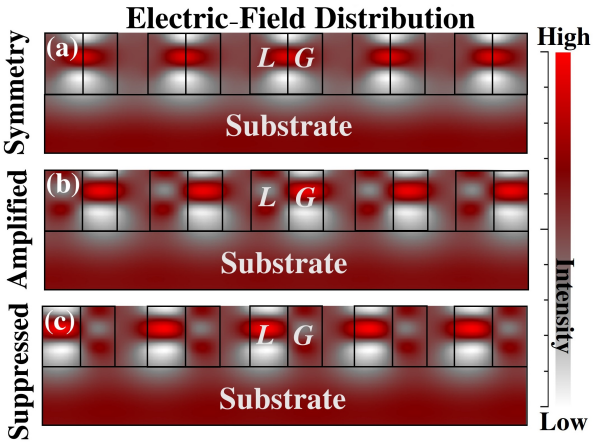

Fig. 5.5: Electric-field distribution over the PT-symmetric grating where **a)** $\gamma = 0.2$, associated with the symmetry phase. **b)** $\gamma = 0.22$ associated with the symmetry-broken phase (amplified mode). **c)** $\gamma = 0.22$ associated with the symmetry-broken phase (suppressed mode).

Figure 5.5.a) shows the symmetric distribution of the electric field over the gain and loss areas so that no mode experiences net amplification or suppression. This pattern can be associated with the PT-symmetry phase, where both eigenvalues are purely real. Increasing gain/loss (γ) from 0.2 to 0.22 shifts the system to the symmetry-broken phase, where one mode is captured in the gain and experiences the amplification. Figure 5.5.b) displays this mechanism clearly. However, the

other mode is trapped in the loss and is suppressed (figure 5.5.c)).

After indicating the bifurcation over the PT-symmetric diffraction grating, it is also found that the PT grating system can produce a non-trivial single-mode surface emission with a proper configuration of grating structure parameters and gain/loss contrast (γ). Figure 5.6 illustrates three surface-emitting spectra from the PT grating structure with a period of 1 μm, a fill factor of 0.55, and a thickness of 800 nm. Figure 5.4.b) shows the setup of our simulation model that includes three regions: the upper vacuum region, the middle grating region, and the lower substrate region. Considering the thicknesses of the upper and lower layers are generally multi-orders of magnitude higher than one of the middle grating layers, both of these two layers are set to be semi-infinite in our simulation. In addition, since the simulation path follows the input plane towards the output plane as indicated in figure 5.4.b), the upper vacuum space and lower substrate are also defined as the reflection and transmission regions. As such, the spectra in figure 5.6 are also noted as the transmitted emission spectra because they are observed from the substrate end ($Z = D$).

It should be pointed out that a similar single-mode PT emission can also be observed from the upper vacuum region, while the contributions from the diffraction orders are different. It is known that the cutoff condition [178] to prohibit the propagation of the higher ± 1 orders diffraction is $\Lambda < \lambda_0/n$, where Λ, λ_0, and n are period, free-space wavelength and refractive index, respectively [63]. In the upper-half vacuum region where $n = 1$, the wavelength (i.e., near 1.46 μm) is higher than the grating period (Λ=1 μm), which makes the ± 1 orders evanescent. Therefore, the high-Q emission observed from the upper region is solely contributed by the ground diffraction order. On the contrary, considering our semi-infinite substrate's $n = 1.47$ ($\epsilon > 2.1$), in the lower substrate region,

these two higher orders are not evanescent and allowed to propagate. Thus, the transmitted emission spectra in figure 5.6 are the combined emission effects from both the ground $m = 0$ and allowed ± 1 orders.

To better understand the dynamic of this non-trivial PT emission, I compared the diffraction efficiency of the transmitted modes in the logarithm scale, where $\gamma = 0.18$, $\gamma = 0.2$, and $\gamma = 0.22$. Figure 5.6.a) illustrates this comparison, where the solid blue line is related to the system with $\gamma = 0.22$, the dashed red line is associated with $\gamma = 0.2$, and the black dotted line is associated with $\gamma = 0.18$. The inset shows field amplitude distribution over a unit cell in a grating with $\gamma = 0.2$ and $\gamma = 0.22$. The magnitude of amplitude is displayed by the colored bar. Furthermore, figure 5.6.b), figure 5.6.c), and figure 5.6.d) show the 2D transmitted emission coefficient map over wavelengths, where γ changes from 0 to 0.18, 0.2, and 0.22, respectively. As we can see, the broadness of the mode decreases by increasing γ, which matches with the full-width half maximum of the spectrum in figure 5.6.a). The main reason for this significant difference is attributed to the intensity of the confined field in the gain area. The inset illustrates that the amplitude of the confined mode in the gain area for the grating with $\gamma = 0.22$ is almost 10^3 greater than the amplitude of the trapped mode in the gain for the same grating but with $\gamma = 0.2$. The physical mechanism for this extraordinary phenomenon has roots in the scattering theory in PT-symmetric systems, and the concept of spectral singularity [179]–[181].

Grating structures can be regarded as a typical scattering system in which the light propagation properties can be mathematically defined by using the scattering matrix function $\boldsymbol{S}$. Here, (5.18) shows a general $\boldsymbol{S}$-matrix (of dimension $n \times m$) that associates the amplitudes of incoming modes $(\phi_1 \cdots \phi_m)$ to the amplitudes of corresponding outgoing modes $(\eta_1 \cdots \eta_m)$.

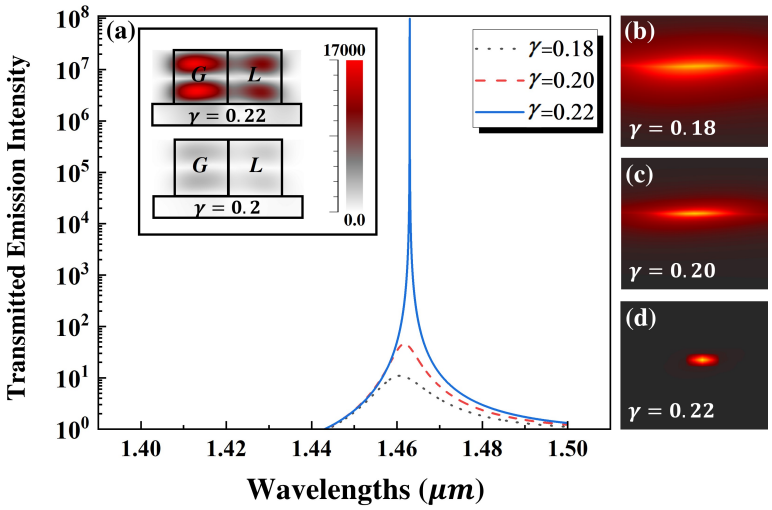

Fig. 5.6: **a)** Total transmitted spectra over wavelengths from the grating with $\gamma = 0.18$ (the black dotted line), $\gamma = 0.2$ (the red dashed line), and $\gamma = 0.22$ (the solid blue line), in the logarithm scale. The amplitude distribution of the spectrum with $\gamma = 0.2$ and $\gamma = 0.22$ is displayed over one grating period in the inset. The transmitted emission coefficient map over wavelengths where γ changes from 0 to **b)** 0.18, **c)** 0.2, and **d)** 0.22.

$$\boldsymbol{S}\begin{bmatrix}\phi_1\\ \vdots\\ \phi_m\end{bmatrix} = \begin{bmatrix}\eta_1\\ \vdots\\ \eta_m\end{bmatrix} \tag{5.18}$$

To solve eigenvalues of the $\boldsymbol{S}$ matrix, (5.19) should be satisfied, where $\boldsymbol{I}$ is the identity matrix, and λ stands for the eigenvalues of the $\boldsymbol{S}$ matrix. A required condition to define an $\boldsymbol{S}$-matrix is the unitary condition (|det $\boldsymbol{S}$|=1).

$$|\ \boldsymbol{S} - \lambda \boldsymbol{I}\ | = 0 \tag{5.19}$$

For passive structures with real frequencies, this unitary condition is only satisfied by having unimodular $\boldsymbol{S}$-matrix eigenvalues ($|\lambda_m|$=1) [182]. Applying the PT operator on $\boldsymbol{S}$-matrix meets the unitary condition. However, unlike

passive structures, the only way to meet the unitary condition in PT-symmetric systems is not having unimodular eigenvalues. In these systems, the unitary condition can be satisfied by pairs reciprocal moduli as well (λ_m=$1/\lambda_m^*$) [183]. The former possibility to satisfy the unitary condition is related to the PT-symmetry (unimodular eigenvalues), and the latter way (reciprocal eigenvalues) is associated with the PT-symmetry broken phase.

In the PT-symmetry broken phase, there are points at which poles and zeros of the $\boldsymbol{S}$-matrix intersect on the real axis [184], [185]. This intersection makes λ_m approach to zero or equivalently $1/\lambda_m^* = \infty$, while their product is still unity. In fact, such singular points are known as the spectral singularity, corresponding to an extraordinary amplitude enhancement of the transmitted emission modes. In this study, via optimizing the grating structure and the introduced optical gain/loss, the active photonic system reaches the vicinity of the spectral singularity, where its imaginary part of the complex frequency solution is almost zero [179], [186], [187]. Consequently, the non-trivial optical resonance rising from the active PT grating structure appears in the form of a high Q-factor surface-emitting single mode.

Figure 5.7 indicates Q-factors of the resonant mode (1.463 μm) with different introduced gain/loss (γ) to the grating. The calculation is based on the finite-difference frequency-domain method [188]. A sharp enhancement is observed when γ touches 0.22. This figure shows that only at a specific gain/loss value, here $\gamma =$ 0.22, spectral singularity can occur, and higher or lower values cannot satisfy the spectral singularity condition. This is matched with the theory that claims only at the spectral singularity point, where λ_m goes to zero while $1/\lambda_m^*$ goes to ∞. And the giant transmitted emission enhancement is related to $1/\lambda_m^*$, and its amplitude approaches infinity. Additionally, I want to point out that although such an ultra-

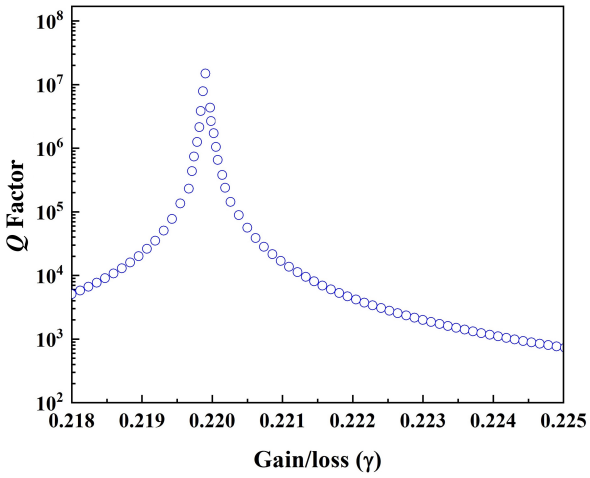

Fig. 5.7: Q-factor of the resonance mode in the logarithm scale with different introduced gain/loss (γ) to the grating.

high-Q mode ($> 10^7$) has been achieved by other passive structures, including whispering gallery cavities [189], and waveguide-coupled resonators [190], [191], they all carry multi-longitudinal modes and travel laterally in the same plane as their waveguides sit. The ultra-high Q mode in our work is uniquely created from the active material and emits in the direction perpendicular to the gratings, which can lead to a pathway to develop single-mode surface-emission laser devices. Moreover, in other mentioned works, the loss is considered an unwanted factor to be suppressed in order to achieve the high-Q performance. But here, due to the non-trivial properties of the PT-symmetry system, the loss becomes a beneficial role in providing fundamentally new freedom to manipulate light and stimulate the high-Q emission.

In conclusion, I reported a new active granting platform having the optical gain and loss to realize non-trivial PT-symmetry modulation effects. Herein, solving the Helmholtz equation in the Raman-Nath approximation indicated the bifurcation leading to confining the amplified mode in the gain region. I showed that in the PT photonic grating structure, in addition to the gain/loss parameter,

the period selection can also drive the system from PT-symmetry to the symmetry-broken phase. Moreover, a near zero-bandwidth photonic emission mode (i.e., at 1.463 μm) can be stimulated and numerically demonstrated through the RCWA simulation. It is suggested that, by optimizing the optical gain/loss contrast, this non-trivial high Q-factor resonance mode results from the photonic system's special spectral singularity effect, where one of the scattering states approaches zero while its reciprocal state approaches infinity. Considering the functionality of gratings in a broad range of applications, I anticipate introducing active PT-symmetric gratings will offer new engineering strategies for developing new low-threshold and super-coherent surface-emitting lasers and, thus, advancing modern on-chip photonic applications.

In Chapter 6, the focus will shift to discussing potential materials for fabricating the designed structures presented in the previous chapters, specifically for Mid-IR sensors. One promising candidate is PbSe Nanocrystals (NCs), which exhibit strong quantum confinement, a wide range of tunable bandgap energies, a large Bohr radius, and low Auger recombination rates and perform well at room temperature. The upcoming chapter will explore a new growth zone by conducting experiments with different pH values and preparation temperatures. The objective is to investigate the impact of growth time and control factors, such as the complex/cations ratio in the solution, on the growth mechanisms and film deposition. The utilization of high-quality PbSe NCs shows great potential in the development of optoelectronic devices operating in the Mid-IR range, including solar cells, infrared detectors, photonic sensors, and light emitters.

Chapter 6

Lead-Selenide-based Mid-Infrared Material Engineering

In recent years, considerable efforts have been devoted to developing on-chip Mid-IR sensors, to create transformative sensing capabilities in a compact form factor [192]. As a result, the performance of active Mid-IR light sources and photodetectors has been improved largely. Room Temperature operating Mid-IR laser sources (i.e., Quantum Cascade Lasers (QCLs) and Interband Cascade Lasers (ICLs)) [193]–[196] have been successfully realized on III-V group semiconductor materials platform. In the wavelength range from 3 to 5 μm, the specific detectivity (D^*) of Mid-IR photodetectors has reached 4×10^{12} Jones using IV-VI group lead salt semiconductors [107], [108], [197]. For longer wavelength ranges, improvements in the miniaturization for pyroelectric and thermopile detectors have also contributed to the reduction of price and footprint [198].

However, those technological advancements still have not reached the complete on-chip integration of a practical Mid-IR chemical sensor. Apparently, quantum-engineered III-V Mid-IR lasers offer incomparable performance and dominate light source markets for Mid-IR sensing applications. But also because of that, cost and integration challenges have been preventing the sensor development progress. Both QCLs and ICLs are made of precisely controlled

quantum-well and super-lattice structures, requiring the expensive and time-consuming Molecular Beam Epitaxy (MBE) ultra-high vacuum growth process. The room to reduce such costs is marginal. On the other hand, materials and substrates for low-cost non-cryogenic Mid-IR photodetectors (PbSe, HgCdTe, etc.) differ from those for QCLs/ICLs. Consequently, monolithic integration of critical elements (laser, photodetector, and gas cell) becomes almost impossible. From this point, exploring alternative solutions to overcome those challenges is essential.

I anticipate that lead salt materials could provide a possible new pathway for the on-chip gas sensor development. This group of direct narrow-band semiconductors has a high optical absorption coefficient and meager non-radiative Auger recombination rates [199]. By far, uncooled polycrystalline PbSe photoconductive detectors remain the primary choice for Mid-IR sensing applications operating in the 3-5 μm spectral range, thanks to their high detection performance [12]. Besides, they have excellent light emitting capabilities, especially at room temperature conditions [177], [200]. With this said, it is possible to fabricate both a light source and photodetector on one substrate for monolithic integration purposes. In addition, lead salts also have the highest refractive indices compared with other Mid-IR material groups. This is a unique and outstanding property for confining light in active waveguides to manipulate light and matter interactions. Thus, besides the emitters and detectors, the lead salt waveguide offers another key component for sampling gas molecules on chips.

With all these factors being considered, developing a sensing device in one chip based on lead salt materials is promising. Nevertheless, it is necessary to point out that, to conduct photonic design, the material morphology, and

geometry have to be well defined. However, polycrystalline lead salt materials prepared by the wet chemical process on amorphous substrates generally have random crystal orientations and very rough surface morphology comparable with the corresponding Mid-IR wavelengths. To overcome this technical hurdle, I introduce an experimental exploration for preparing highly uniform and oriented lead salt photonic nanocrystal films on glass substrates using a new hybrid wet chemical synthesis approach.

6.1 Introduction of Deposition Mechanism

Lead salts have various growth mechanisms in the chemical synthesis process [201], [202]. Two of the most commonly reported and thoroughly investigated mechanisms that could lead to film-to-substrate deposition are the Ion-By-Ion (IBI) growth and the cluster growth mechanisms. The IBI mode is a simple deposition process in which chemical reactions directly occur upon the substrate surface. This mechanism typically results in bulk films with irregular orientations. The cluster growth mode is a two-step process in which solid clusters precipitate in solution, diffuse to the substrate, and assemble into nanocrystal forms. This mode could produce highly dense and ultra-small quantum dot films. T. Templeman etc. [203] recently reported an intermediate Oriented-Attachment (OA) growth mechanism between IBI and cluster growth modes.

This new mechanism can produce highly uniformed (111) oriented PbSe microstructure films exhibiting low dimension quantum confinement effects covering a broad Mid-IR wavelength range from bulk 4.2 μm down to the Near-Infrared (NIR) range. However, the reported studies show the key role of the substrate in the OA growth mechanism [204]. Thus, all the given chemical deposited PbSe NCs, by the OA method, have been synthesized over GaAs (111)

or GaAs (100) [203]–[206]. However, to the best of our knowledge, the OA-grown PbSe was realized on the glass substrate, for the first time, in this study.

In the IBI mechanism, the reaction between free metal ions M^{n+} (in this case, Pb ions) and selenide ions Se^{2-} or, more probably, HSe^{-}, leads to the precipitation of metal chalcogenides (PbSe) when the ionic product is greater than the solubility product [201]. In this mechanism, crystals are synthesized directly from the substrate [207]. However, in the cluster growth, solid clusters precipitate in the solution and diffuse to the substrate [203]. In both mechanisms, the complex agents control the reaction rate [208]. In contrast to cluster-based nano-size crystals, IBI-based crystals are typically characterized by larger grains in the micrometer regime. The reaction process, leading to the IBI, and the cluster growth, is shown in (6.1) and (6.2), respectively [201], [205], [207].

$$\begin{aligned} SeSO_3^{2-} + OH^- &\rightarrow HSe^- + SO_4^{2-} \\ Pb^{2+} + HSe^- + OH^- &\rightarrow PbSe + H_2O \end{aligned} \tag{6.1}$$

$$\begin{aligned} 2SeSO_3^{2-} + H_2O &\rightarrow HSe^- + SeS_2O_6^{2-} + OH^- \\ Pb(OH)_2 + HSe^- &\rightarrow PbSe + OH^- + H_2O \end{aligned} \tag{6.2}$$

6.2 Experimental Setting

Two precursors are needed to deposit a thin layer of PbSe on the glass substrate: one for Pb cations and the other for Se anions. Moreover, sodium hydroxide (NaOH) is used as a complex agent to control the reaction's speed. As a Se precursor, a stock of sodium selenosulfate (Na_2SeSO_3) 0.2 M was prepared by refluxing 0.2 M of selenium powder (Aldrich, 100 mesh, 99.99% trace metals basis) with 0.5 M of sodium sulfite (Aldrich, BioUltra, anhydrous, $\geq$98% (RT)). The Na_2SeSO_3 solution was stirred at 90°C for 6 hours. Then, it was filtered to remove non-reacted selenium powder and was stored at 4°C. As a Pb precursor, 0.2 M lead (II) acetate trihydrate (Aldrich, $\geq$99.99% trace metals basis) was used.

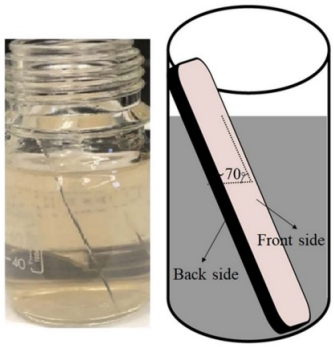

Fig. 6.1: Location of the substrate in the final solution.

Rectangular microscope slides ($3'' \times 1''$) were used as substrates, cleaned by solvent (acetone 55°C, methanol 25°C) and RCA bath (a mixture of 5 parts DI water, 1 part ammonia hydroxide, and 1 part hydrogen peroxide, 70°C/15min). To prevent adhering large particles to the growing films, they were deposited on the bottom face of the substrates at an angle of $\sim 70°$ with respect to the air–solution interface, as shown in figure 6.1. To prepare the deposition solution, first, the diluted lead acetate with a concentration of 48 mM was heated to reach 60°C. Then, by adding NaOH, the pH was controlled to be in the range of 9.5-10.1.

Afterward, the glass substrate is added to the Se-free solution. Finally, 48 mM of Na_2SeSO_3 was added to a 50 ml Pyrex beaker when the temperature of the final solution reached $\sim 62°C$. After adding Na_2SeSO_3, the reaction solution was removed from the hot plate. It is important to mention that the reaction solution was continuously stirred during the preparation.

In this research, the structural characterization of the deposited films was studied by X-ray Diffraction (XRD). The films' crystallographic phase and texture were studied by the Rigaku Ultima IV diffractometer. Data were collected in the 2Θ geometry using Cu Kα radiation (λ= 1.5405 A°) at 40 kV and 44 mA. Diffraction scans were taken for 120 minutes over the $2\Theta/\Theta$ range of 10°-70° with a step size of $\sim 0.2°$. The morphology of the films was observed via ultrahigh-resolution Ziess Neon EsB, which is a Scanning Electron Microscope (SEM). The acceleration voltage was 15 kV. Besides, Electron Backscatter Diffraction (EBSD), an SEM-based technique, provided more accurate crystallographic information compared to the XRD about the microstructure of the sample.

The optical characterization of the deposited films was studied by reflected, and Photoluminescence (PL) emissions were measured by a Bruker Invenio-R Fourier Transform Infrared Radiation (FTIR) spectrometer with a 16 cm^{-1} resolution. InSb high gain detector was cooled by liquid nitrogen. To decrease the thermal background, the PL module was combined with an external SR-830 lock-in amplifier. Excitation was achieved by a 980 nm laser. Moreover, to study the oxidation degree in different growth mechanisms, X-ray Photoelectron Spectroscopy (XPS) was used. The XPS was performed on a system equipped with Al Kα monochromatic X-ray source. A pass energy of 20 eV was used for high-resolution scans. The total number of scans is 10, with an energy step size of 0.05 eV.

6.3 Results Analysis and Discussion

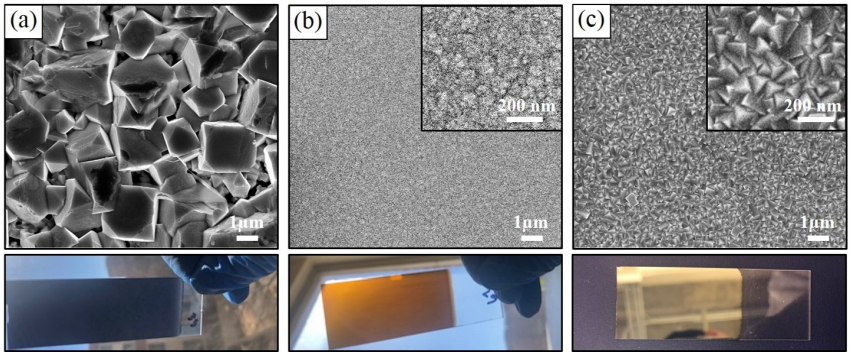

Fig. 6.2: Top-view SEM images of the PbSe thin film deposited by **a)** a poly-crystalline high-temperature bath deposition (IBI); **b)** a low-temperature quantum dots deposition (Cluster); **c)** the oriented-attachment growth mechanism. The appearance of the given films is shown beneath each growth method.

Figure 6.2 shows the top-view SEM images of three PbSe thin films deposited by different growth mechanisms, on glass substrates. Figure 6.2.a) indicates the IBI growth, featured by large grains. The rough surface of the given film by this method, shown below the SEM image, confirms the poly-crystalline nature of this sample. Figure 6.2.b) displays the morphology of the cluster-grown sample. The transmission of sunlight through this sample indicates the small size of the deposited NCs. Figure 6.2.c) shows a totally different morphology characterized by small pyramidal-shaped NCs. This film shows a shiny mirror-like look. From figure 6.2.c), it seems that the pyramidal-shape NCs are mostly oriented into (111) direction. To confirm this speculation, the EBSD analysis was performed.

Figure 6.3.a) shows the SEM image of the IBI-grown sample, and figure 6.3.b) indicates the given Kikuchi pattern, diffracted from sample (a). Each Kikuchi line is related to the Bragg diffraction from one side of a single set of lattice planes. These lines are marked with the Miller indices, which are used to identify individual diffraction spots [209], [210]. Furthermore, by scanning sample (a) on a 5×5 μm^2 grid, the EBSD orientation map in the form of a colored triangle is

overlaid (figures 6.3.c)). This legend, colored Miller map provides a visual display of the spatial and angular distribution of crystallographic directions. The colored bar indicates that NCs are mostly oriented in which direction. The blue region is the preferred orientation for NCs, while the red region is the least preferable. The SEM image, the Kikuchi pattern, and the EBSD orientation map of OA-grown film are shown in figures 6.3.d), 6.3.e), and 6.3.f), respectively.

As the given orientation map of sample (a) shows (figure 6.3.c)), the IBI-based NCs are mostly oriented into (001), and the (111)-oriented NCs are rare in the IBI-based sample, which considering lower surface energy of 100 facets, is not surprising. However, the orientation map of sample (d) shows an entirely different pattern. In this sample, the red zone is labeled by (001), which means, in contrast to sample (a), (001) is the least preferable direction for NCs. Compared to sample (a), (111)-oriented NCs increased and are almost equal to (101)-oriented NCs (both shown by green zone). Therefore, according to the EBSD analysis, I suggest sample (d), indicated by pyramidal-shape NCs, is grown by a unique oriented growth mechanism, different from IBI and cluster mechanisms. In the following sections, this mechanism will be thoroughly investigated.

After the crystallographic study, the optical properties of the films are then investigated here. Figure 6.4.a) and 6.4.b) present the reflection spectra of both the IBI-grown and OA-grown films, respectively (incident angle=60°). For the IBI-grown film, a clear intensity drops around 4.4 to 5 μm indicates the approximate location of the NCs' absorption-edge [211], [212]. However, because the thickness of the IBI-grown film is high (i.e., $\sim$ 1 μm), strong interference is introduced, resulting in a broadband modulation, which raises the difficulty of precisely determining the band-gap energy from the spectrum.

A simulation, thus, is performed, and a good agreement is found between the

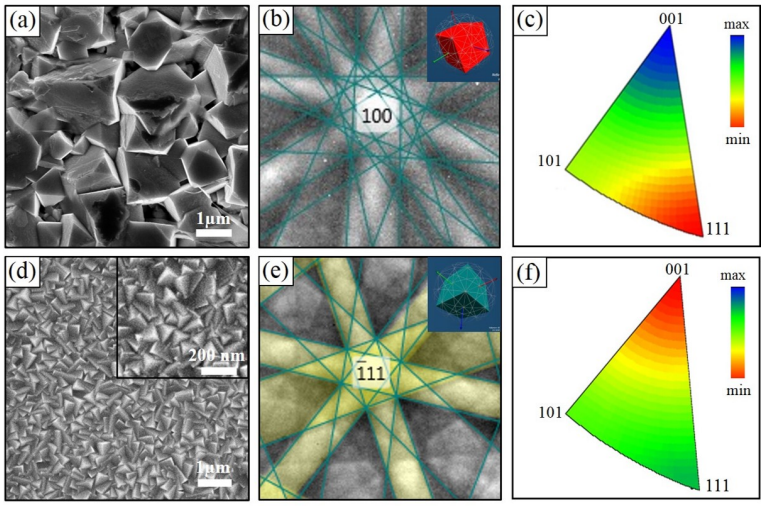

Fig. 6.3: **a)** Top-view SEM image of the PbSe thin film deposited by the IBI mechanism. **b)** Kikuchi pattern, diffracted from sample (a). **c)** EBSD orientation map of sample (a), taken on a 5×5 μm^2 grid. **d)** Top-view SEM image of the PbSe thin film deposited by the OA mechanism. **e)** The Kikuchi pattern, diffracted from sample (d). **f)** EBSD orientation map of sample (d), taken on a 5×5 μm^2 grid. Insets show a 3D view of (100)-oriented NCs (red cube), and (111)-oriented NCs (blue cube).

simulation and experimental results, indicating that the band-gap of the film is around 4.4 μm. In terms of the thin OA-grown film with a thickness of $\sim$ 300 nm, the interference can not be obviously seen in Figure 6.4.b). Hence, the absorption-edge can be clearly located at the wavelength close to 3 μm. To further confirm the results, PL measurements are also performed. Figure 6.4.c) indicates the comparison of the normalized PL emissions given by OA and IBI deposited films. The PL peak position of the IBI sample is around 4.4 μm, which is a good match with the given results from the sample reflection. In comparison, the peak position of the OA-grown film has blue-shifted to 3 μm. This blue-shifting indicates the reduction of the NCs' size, leading to the enhanced quantum effect.

In order to understand this newly-discovered unique OA growth mechanism, the growth rate and the related morphology changes are systematically studied. Figure 6.5.a) shows the extracted growth rate by measuring the film thickness at

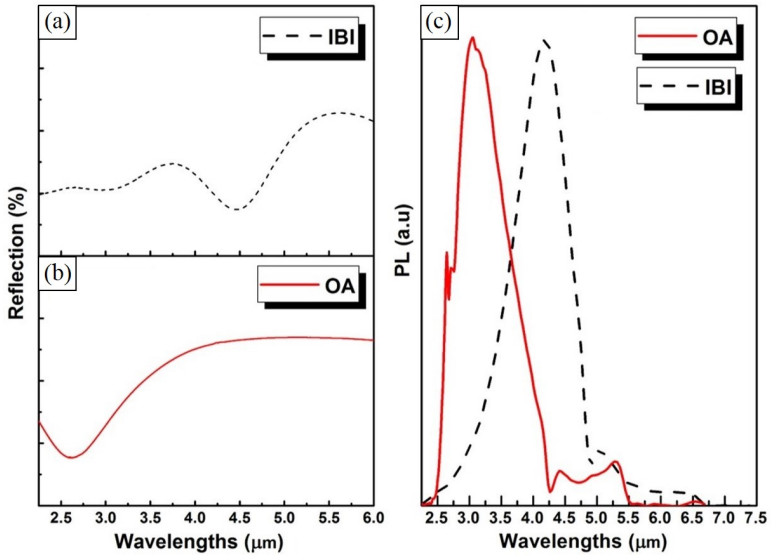

Fig. 6.4: **a)** Reflection of the IBI-grown sample in the Mid-IR optical range. **b)** Reflection of the OA-grown sample in the Mid-IR optical range. **c)** Normalized PL emissions given by OA and IBI samples.

different time intervals. The dramatic change in the growth rate, starting at 3rd minute, indicates the transition of the growth mechanism from the cluster to the OA. This transition is accompanied by a change in the film morphology.

Figure 6.5.b) displays the morphology of the film deposited for three minutes. This film is characterized by the small spherical NCs, which is a typical cluster growth morphology. However, the morphology of this film is entirely different from the film deposited for 6 minutes under the same condition (figure 6.5.c)). Only in three minutes (growth time: 3 minutes to 6 minutes), the growth mechanism transits completely from the cluster growth to the OA mechanism. As figure 6.5.a) indicates, at 6th minute of growth time, there is another sharp change in the growth rate. Thus, the growth rate dramatically decreases. However, the growth rate reduction stops after 4 minutes, when the growth time is 10 minutes. Afterward, the film thickness increases with a constant rate (2.5 (nm/min)). Figure 6.5.d) shows the deposited film in 20 minutes. Apparently, the film morphology converts

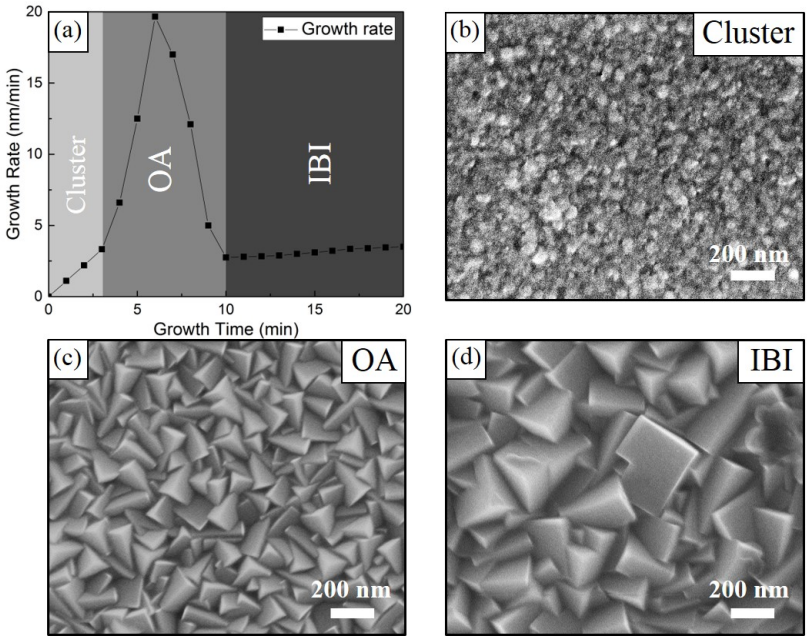

Fig. 6.5: **a)** Plot of the growth rate as a function of growth time, labeled by three different growth mechanisms. Top-view SEM imaging of the films deposited at 45°C, pH∼10, for **b)** 3 minutes; **c)** 6 minutes; **d)** 20 minutes.

from the oriented pyramidal-shape to the poly-crystalline cubic-shape, which is a common morphology for the IBI mechanism.

The time-dependency of the growth rate and the related morphology changes may be attributed to the concentration of free ions in each stage of the reaction. In our study, the Pb precursor is added first, followed by adding NaOH complex, and the Se precursor is added as the final step to the hot solution (62°C). Thus, it appears that in the initial stages of the reaction (in 3 minutes), Se^{2-} ions do not have enough time to release in the solution. Therefore, the lack of free Se^{2-} may limit the growth rate and keep the growth mechanism in the cluster regime [201]. Moreover, the formation of hydroxide clusters can be another reason that limits the free Se^{2-} ions [203]. However, in a short time, the released OH^{-} ions accelerate the process of Se^{2-} ions relief, which leads to a dramatic rise in the growth rate. The high temperature of the final solution facilitates sharp changes

in the growth rate. As the deposition proceeds, due to the formation of PbSe, Pb^{2+} ions are removed from the solution. Thus, the complex/Pb^{2+} ratio increases, leading to the growth transition to the IBI mechanism [201].

Generally, the free OH^- ions in the final solution have two competing roles. On the one hand, higher OH^- ions limit available free Pb^{2+} cations, on the other hand, they induce decomposition of Na_2SeSO_3 and release more Se^{2-} ions [213]. Therefore, due to the fast changes in the growth rate, resulted from OH^- ions variation, this unique OA mechanism is observed only in a narrow window, where the free OH^- ions are in the optimum amount.

As I mentioned, the consumption of free Pb^{2+} cations during the reaction leads to converting the OA growth to the IBI mechanism. Therefore, refreshing the solution to compensate the consumed free Pb^{2+} should keep the growth mechanism in the OA regime. Figure 6.6 approves this explanation. Figure 6.6.a) shows the top-view SEM imaging of the film, which was deposited for 56 minutes in total. However, every 8 minutes, the reaction solution was refreshed. The replenishing of the solution was repeated seven times. In comparison to this successive film growth, figure 6.6.b) indicates the morphology of the film, deposited 1 hour continuously, without replenishing the reaction solution, under the same condition. The transition growth mechanism from the OA growth to the IBI is evident. It is worth to note that the successive growth enables us to synthesize OA-deposited films up to 850 nm in thickness.

As I mentioned, during the reaction, changes in the number of free OH^- ions play a crucial role in the transition of the growth mechanism. Therefore, the amount of added NaOH, in the first place, during the preparation of the reaction solution, should have a substantial impact on the growth mechanism as well. During the preparation, I noticed that depending on the amount of added NaOH,

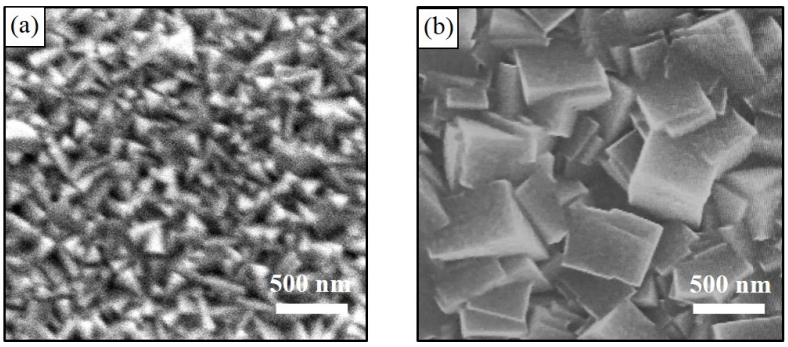

Fig. 6.6: Top-view SEM imaging of **a)** the successively grown film deposited at 30°C, pH 9.9, (7 runs, each run 8 minutes); **b)** the deposited film at 30°C, pH 9.9 for 60 minutes, 1 run.

the color of the solution changes. Thus, the reaction solution remains transparent when I add 0.4 M of NaOH. However, adding 0.3 M of NaOH leads to synthesizing shiny solids, which are suspended in the solution. When I decrease the amount of NaOH to 0.2 M, instead of the small suspended crystalline particles, huge agglomerated solid crystals settle down to the bottom of the reaction solution, and the solution becomes semi-transparent.

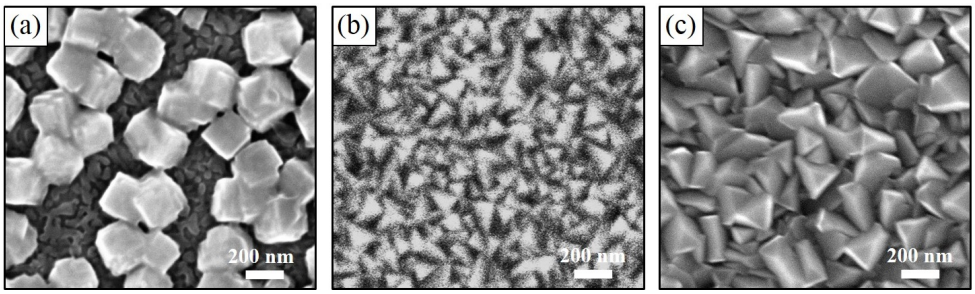

Fig. 6.7: Top-view SEM imaging of the film deposited at 40°C, for 10 minutes, when **a)** added NaOH=0.4 M; **b)** added NaOH=0.3 M; **c)** added NaOH=0.2 M.

The top-view SEM imaging of these three samples is shown in figure 6.7. The SEM image of the film, deposited by the highest amount of NaOH (figure 6.7.a) shows cubes randomly oriented over a layer of small connected dots. It seems that in this sample, IBI and cluster mechanisms have been initiated simultaneously. Probably, the high amount of NaOH increases the possibility of having more free

OH^- ions, consequently few free Pb^{2+} cations, in the first stage of the reaction, which is in favor of IBI mechanism [201]. However, the lack of free Se^{2-} ions in the first minutes of the reaction will favor the cluster deposition [201]. Thus, it seems that the high amount of added NaOH has blocked the narrow window of realizing the OA mechanism (figure 6.5.a)).

However, when the amount of added NaOH is 0.3 M (figure 6.7.b)), the OA mechanism is completed in ten minutes. The responsible process for this mechanism has been thoroughly explained in the growth rate section (figure 6.5), where the cluster mechanism completely transited to the OA mechanism during the reaction. The observed suspended crystalline solids during the preparation may be attributed to the lead hydroxide [201]. It is noted that the color change of the reaction solution slightly to light green during the preparation stage is critically important to ensure the success of the growth. I notice that this phenomenon is caused by the uncapped operation. Thus, it is suggested that CO_2 in the air could dissolve to the solution and contribute to the growth. The involvement of CO_2 in the chemical deposition of PbSe NCs has also been observed in other studies previously [201]. I believe that CO_2 help release free OH^- ions, which promotes the synthesis of solid lead hydroxide in the Se-free solution.

In the third scenario, when the amount of added NaOH decreases to 0.2 M, likely, the possibility of having more free OH^- ions, in a Se-free solution decreases. It seems that this low amount of free OH^- accelerates the relief of Pb^{2+}. Maybe this high amount of free Pb^{2+} reacts with the existing OH^- ions, resulting in agglomeration of lead hydroxide crystals, before adding selenosulfate. In comparison to sample (b), the pyramidal-shaped grains of sample (c) enlarged. This comparison suggests that decreasing added NaOH

leads to enlarging the grain size. Our potential explanation for this behavior suggests that the significant amount of lead hydroxide, synthesized in the form of agglomerated crystals in the Se-free solution, may limit free Pb^{2+} cations in the final solution, which is in favor of enlarging the grain size. Thus, in a reaction solution with a lower amount of NaOH, the transition of the OA to the IBI mechanism starts in the earlier stages of the reaction.

I noted during the preparation when selenosulfate is added to the mixture of Pb acetate and NaOH, at different temperatures, the appearance of the given films looks different. I called this temperature the preparation temperature, which is different from the growth temperature. Figures 6.8.a), 6.8.b), and 6.8.c) show the morphology of the deposited films in three different preparation temperatures. Moreover, the related PL peak position of each film is plotted in figure 6.8.d).

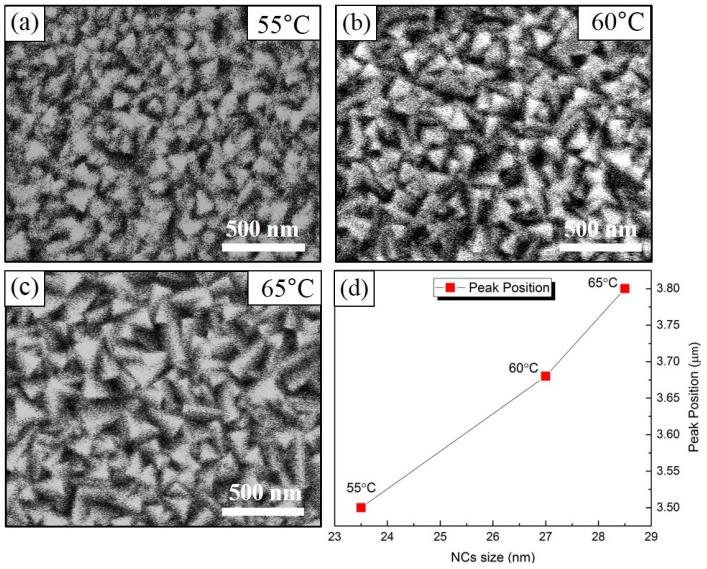

Fig. 6.8: Top-view SEM imaging of the film deposited at 45°C, pH∼9.8, for ten minutes when the preparation temperature is **a)** 55°C, **b)** 60°C, and **c)** 65°C . **d)** The plot of size-dependent PL peak position of the deposited films.

All deposited films featured pyramidal-shaped grains, indicating the OA growth mechanism. However, comparing the SEM image of sample (a), (b), and

(c) suggests that the grain size increased slightly by increasing the preparation temperature. Furthermore, figure 6.8.d) shows that 10°C rise in the preparation temperature expands NCs around 5 nm, resulting in a 300 nm red-shift in the PL peak position. The red-shift has directly resulted from the size-dependent property of the PbSe energy band-gap [25]. Moreover, by controlling the size of NCs, the PL emission was tuned over the range of [2.8-3.75 μm], the important optical range containing the molecular fingerprint of trace gases such as CO_2 and methane [23].

Furthermore, in order to obtain a better understanding of the OA-grown films, the XRD analysis of three films, deposited by three different growth mechanisms is performed. XRD analysis reveals more information about the structure of NCs, synthesized under different growth mechanisms. Figures 6.9.a) and 6.9.b) show the SEM image and the XRD patterns of the cluster-deposited film, respectively. Figures 6.9.c) and 6.9.d) display the SEM image and the XRD patterns of the IBI-deposited film, respectively. Besides, figures 6.9.e) and 6.9.f) indicate the SEM image and the XRD patterns of the OA-deposited film, respectively. The crystal's orientations are displayed next to each peak.

The XRD pattern of the cluster-grown sample (sample (a)), indicates two peaks at 44.1° and 64.8°, which, according to International Center Diffraction Data (ICDD), may relate to (202) and (222) facets of the orthorhombic phase of PbSe. The XRD pattern of the IBI-grown sample (sample (c)) shows ten distinct peaks. According to ICDD, I found a good match between eight peaks of the cubic phase of PbSe. These phases are depicted in figure 6.9.d). However, it seems that the two peaks displayed by the black dashed lines are not related to the cubic phase of PbSe. The position of these two peaks (black dashed line) is matched with the position of the (202) and (222) facets of the orthorhombic

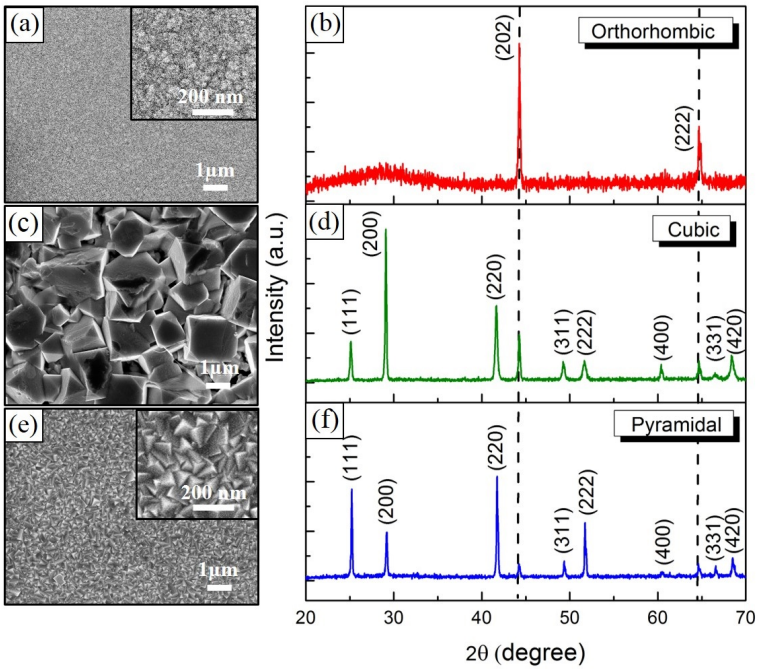

Fig. 6.9: **a)** SEM image of the cluster-based film. **b)** X-ray diffraction patterns of sample (a). **c)** SEM image of the IBI-based film. **d)** X-ray diffraction patterns of sample (c). **e)** SEM image of the OA-based film. **f)** X-ray diffraction patterns of sample (e).

phase of PbSe (sample (a)). As we can see, the dominant orientation in sample (c) is (200), which is in good agreement with the given result from EBSD analysis (figure 6.3.c)). Finally, the XRD pattern of the OA-grown sample (sample (e)) is shown in figure 6.9.f). This sample shows all peaks that appeared in sample (c); however, the peak intensity is different. Versus sample (c), (111)-oriented NCs are significantly increased in sample (e). However, (200)-oriented NCs are suppressed, and (220)-oriented NCs are fairly enhanced.

The existence of orthorhombic-related peaks in XRD patterns of all three samples (black dashed line), which are weak in sample (c) and (e), suggests the presence of a sub-interfacial cluster layer. The signs of the existence of this interfacial layer have already shown in figure 6.5.b), where the three minutes-grown sample displays the cluster-deposited morphology. Compared to

sample (c), suppressing (200)-oriented NCs and improving (111)-oriented NCs in sample (e), indicates a clear oriented growth transition. Furthermore, (111) and (220) facets of the cubic phase of PbSe may evolve from (222) and (202) facets of the orthorhombic phase of PbSe. Lastly, since XRD is performed over 5×5 mm^2, which is a large area, probably, the (200) peak of sample (e), originates from the contamination on the surface, which is not captured by the taken SEM image. Since the EBSD orientation map from sample (e) is scanned over a much smaller area (5×5 μm^2), I expect the contamination-related peak to be suppressed. Figure 6.9.f) by showing the minimized (001) orientation would confirm this claim.

6.4 New Growth Model Discussion

It seems that investigating each effective factor in the growth mechanism revealed a missing piece of a puzzle, which guided us toward a comprehensive understanding of the unique behavior and morphology of the OA growth. The XRD analysis, as the final piece, completed this puzzle. The XRD analysis suggested the existence of an interfacial PbSe orthorhombic seed layer, which acts as a foundation for the OA growth. Moreover, I discovered that the shiny particles, synthesized in the Se-free solution, are lead hydroxide crystals, which were not observed in the high-pH solutions. Furthermore, I realized the preparation temperature plays a crucial role in controlling the grain size in the OA growth mechanism. Besides, I found out that the order of adding precursors possesses high importance. Hence, when Se precursor is added first, no OA growth activates.

A new growth model is then proposed to offer a theoretical explanation and experimental guideline (figure 6.10). According to this model, the low pH value and the high preparation temperature lead to bonding Pb^{2+} cations to the free

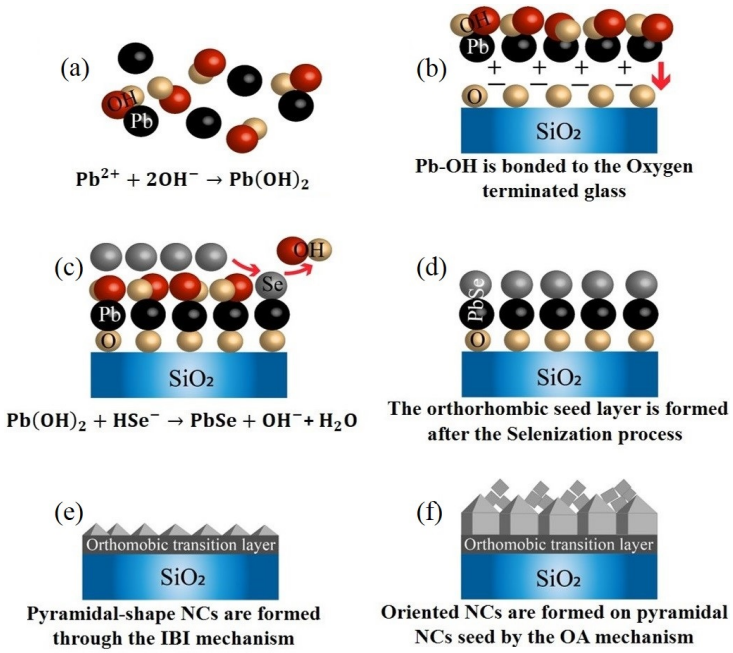

Fig. 6.10: Steps of the suggested growth model for the unique OA growth on the glass substrate; **a)** Forming lead hydroxide in the Se-free solution. **b)** Bonding lead hydroxide with the oxygen-terminated glass. **c)** Starting the Selenization process. **d)** Forming a seed layer of orthorhombic PbSe NCs. **e)** Synthesizing pyramidal-shaped NCs on top of the seed layer by IBI growth. **f)** Synthesizing OA NCs from (100) faces of pyramidal facets.

OH^- in the Se-free solution (figure 6.10.a)). The reason for emphasizing the low pH and the high preparation temperature is increasing the possibility of forming $Pb(OH)_2$. Thus, when the amount of added NaOH is too high, or similarly, the preparation temperature is not high enough (less than 45°C), the suspended shiny particles, which I presume are $Pb(OH)_2$, were not observed, in the Se-free solution. After forming $Pb(OH)_2$, the clean glass is added to the Se-free solution. In this step, the oxygen-terminated glass attracts the free lead hydroxide, in a way that the surface is terminated by hydroxide (figure 6.10.b)). In the third step, the Se precursor is added to the solution (figure 6.10.c)). Thus, through the substitution of Se^{2-} ions with hydroxide ions, the Selenization process starts in this step. In step (d), all lead hydroxides get Selenized, and an orthorhombic

layer is formed. The sign of the existence of this layer is evident in the OA and the IBI mechanisms (black dashed lines in figure 6.9). I suggest that this thin film acts as a seed layer, and when the IBI growth mechanism is activated, cubic PbSe crystals tend to align with the seed layer's crystal orientation (i.e., (111) and (101)). This critically important growth step is shown in figure 6.10.e). On top of these oriented IBI NCs array, the later on activated OA growth mechanism will then assemble the cubic crystallites along with the bottom 100 faces (figure 6.10.f)). The growth mechanism is similar to the reported work by Templeman and et al. [203].

To conclude, OA-grown PbSe NCs were chemically synthesized directly on amorphous glass substrates, for the first time. By exploring a new domain of the pH value and the preparation temperature, a new growth zone is revealed, in which the OA growth can be realized on the amorphous glass substrate. The growth time is found to be another important factor that can control the transition of the growth mechanisms among the cluster, IBI, and OA by design. Furthermore, control factors, such as the complex/cations ratio in the solution, also play a crucial role in synthesizing OA-deposited films. More importantly, a comprehensive growth model is developed through the study of these dynamic parameters, which offers a clear theoretical explanation and growth guideline for this new method. Lastly, I anticipate that this new material synthesis finding will open a new pathway to advance a wide range of optoelectronic devices, such as solar cells, infrared detectors, photonic sensors, and light emitters, operating at the Mid-IR range.

In the upcoming chapter, I will delve deeper into design and material preparation by exploring methods for photonic patterning. One such method is Laser Interference Lithography (LIL), a low-cost technique capable of fast and

on-chip large-area patterning. Furthermore, I investigate the application of the Reactive-Ion-Etching (RIE) method on the PbSe material. This method poses a challenge due to the low volatility of the Pb compound, which can form undesirable etching gas compounds. To overcome this issue, I introduce a novel solution to address the charging effect on the RIE-etched profile, ensuring a smooth and precise etched profile. These explorations and developments aim to optimize the fabrication process, enabling the realization of high-quality structures for Mid-IR sensors and other optoelectronic devices.

Chapter 7

Experimental Investigation of the Large-Area Patterning Method for Grating Fabrication

This chapter focuses on the fabrication process of PbSe-based gratings. Herein, I discuss experimental settings including cleaning procedures, lithography methods, and etching systems. Then, in a separate section, I elaborate on lithography techniques and the optimization of the Reactive Ion Etching (RIE) method to etch PbSe gratings. Moreover, I present a study of the ion charging effect to improve the RIE-etched profile of grating structures. In this study, I show the impact of Cu hard mask to neutralize the charging effect leading to sub-micro-size etch profiles.

7.1 Sample Prepration

As I mentioned in the introduction, the high Q-factor modes shown by HCGs are highly sensitive to the size-fluctuation. Thus, providing a smooth surface and high-quality materials is crucial. Figure 7.1 displays the Full Width at Half Maximum (FWHM) changes due to the introduced roughness (RMS). This figure shows that in an ideal case with zero roughness, the FWHM is 0.01 nm, while this value can reach 0.7 nm for a sample with 50 nm of roughness. As we can see, FWHM is a logarithm function of roughness, and the FWHM of a sample with

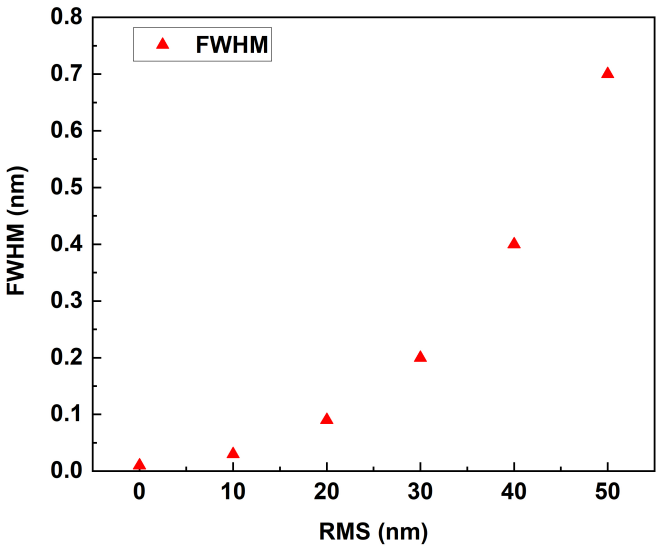

Fig. 7.1: Numerical simulation of FWHM changes due to the introduced roughness (RMs). 10 nm, 20 nm, 30 nm, 40 nm, and 50 nm are introduced.

100 nm roughness extends to 4 nm.

To make sure our deposited thin PbSe films by the OA method, are smooth enough to show the mode from the designed HCG, an AFM image has been provided. Figure 7.2.b) shows the AFM image of sample (a). From this photo is evident that each pyramidal-shape grain (size $\sim$ 100 nm) is composed of smaller agglomerated crystals (size $\sim$ 25 nm). Moreover, figure 7.2.c) shows a 3D view of the sample (a) taken on a $0.75 \times 0.75\ \mu m^2$ surface. The given RMS roughness of this sample is 7.71 nm. This roughness increases the bandwidth $\sim$ 2 times, compared to zero roughness, which still shows the high Q-factor ($\sim 10^6$). However, in each round of OA deposition, the PbSe film thickness is around 150 nm. Therefore, to reach 1 μm thickness of the PbSe, the deposition should be repeated 7 times, and in each round, the roughness increased accordingly.

To address this issue, I suggest a hybrid method, in which I deposit 850 nm of a thin PbSe film by the sputtering method, use this sample as a seed layer, and

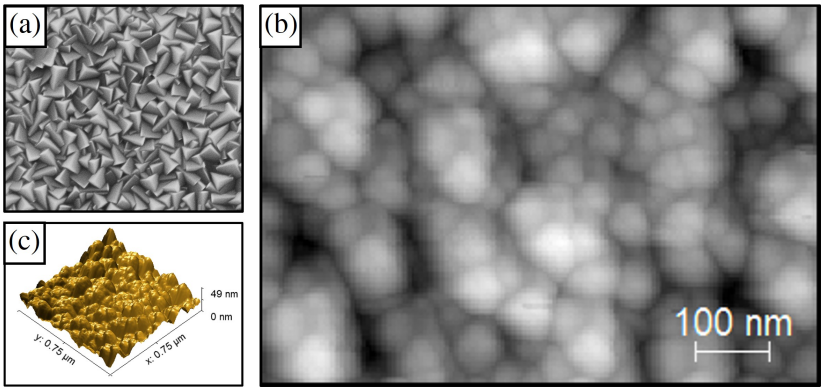

Fig. 7.2: **a)** SEM photo and **b)** AFM photo of the OA-deposited sample. **c)** 3D view of the sample (a) taken on a 0.75×0.75 μm^2 surface.

follow the OA method to deposit a 150 nm thick layer of PbSe. In this way, I have the same roughness of only one round of OA deposition and the comparable PL intensity. It should be noted that, without the OA deposited layer, sputter-deposited samples show no PL emission at room temperature.

7.2 Experimental Settings

In this research, I designed a set of grating structures with different slot sizes to study the effect of the gap width. For etching grating patterns, I used PbSe thin films with a thickness of 1 μm, depositing with oriented attachment (OA) chemical solution method on glass substrates. The details of the growing process have been explained in this research [27]. Before applying the photoresist, I ultrasonic cleaned the sample in acetone for three minutes, followed by a three-minute ultrasonic clean in Isopropanol alcohol (IPA), and finished by rinsing the sample in deionized (DI) water and drying the sample using ultra high purity (UHP) nitrogen gas. Herein, I used positive (AZ 1505, 0.5 μm thickness) and negative (AZ nLOF2020, 2 μm thickness) photoresists. For negative photoresist, I coated the sample with HMDS to improve photoresist

adhesion. I soft-baked the sample for one minute at 110 C°. I utilized several lithography methods in this study, including direct writing photoresist by PG-101 Laser, the MJB3 mask aligner, and interference lithography. The related details of each method will be explained in a separate section.

In this study, I used the Trion ICP-RIE plasma etching system (Trion Technology). The reactor chamber was pumped down to less than 1.5×10^{-5} Torr. The RIE was performed in $CH_4/H_2/Ar$ plasma atmosphere, where the gas flow rate was controlled by mass flow controllers [214]. After completing the etching process, the structure was exposed to oxygen to improve photoresist removal. After finishing the etching process, to completely remove the photoresists, I ultrasonic the sample in acetone and IPA for three minutes, respectively, and finished by rinsing the sample in DI water and drying it with UHP nitrogen gas.

I used Lesker Nano36 Evaporator to grow a thin copper layer. This system is a 150 W three-source thermal evaporation system, typically used to evaporate metal films under high vacuum (6×10^{-6} Torr) while measuring the thickness in-situ by a thickness monitor. Thus, I can precisely control deposition rate and film thickness through this small-scale, research-level thin film deposition system. After completing the metallization, to remove Cu from unwanted areas, I lifted off the gratings in AZ NMP Rinse for 20 minutes and cleaned them with DI water, and dried them with nitrogen gas. I characterized the etched structures by scanning electron microscope (SEM) JSM-6060 (JEOL). The top and tilted view SEM images give a comprehensive understanding of the RIE process. Moreover, I used Keyence VHX-7000 digital microscope and Park NX10 Atomic Force Microscope (AFM) to provide 2D and 3D profilometer analysis from the etched grating profile.

7.3 Laser Interference Lithography (LIL) Patterning Method

The first method used for patterning the PbSe films was direct writing photoresist by μPG-101 Laser Lithography System. The capabilities of this system make it an excellent lithographic tool for research. It uses acoustic-optic modulators to adjust the laser intensity. During an exposure, only the stage moves. The substrate is held down on the stage by a vacuum and moves in the XY plane. The 10 mm head acts as a focusing objective with a resolution of 2.5 microns.

To accelerate the fabrication process, I designed a mask by MJB3 Mask Aligner to transfer the grating patterns to the sample. The mask contains several HCG designs with the smallest feature of 1 μm and the biggest feature of 4 μm. After four-second UV exposure, I baked the sample again for one minute at 110 C°. Finally, I developed it in AZ 300MIF developer for 50 seconds, washed it with DI water, and dried it using UHP nitrogen gas.

In order to reach sub-micron grating structures, I used another method named laser interference lithography. There are two common equipment architectures used in LIL: Lloyd's mirror interferometer for high-resolution applications and the dual-beam interferometer for large-area patterning [215]. I set up Lloyd's mirror interferometer in our lab. This setup consists of several components: a laser with a long coherent Gaussian beam, a lens, a pinhole, and a mirror. The mirror is positioned perpendicular to the exposed surface to create the second beam. By placing the substrate and mirror on a rotating table, the period of the grating can be precisely adjusted. Figure 7.3 shows the setup schematically. In this setting, the period (Λ) can be driven by (7.1), where θ is the angle at the intersection of the mirror and substrate, and λ is the laser wavelength.

$$\Lambda = \frac{\lambda}{2Sin(\theta)} \tag{7.1}$$

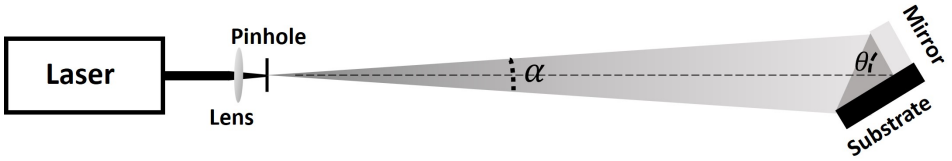

Fig. 7.3: Schematically view of Lloyd's mirror interferometer.

In this setup, the center of the beam is aligned at the intersection of the mirror and the substrate, while the Gaussian beam should be symmetrically aligned over the substrate and mirror to achieve equal intensities at the intersection. Additionally, to control any disturbances to the interference pattern caused by vibrations, the setup is mounted on a vibration-isolated table, and the rotation table is stabilized to maintain accuracy during the exposure. Furthermore, dust particles on the mirror can disrupt the interference pattern. Therefore, I used a mirror with a perfectly smooth surface. I used a CW laser (SN TopMode-405-HP) showing long coherence length with the advantage of easy exposure dose control only by the exposure time.

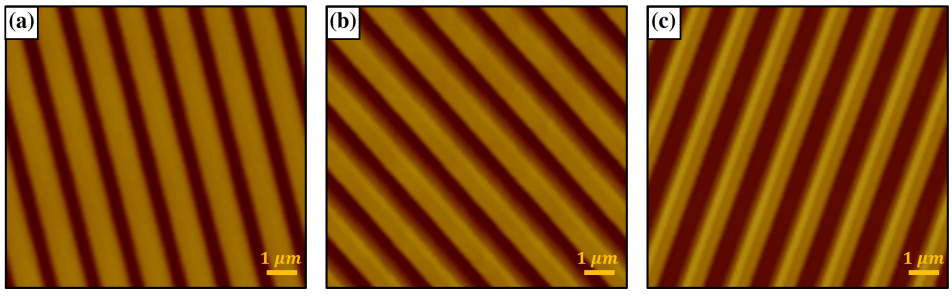

Fig. 7.4: **a)** AFM photo of the grating pattern under 15.6 mJ/cm^2 exposure dose. **b)** AFM photo of the grating pattern under 31.2 mJ/cm^2 exposure dose. **c)** AFM photo of the grating pattern under 62.4 mJ/cm^2 exposure dose.

We optimized the system by selecting a lens with a focal length of 15 mm and a pinhole with 20 μm diameter. Moreover, I optimized the power reaching the mirror/substrate intersection (1.56 mW/cm^2). Figure 7.4.a) shows an AFM photo of the photoresist pattern given by rotating angle (θ=10°) and 15.6 mJ/cm^2 exposure dose on a silicon substrate. This configuration led to a grating pattern with a period of 1.1 μm and a fill factor of 0.67, showing 0.37 μm slot width.

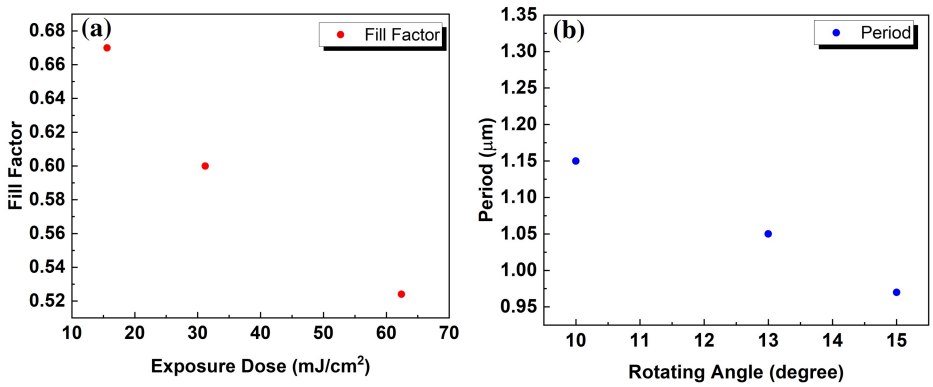

Fig. 7.5: **a)** Trend of fill factor changes under different exposure doses. **b)** Grating period size for 10°, 13°, and 15° rotating angle.

I could reach the smallest feature of 0.37 μm, while the smallest feature given by the direct lithography method was 0.7 μm. I expect that increasing the exposure dose leads to a lower fill factor. Figure 7.4.b), shows an AFM photo of the grating pattern under 31.2 mJ/cm^2 and 62.4 mJ/cm^2, respectively. Figure 7.5.a), shows the trend of fill factor changes under different exposure doses. As we can see, the fill factor decreases almost linearly by increasing the exposure dose. Moreover, I can control the grating period by the rotating angle (θ). According to (7.1), a greater angle results in smaller periods. Figure 7.5.b), shows the changes in period size according to the rotating angle (10°, 13°, and 15°).

7.4 Optimization of the RIE Dry Etching Method

Among different etching methods, one of the well-known methods is wet chemical etching. This low-cost and straightforward method provides high levels of mask selectivity [216], [217]. However, the equal etched rate in all directions, or in other words, isotropic etching, results in severe undercutting of the masking layer and makes size control challenging [218]. This issue becomes bold in micro-size components, which need high feature size control. In comparison to wet-etching, Reactive Ion Etching (RIE) and inductively coupled plasma-RIE (ICP-RIE) indicate high material selectivity and directionality [219], [220] simultaneously. Therefore, this method can be a promising candidate for the fabrication of small-size components with close pitch and high-density arrays. However, to achieve a precise etching profile with smooth sidewalls, optimizing the plasma gas phase, RF power, and process pressure are significantly important.

The DC self-bias voltage in an RIE system is a negative potential on the power electrode caused by electron bombardment. Several factors affect the DC self-bias voltage, including process pressure, RF power, and the type of gas used. The RF power applied in RIE significantly influences the etching rate and etched profile by directly impacting the DC self-bias voltage on the electrode. It has been observed that the DC self-bias voltage increases approximately linearly with an increase in RF power. On the other hand, the DC self-bias voltage decreases with increasing process pressure. The influence of process pressure on the DC self-bias voltage can be explained as follows: as process pressure increases, the mean free path of electrons decreases, resulting in a higher probability of collisions between particles. More collisions lead to increased recombination of ions and electrons, reducing the number of free electrons and ions reaching the sample chuck. Consequently, the

DC self-bias voltage decreases.

The etching rate in RIE is determined by both physical and chemical components. Higher RF power increases plasma density, leading to an increased number of reactive species for chemical etching. As a result, the etching rate increases with higher RF power. However, at higher process pressures, the decreased mean free path of electrons and ions increases the recombination of electrons and ions, significantly reducing electron density. This decrease in electron density lowers both the dissociation rate and radical density, resulting in reduced physical and chemical etching components and, thus, a decrease in the etching rate. Figure 7.6.a) shows an SEM photo of an etched grating with the optimized RF power (200 W) and process pressure (15 mTorr). In comparison, figure 7.6.b) indicates the etched profile of a non-optimized grating (350 W, 25 mTorr). The grating slot width is 2.2 μm.

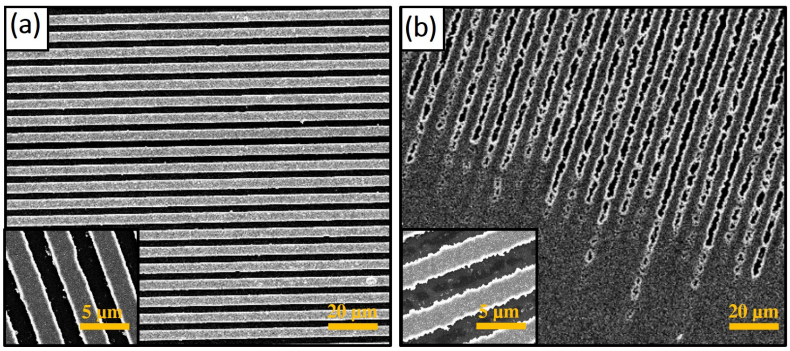

Fig. 7.6: **a)** SEM photo of the etched profile of a grating with 200 W RF power and 15 mTorr process pressure. **b)** SEM photo of the etched profile of a grating with 350 W RF power and 25 mTorr process pressure. The RIE was performed in $CH_4/H_2/Ar$ plasma atmosphere with the ratio of 10/10/5, respectively. Insets show a higher magnification of each grating.

I discovered that the developed etching recipe results in an unexpected profile irregularity and RIE-lag for sub-micron narrow-gap grating structures. I anticipate that the source of this irregularity can be the charging effect induced by charged carrier shading. The accumulated charge on the non-conductive photoresist plays a crucial role in forming this effect. Therefore, introducing a conductive layer can neutralize the accumulated charge and significantly improves the profile. To prove this theory, I introduced a thin layer of copper on the gratings. While without any conductive coating, I failed to etch gratings with a slot width of less than 1 μm; by introducing a copper layer, I succeeded in etching gratings with 0.7 μm slot width with the improved sidewall profiles. Hence, this technique enables us to fabricate sub-micron PbSe gratings with MIR device applications. In the following section, I discuss the details of this method.

7.4.1 Ion Charging Effect to Improve RIE Etched Profile

By decreasing the slot width from 4 to 2 μm, we discovered increased irregularity and RIE-lag in etched profiles. I suggest that the charging effect resulting from charged carrier shading is the main responsible mechanism for this phenomenon [221]. Charged carrier shading is a phenomenon that explains the imbalance of ion and electron currents reaching the bottom of the narrow gap [218]. It seems that the accumulated charge on the insulating photoresist builds up a positive charge at the neck of the trench, leading to the deflection of ions and causing a lower etch rate at the trench bottom. To test our hypothesis, I deposited a metallic layer on non-conductive photoresist mask layers to assist in preserving the electrical continuity in intermediate parts and prevent charging up the photoresist, resulting in a minimal shading effect. [221].

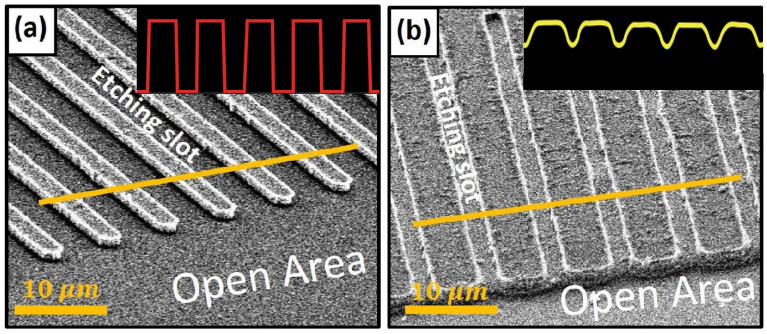

Fig. 7.7: **a)** Tilted SEM image of the etched profile of a grating with a slot width of 4 μm. The inset shows a 2D profilometry view of this grating. **b)** Tilted SEM image of the etched profile of a grating with a slot width of 2.1 μm. The inset shows a 2D profilometry view of this grating. The reference line is displayed by a solid yellow line at the grating area.

Figure 7.7.a) shows the SEM photo of the etched profile of a PbSe grating with a period of 8 μm and 50% fill factor. We can see the open area where no grating has been patterned, and slots in the grating area have been entirely etched to the substrate. The inset shows a 2D profilometer analysis given by Keyence VHX-7000. The reference line is displayed by a solid yellow line at the grating area. Figure 7.7.b) displays the SEM photo of a grating with a period of 7 μm and 70% fill factor, where the slot width has been reduced from 4 μm to 2.1 μm, compared to the figure 7.7.a). While the open area has been etched to the substrate, slots at the grating area show the RIE-lag, and the etching process has not been completed in this area. The 2D profilometer displayed in the inset shows a severe bowing effect in the narrow-slot grating.

Since the main difference between these two gratings is their slot width, I anticipate this factor plays an important role in causing the RIE-lag and the bowing effect. To test this theory, I studied the slot width impact by etching gratings with different slot sizes. I started from a grating with a slot of 4.1 μm and decreased the slot width 100 nm for each grating. Therefore I provided a set of

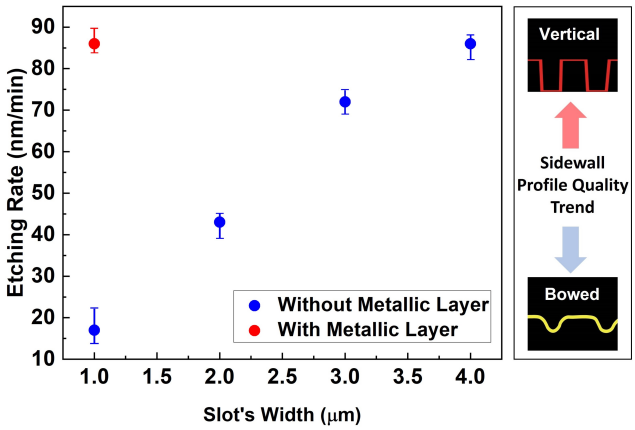

Fig. 7.8: Plot of the etching rate according to slot width changes in grating structures. The blue circles are related to the grating with no metallic layer. The red circle shows the accelerated etching rate due to the introduced metallic layer (Cu) for narrow-slot gratings. The arrows show that by increasing the etching rate, the etch profile improves.

gratings with the widest slot of 4.1 μm and the narrowest of 0.7 μm. All gratings were etched at $CH_4/H_2/Ar$ atmosphere with the ratio of 10/10/5, respectively for 700 s. I found out the bowing effect starts to be noticeable in the grating with the slot of 3 μm, and for less than 1.5 μm slot width, the grating pattern severely disordered and etching the grating with less than 1 μm slot width is practically impossible.

Figure 7.8 can give us a better understanding of the relationship between slot width and the etching rate in grating structures. The blue circles indicate the etching rate of PbSe gratings, where only insulator photoresists are used for patterning. This plot shows that by increasing the slot width from 1 μm to 4 μm, the etching rate increases almost linearly from 17 nm/min to 86 nm/min, and the etched profile improves, resulting in an ignorable bowing effect for gratings with a slot width of 4 μm.

The source of this irregularity can be the charging effect induced by charged carrier shading. Charged carrier shading is a phenomenon that explains the

imbalance of ion and electron currents reaching the bottom of the narrow gap. The primary reason for this phenomenon is related to the difference in the ion and electron angular distributions. When the pattern is exposed to a plasma, the upper side of the mask is charged up. Thus, the entering electrons are deflected, resulting in the reduction of the reaching electron to the bottom of the gap. In addition to profile irregularity, the shading effect can cause the RIE-lag. Ion deflection or translational energy reduction decreases the etch rate at the bottom of the slot.

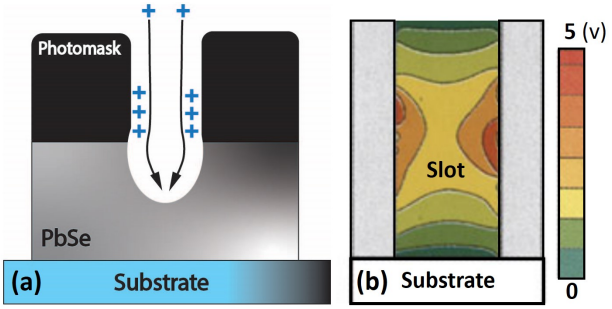

Fig. 7.9: **a)** 2D schematical view of the etched profile of a PbSe grating showing the ion-focusing effect resulting in the rounded shape of the trench's bottom. **b)** Numerical simulation of the potential contour map in the slot in a grating. The colored bar shows the potential values of the counter map [218].

As a result of the accumulated electrons on the mask, an intense electric field builds up at the edge gap in the direction of the edge line. These electrons can no longer be distributed to intermediate lines to maintain electrical continuity. Therefore, ions are mostly deflected along the edge line, etching the inner sidewall much sooner than the sidewalls of intermediate lines. This results in etching the open area faster than compacted arrays. This phenomenon mostly leads to micro trenching. However, in this study, the profilometer analysis (figure 7.7.b)) indicates the bowing effect rather than the trenching effect. Although this phenomenon can be the responsible mechanism for the RIE-lag (etching the open area faster than the grating area), it seems that another mechanism is

involved leading to the bowing effect. This mechanism can be ion-focusing. The ion-focusing mechanism can be responsible for the rounded shape of the trench bottom. Figure 7.9 can give us a better understanding of this mechanism.

Figure 7.9.a) illustrates a 2D schematical view of the etched profile of a PbSe grating showing the bowing effect. Arrows display ion current trajectory, and positive signs stand for the positively charged area. Figure 7.9.b) shows the simulated potential contour map of the slot in a grating [218]. The colored bar shows the potential values of the counter map where the red color is the most positively charged part and the dark green is the neutral part. As we can see, the positive accumulated charge on the trench's sidewall repels the ion current and forces a significant fraction of the ions to bend toward the center of the trench. The schematical view indicates evidently how the ion-focusing results in the rounded bottom, while no indication of trenching is observed. The performed numerical simulation shows how the sidewalls charged up positively (red parts show the highest positive potential).

Since the responsible mechanism for RIE-lag is accumulated charge on the photoresist, it seems that introducing a metallic layer can address this issue. The metallic layer helps to preserve the electrical continuity in intermediate parts and prevents charging up the photoresist and its consequent phenomena. I anticipate that introducing a thin metallic layer can significantly improve the etched profile in a way that fabrication of gratings with a slot width of less than 1 μm would be possible. To test this theory, I deposited a 70 nm thick copper (Cu) layer on the patterned gratings. In this study, I selected copper due to its decent electrical conductivity, straightforward deposition method, and relatively easy etching removal.

Figure 7.10.a) displays the SEM image of the etched grating without the Cu

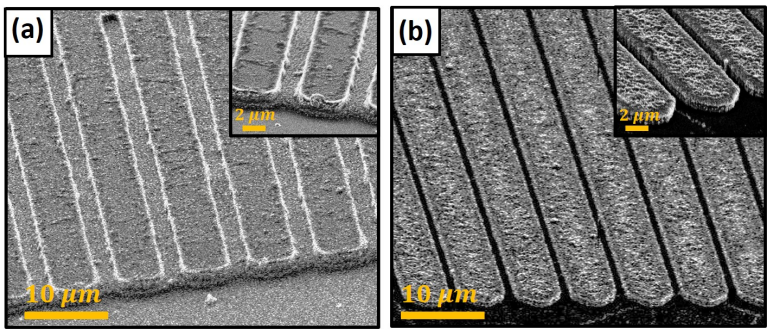

Fig. 7.10: **a)** Tilted SEM image of the etched profile of the grating without a Cu layer. The inset shows a zoomed-in view. **b)** Tilted SEM image of the etched profile of the grating with 70 nm of Cu layer. The inset shows a zoomed-in view.

layer. Figure 7.10.b) demonstrates the SEM image of the etched grating by introducing a 70 nm Cu layer on the photoresist. Insets show a zoomed-in view of each grating. The solid yellow bar shows the scales. The gratings have been etched for 700 seconds, at a process pressure of 15 mTorr, 150 watts of RIE power, with a gas mixture of $10CH_4/10H_2/5Ar$.

We can see that without applying any Cu layer (Figure 7.10.a)), the etching process of the grating with a slot width of 2.1 μm and the period of 7 μm has not been completed. While the open area has been entirely etched, due to the RIE-lag and the ion-focusing effect, the slots have not been etched completely. In comparison, by precisely the same etching process, the grating with a Cu layer has been completely etched down to the substrate, even in grooves (figure 7.10.b)). The red circle in figure 7.8 shows that depositing the metallic layer has increased the etching speed five times compared to non-conductive photoresist coating. The grating is shown in figure 7.10.b) possesses the narrowest slot (width of 0.7 μm). Etching a grating with this narrow slot width with no conductive layer was not practical in this study. The charging effect is significantly severed by narrowing down the slot width. Thus etching a grating with a slot width less than 1 μm, with our optimized receipt, is practically impossible. This observation is well-matched

with the theory expanded priory in this section.

In conclusion, this study reports an effort to etch PbSe-based sub-micron grating structures with the RIE method. RIE indicating high directionality is a suitable method to precisely etch small-size structures. Herein, effective parameters have been studied, including RF power, gas ratio, and process pressure in etching the smoothed edge profile. I noticed that a severe RIE-lag is observed by decreasing the grating size and narrowing down the slot width. While the open area is etched completely to the substrate, the etching process is unfinished in slots, and the trench's bottom indicates a rounded shape resulting from the bowing effect.

In this research, charged shading effect and ion-focusing were suggested as responsible mechanisms causing the bowing effect. Therefore, I anticipate that introducing a thin metallic layer can neutralize the accumulated charge and address this issue and its consequent phenomena. To test this theory, a thin layer of Cu (70 nm) is deposited on the grating pattern. Comparing the etched profiles of structures with and without the Cu layer showed the effectiveness of the suggested solution. By introducing a Cu layer, I succeeded in etching a grating with a slot width of 0.7 μm. However, in a case that no metallic layer is introduced, due to the severe charging effect, etching gratings with less than 1 μm slot width is impossible with our current RIE method. Therefore, I indicated that introducing a metallic layer can significantly improve the etch profile of sub-micron gratings, facilitating the fabrication of close-pitch and high-density structures with applications in enhancing the light-matter interaction.

To fabricate high Q factor gratings, the desired precision (less than 20 nm fluctuation) has remained elusive due to various technical limitations and the limited availability of advanced technologies. Despite these challenges, it is

important to acknowledge that this section serves as a foundation for future efforts aimed at achieving greater precision in micro- and nano-size grating fabrication. One potential avenue for improving fabrication accuracy is utilizing Electron Beam Lithography (EBL). By harnessing the capabilities of EBL, researchers may overcome the limitations.

In the next chapter, I provide a comprehensive summary of the studies conducted throughout this dissertation and highlight the research gaps that still exist in the field. The goal is to identify potential directions for future research and advancements in the development of fully integrated on-chip sensors for Mid-IR optical applications.

Chapter 8

Conclusion and Future Works

In conclusion, this dissertation has undertaken a comprehensive investigation into developing miniaturized advanced Mid-IR optical devices for chip-scale chemical sensing, focusing on overcoming existing obstacles in different parts, including the light source, the interaction path, and the detector.

Despite all recent advancements in Mid-IR sensing, there is room for further improvement, given cost-effective and high-performance light sources and detectors in micro-size interaction paths. To address the need for downsized and cost-effective Mid-IR sensors, this dissertation explores the integration of High Contrast gratings (HCGs) as a well-known micro-size resonate grating, enabling efficient manipulation of light propagation. The dissertation focuses on designing and optimizing three different HCG structures for developing various parts of Mid-IR sensors, including the light source, the interaction path, and the detector.

After reviewing the underlying physics of HCGs and PT-symmetric systems in Chapter 2. In Chapter 3, I studied a new theoretical approach to enhance the PbSe-based uncooled photodetector's performance in the Mid-IR wavelength region. A one-dimensional grating layer was proposed to be implemented and inserted under the PbSe photosensitive layer. Due to the resonance tuning

mechanism, this grating layer could uniquely manipulate Mid-IR light-matter interactions. It not only prevents the light transmission loss from the backside of the device but also tunes the destructive interference in the reflectance spectra, which consequently maximize the light absorption in the weak-absorbing energy band-tail region. By combining these two capabilities, it is possible to improve the detector's sensitivity significantly. With this goal, several grating parameters, including grating period, fill factor, and grating thickness, were systematically investigated and optimized using the Rigorous Coupled Wave Analysis (RCWA) method. Through the optimization, a 33% broadband absorption enhancement was achieved by using a Si(n=3.489)/SiO_2 grating on a soda-lime glass (n=1.45) substrate with the listed parameters: grating period=2.4 μm, fill factor=0.49, and thickness=1.22 μm. Apparently, this simple and effective method could practically advance the uncooled Mid-IR PbSe detector's performance.

In Chapter 4, I presented a theoretical study on using HCG designs to enhance light-gas interaction in the Mid-IR range. The optical behavior of a single layer HCG was studied under the presence of CO_2 gas. By optimizing the structure parameters, I could confine an intense electric field over the grating layer. Consequently, about 200 times light-absorption enhancement was observed. To further improve the performance, a Coupled HCG (CHCG) was proposed to introduce another vertical photonic confinement mechanism. I found that CHCG can restrict much intense light energy in the structure leading to over 600 times of light-absorption enhancement. However, it was noticed that a significant part of the concentrated electric field was still trapped in the high index areas, where the gas cannot interact. To address this issue, a modified CHCG with a thin substrate thickness was proposed. Through the thickness

optimization (T=1.149 μm), I was able to redistribute most of the light energy into the void space of the CHCG layer, which resulted in close to 1400 times of improvement. This work clearly demonstrates that using HCG for enhancing light-gas interaction is a promising approach to making on-chip gas sensing devices. Furthermore, it can also be integrated into other photonic components, e.g., fibers for advanced sensing system development.

The last Chapter of numerical designs (Chapter 5) presented a theoretical investigation of an active photonic grating of the Parity-Time (PT) symmetric architecture. The analytical study of the free-space mode propagation from the grating structure indicates the unique bifurcation property due to the PT-symmetry modulation. It is shown that both the gain/loss contrast and the lattice constant parameters are critical factors in modulating the active photonic system in between the PT-symmetry to the symmetry-broken phases. Furthermore, numerical simulations via the RCWA method discover the existence of a unique spectral singularity phenomenon in this PT grating structure, which corresponds to a non-trivial single-mode and near-zero bandwidth photonic resonant emission [24]. Also, the guiding procedure for fulfilling spectral singularity modes is found to be related to the unique formation of the scattering matrix applied in the PT-symmetric photonic gratings. This theoretical work takes a fresh look into the active PT-symmetric photonic gratings focusing on discovering new free-space emission modes rather than the commonly studied unidirectional properties, which could contribute to developing novel low-threshold and super-coherent surface-emitting devices.

Chapter 6 experimentally investigated the exploration of lead selenide (PbSe) NCs as a viable material for fabricating the designed active optical components. Herein, a new growth zone was discovered by exploring different pH values and

preparation temperatures, allowing PbSe NCs to grow on amorphous glass substrates using the OA (oriented attachment) method. The growth time and control factors, such as the complex/cations ratio in the solution, were found to influence the growth mechanisms and film deposition. A comprehensive growth model was developed, providing theoretical understanding and practical guidelines for this novel synthesis method. This advancement holds promise for the development of optoelectronic devices operating in the Mid-IR range, including solar cells, infrared detectors, photonic sensors, and light emitters.

Chapter 7 studied the required steps and techniques to fabricate sub-micron grating structures. In this chapter, the direct lithography and the interference lithography methods were discussed, indicating the capability of the interference lithography method in patterning smaller features. Then RIE etching method was optimized to etch smooth-etched-profile gratings. Moreover, it is found that as the grating size decreases and the slot width narrows, a severe RIE-lag occurs, resulting in an incomplete etching process and a rounded trench bottom due to the bowing effect. The charged shading effect and ion-focusing are identified as the mechanisms responsible for the bowing effect. To address this issue, the introduction of a thin metallic layer, specifically a 70 nm Cu layer, is proposed to neutralize the accumulated charge and mitigate the bowing effect. Experimental results demonstrate the effectiveness of introducing the Cu layer in improving the etch profile of sub-micron gratings.

Advanced nanofabrication technologies have contributed significantly to developing miniature devices and sensors. The intricate nature of nanoscale structures requires sophisticated equipment and specialized expertise, making the production of such devices a challenging and resource-intensive task. Thus, due to limited equipment, the potential of designed photonic structures has yet

to be fully explored, in this dissertation, particularly in terms of fabrication. Despite these limitations, the fabrication part of this study serves as an extension of existing research, providing a foundation for future investigations. By exploring novel fabrication approaches and techniques, I aim to overcome the current constraints and develop more efficient and cost-effective methods for manufacturing integrated chemical small-size sensors.

This dissertation represents a substantial contribution to the advancement of integrated on-chip Mid-IR gas sensors. Through an in-depth investigation of optical grating, specially HCGs, and an exploration of active and passive designs, along with the assessment of PbSe nanocrystals for fabrication purposes, this research enhances the understanding and capabilities of Mid-IR gas sensing technology. The findings and insights presented herein lay the groundwork for future research endeavors and pave the way toward practical and commercially viable on-chip Mid-IR gas sensors characterized by compact size, low weight, low power consumption, and cost-effectiveness. These features align well with emerging technologies such as the Internet of Things (IoT) and hold great promise for transformative applications in a wide range of fields.

Future Works

Interference lithography is a powerful technique to fabricate optical gratings. This cost-effective method, showing high resolution, flexibility in pattern design, and compatibility with various materials, can be the first candidate to pattern nanosize ($\approx$ 100 nm) 1D, 2D, and 3D periodic structures. There is a lot of room to enhance the performance of the interferometer setup in our lab, including optimizing the optical path smoother edge profile and using different laser sources and optical components to achieve smaller features.

Another lithography method, which has not been explored in this dissertation, is Electron-beam lithography (EBL). This method shows several advantages, including sub-10 nanometer feature sizes, creating complex and customized, patterning high-aspect-ratio structures, and precise alignment capabilities. Considering these advantages, in the future, this method can be one of the candidates for patterning nanosize structures.

In Chapter 4, I demonstrated how adding one more grating layer and designing a coupled-HCG enhanced the light absorption five times compared to only a single layer of grating. Thus, it seems that adding more grating layers improves the light-matter interaction and light absorption, consequently. Primary simulations showed that adding the third layer enhanced the light absorption about three times compared to the coupled-HCG. However, by adding the fourth layer the optimization of the structure to be matched with the peak absorption of CO_2, located at 4.3 μm, is got too complicated, and no more enhancement observed. Despite the positive impact of adding new grating layers on the light absorption enhancement, this makes the system more complicated, harder to be optimized and increases the overall size.

In Chapter 5, I showed the non-trivial properties of PT-symmetric gratings. The numerical simulation indicated near zero-bandwidth photonic emission mode at 1.463 μm coming from nontrivial high Q-factor resonance mode results from the photonic systems' special spectral singularity effect. Moreover, I discussed and indicated the PbSe-based fabricated grating in Chapter 4. By introducing a metallic layer, such as Cr, on half of the solid part of the grating, I can apply the lossy part. Figure 8.2 shows a schematic view of the potential PT-symmetry grating that will be fabricated in the future.

By numerical simulation, the thickness of the metallic layer has been optimized.

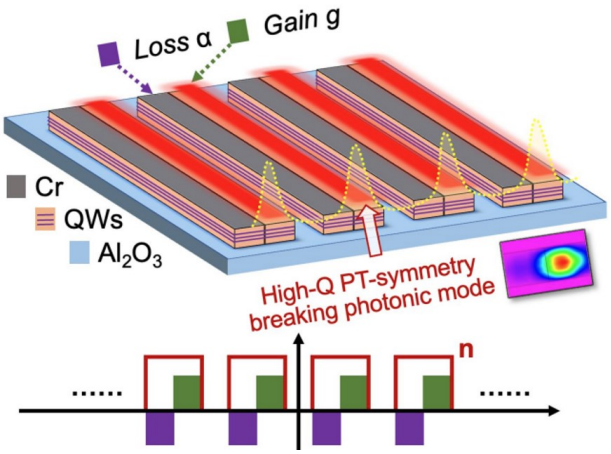

Fig. 8.1: Schematic view of the PT-symmetry grating.

Furthermore, the effect of the fluctuation coming from fabrication error has been studied by the RCWA method. However, the needed precision to activate the high-Q mode is in the range of several nanometers; thus, the suitable lithography method can be the EBL. The fabrication and test of the PT grating is one of the ongoing projects in our research group.

Moreover, by accessing advanced nanofabrication technologies, I can use the grating structures for different purposes. For instance, the primary simulations showed the potential of photonic gratings for efficient control and manipulation of light polarization. The grating structure introduces a spatially varying birefringence, which leads to polarization-dependent diffraction or reflection phenomena. By carefully designing the grating parameters, such as the period, fill factor, and grating thickness, precise control over the polarization state of light can be achieved.

In addition to progress can be achieved in the fabrication process. Characterization of the system can significantly improve the sensor's performance. Characterization of Mid-IR chemical sensors plays a vital role in evaluating their performance and suitability for various applications. For

instance, the choice of a light source depends on the specific requirements of the sensor and the desired operating conditions. The characterization process involves evaluating key parameters such as the wavelength accuracy, spectral bandwidth, power stability, and temporal characteristics of the light source. These parameters directly impact the Mid-IR sensors' sensitivity, dynamic range, and signal-to-noise ratio.

In addition to the characterization of the Mid-IR light source, the characterization of the Mid-IR detector, evaluating parameters such as responsivity, dark current, Noise Equivalent Power (NEP), and detectivity under varying environmental conditions, plays an essential role in the optimization of Mid-IR sensors. This characterization provides insights into the sensor's robustness and stability against environmental fluctuations. Understanding how temperature and humidity variations affect the sensor's output enables researchers and engineers to develop compensation techniques or implement environmental control measures to ensure accurate and reliable operation.

Moreover, characterizing the interaction path involves evaluating parameters such as absorption coefficient, path length, and interaction mechanisms. Understanding the interaction mechanisms, such as molecular vibrations, rotational transitions, or scattering processes, allows researchers to optimize the sensor's design and select appropriate detection techniques. Thus, by carefully characterizing the three core parts of a Mid-IR sensor, I can effectively assess the performance and limitations of these sensors, enabling their optimization and refinement for specific applications.

Furthermore, integrating the light source, interaction volume, and detector for miniaturizing Mid-IR sensors presents several challenges that need to be addressed. Miniaturization often necessitates compact and integrated optical

components, which may introduce limitations in terms of alignment, beam quality, and optical losses. Achieving precise alignment and maintaining optical performance becomes critical in such miniaturized systems. Another challenge lies in optimizing the detector for efficient detection of the signal generated in the interaction volume. Miniaturization often requires reducing the size of the detector, which can affect its sensitivity, dynamic range, and signal-to-noise ratio. Additionally, thermal management becomes crucial, as miniaturized systems are more susceptible to heat accumulation, leading to increased noise and potential degradation of the detector's performance.

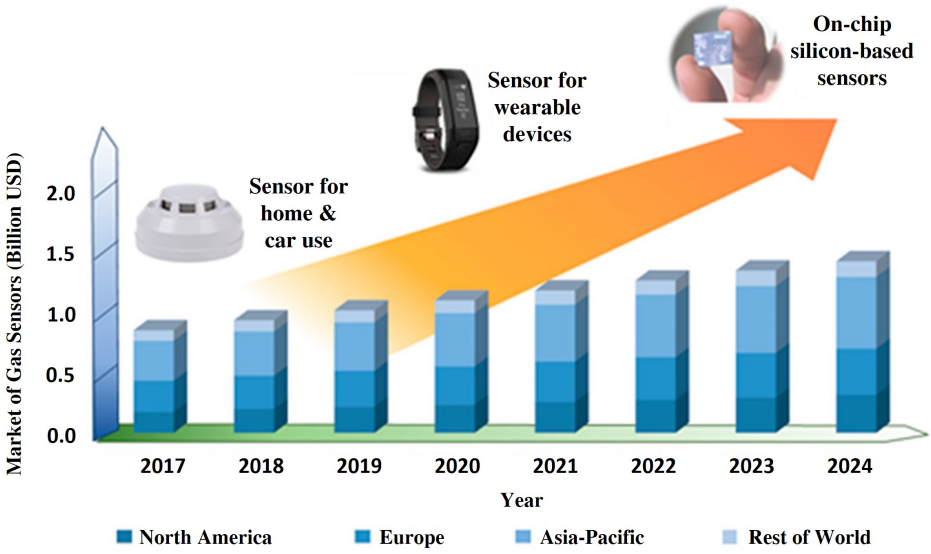

Fig. 8.2: Gas sensors' development and their global market [222].

Thus, to characterize the whole system, comprehensive testing and evaluation methodologies need to be employed. This includes measuring the system's spectral response, responsivity, noise characteristics, and stability under various operating conditions. Special attention must be given to understanding the system's limitations, such as detection limits, dynamic range, and cross-sensitivity to other analytes or environmental factors. Characterizing the

system also involves investigating its performance in realistic environments, including temperature and humidity variations, to assess its robustness and reliability. Moreover, calibration procedures and reference standards should be employed to ensure accurate and traceable measurements. The ultimate goal for the future is to realize low-cost, efficient, and miniaturized integrated Mid-IR sensors that effectively address the mentioned challenges. This advancement enables the widespread deployment of MIR sensors in various applications. Figure 8.2 indicates the speed of developing miniaturized gas sensors. It is anticipated that in a few years, the fully-integrated on-chip gas sensor will be realized.

References

[1] T. Hemati and B. Weng, "The mid-infrared photonic crystals for gas sensing applications," *Photonic Crystals—A Glimpse of the Current Research Trends*, 2019.

[2] M. Razeghi and B.-M. Nguyen, "Advances in mid-infrared detection and imaging: A key issues review," *Reports on Progress in Physics*, vol. 77, no. 8, p. 082 401, 2014.

[3] O. Spitz, P. Didier, L. Durupt, *et al.*, "Free-space communication with directly modulated mid-infrared quantum cascade devices," *IEEE Journal of Selected Topics in Quantum Electronics*, vol. 28, no. 1: Semiconductor Lasers, pp. 1–9, 2021.

[4] V. Singh, P. T. Lin, N. Patel, *et al.*, "Mid-infrared materials and devices on a si platform for optical sensing," *Science and technology of advanced materials*, 2014.

[5] I. E. Gordon, L. S. Rothman, C. Hill, *et al.*, "The hitran2016 molecular spectroscopic database," *Journal of Quantitative Spectroscopy and Radiative Transfer*, vol. 203, pp. 3–69, 2017.

[6] D. F. Swinehart, "The beer-lambert law," *Journal of chemical education*, vol. 39, no. 7, p. 333, 1962.

[7] A. A. Ismail, F. R. van de Voort, and J. Sedman, "Fourier transform infrared spectroscopy: Principles and applications," in *Techniques and instrumentation in analytical chemistry*, vol. 18, Elsevier, 1997, pp. 93–139.

[8] D. Cozzolino, W. Cynkar, N. Shah, and P. Smith, "Feasibility study on the use of attenuated total reflectance mid-infrared for analysis of compositional parameters in wine," *Food research international*, vol. 44, no. 1, pp. 181–186, 2011.

[9] C. S.-C. Yang, E Brown, U. Hommerich, S. B. Trivedi, A. C. Samuels, and A. P. Snyder, "Mid-infrared laser-induced breakdown spectroscopy emissions from alkali metal halides," *Applied Spectroscopy*, vol. 62, no. 6, pp. 714–716, 2008.

[10] D. Long, A. Fleisher, Q Liu, and J. Hodges, "Ultra-sensitive cavity ring-down spectroscopy in the mid-infrared spectral region," *Optics letters*, vol. 41, no. 7, pp. 1612–1615, 2016.

[11] S.-S. Kim, C. Young, and B. Mizaikoff, "Miniaturized mid-infrared sensor technologies," *Analytical and bioanalytical chemistry*, vol. 390, pp. 231–237, 2008.

[12] B. Weng, J. Qiu, L. Zhao, Z. Yuan, C. Chang, and Z. Shi, "Recent development on the uncooled mid-infrared pbse detectors with high detectivity," in *Quantum Sensing and Nanophotonic Devices XI*, SPIE, vol. 8993, 2014, pp. 178–185.

[13] L Küpper, H. Heise, and L. Butvina, "Novel developments in mid-ir fiber-optic spectroscopy for analytical applications," *Journal of Molecular Structure*, vol. 563, pp. 173–181, 2001.

[14] S. Law, V. Podolskiy, and D. Wasserman, "Towards nano-scale photonics with micro-scale photons: The opportunities and challenges of mid-infrared plasmonics," *Nanophotonics*, vol. 2, no. 2, pp. 103–130, 2013.

[15] R Jannesari, C Ranacher, C Consani, T Grille, and B Jakoby, "Sensitivity optimization of a photonic crystal ring resonator for gas sensing applications," *Sensors and Actuators A: Physical*, vol. 264, pp. 347–351, 2017.

[16] Y. Ma, B. Dong, B. Li, *et al.*, "Mid-infrared slow light engineering and tuning in 1-d grating waveguide," *IEEE Journal of Selected Topics in Quantum Electronics*, vol. 24, no. 6, pp. 1–8, 2018.

[17] M. Lu, H. Zhu, C. G. Bazuin, W. Peng, and J.-F. Masson, "Polymer-templated gold nanoparticles on optical fibers for enhanced-sensitivity localized surface plasmon resonance biosensors," *ACS sensors*, vol. 4, no. 3, pp. 613–622, 2019.

[18] Y. Wang, S. Zeng, G. Humbert, and H.-P. Ho, "Microfluidic whispering gallery mode optical sensors for biological applications," *Laser & Photonics Reviews*, vol. 14, no. 12, p. 2 000 135, 2020.

[19] T. Sun, S. Kan, G. Marriott, and C. Chang-Hasnain, "High-contrast grating resonators for label-free detection of disease biomarkers," *Scientific reports*, vol. 6, no. 1, pp. 1–7, 2016.

[20] A. Rostamian, "Integrated photonic devices for trace gas sensing and spectroscopy," Ph.D. dissertation, 2022.

[21] G. Finco, M. Z. Bideskan, L. Vertchenko, *et al.*, "Guided-mode resonance on pedestal and half-buried high-contrast gratings for biosensing applications," *Nanophotonics*, vol. 10, no. 17, pp. 4289–4296, 2021.

[22] T. Hemati and B. Weng, "Theoretical study of leaky-mode resonant gratings for improving the absorption efficiency of the uncooled mid-infrared photodetectors," *Journal of Applied Physics*, vol. 124, no. 5, p. 053 105, 2018.

[23] T. Hemati and B. Weng, "Theoretical design of Coupled High Contrast Grating (CHCG) waveguides to enhance CO_2 light-absorption for gas sensing applications," *Journal of Applied Physics*, vol. 125, no. 15, p. 154 502, 2019.

[24] T. Hemati, Y. Zou, and B. Weng, "High-q surface light emission from active parity-time-symmetric gratings," *Physical Review Applied*, vol. 17, no. 4, p. 044 023, 2022.

[25] T. Hemati and B. Weng, "Experimental study of the size-dependent photoluminescence emission of CBD-grown PbSe nanocrystals on glass," *Nano Express*, vol. 1, no. 1, p. 010 030, 2020.

[26] T. Hemati, X. Zhang, and B. Weng, "Towards a low-cost on-chip mid-ir gas sensing solution: Chemical synthesis of lead-salt photonic materials," in *Smart Photonic and Optoelectronic Integrated Circuits XXII*, International Society for Optics and Photonics, vol. 11284, 2020, p. 1 128 418.

[27] T. Hemati, X. Zhang, and B. Weng, "A direct oriented-attachment growth of lead-chalcogenide mid-infrared nanocrystals film on amorphous substrates," *Journal of Materials Chemistry C*, 2020.

[28] C. Palmer and E. G. Loewen, "Diffraction grating handbook," 2005.

[29] R. Kashyap, *Fiber bragg gratings*. Academic press, 2009.

[30] D. J. Schroeder, *Astronomical optics*. Elsevier, 1999.

[31] M. D. Todd, J. M. Nichols, S. T. Trickey, M. Seaver, C. J. Nichols, and L. N. Virgin, "Bragg grating-based fibre optic sensors in structural health monitoring," *Philosophical Transactions of the Royal Society A: Mathematical, Physical and Engineering Sciences*, vol. 365, no. 1851, pp. 317–343, 2007.

[32] I Nishi, T Oguchi, and K Kato, "Broad-passband-width optical filter for multi/demultiplexer using a diffraction grating and a retroreflector prism," *Electronics Letters*, vol. 21, no. 10, pp. 423–424, 1985.

[33] G Almuneau, M Condé, O Gauthier-Lafaye, V Bardinal, and C Fontaine, "High reflectivity monolithic sub-wavelength diffraction grating with gaas/alox stack," *Journal of Optics*, vol. 13, no. 1, p. 015 505, 2010.

[34] C. Shi, X. F. Zang, L. Chen, *et al.*, "Compact broadband terahertz perfect absorber based on multi-interference and diffraction effects," *IEEE Transactions on Terahertz Science and Technology*, vol. 6, no. 1, pp. 40–44, 2015.

[35] I. Kaminow, H. Weber, and E. Chandross, "Poly (methyl methacrylate) dye laser with internal diffraction grating resonator," *Applied Physics Letters*, vol. 18, no. 11, pp. 497–499, 1971.

[36] E. G. Loewen and E. Popov, *Diffraction gratings and applications*. CRC Press, 2018.

[37] C. H. Wilcox, *Scattering theory for diffraction gratings*. Springer Science & Business Media, 2012, vol. 46.

[38] S. Goeman, S. Boons, B. Dhoedt, *et al.*, "First demonstration of highly reflective and highly polarization selective diffraction gratings (giro-gratings) for long-wavelength VCSELs," *IEEE Photonics Technology Letters*, vol. 10, no. 9, pp. 1205–1207, 1998.

[39] V. Karagodsky, F. G. Sedgwick, and C. J. Chang-Hasnain, "Theoretical analysis of subwavelength high contrast grating reflectors," *Optics express*, vol. 18, no. 16, pp. 16 973–16 988, 2010.

[40] Y. Wang, "Sub-wavelength grating components for silicon-on-insulator platform," Ph.D. dissertation, University of British Columbia, 2016.

[41] R. Halir, A. OrtegaMoñux, D. Benedikovic, *et al.*, "Subwavelength-grating metamaterial structures for silicon photonic devices," *Proceedings of the IEEE*, vol. 106, no. 12, pp. 2144–2157, 2018.

[42] T. T. Wu, Y. C. Syu, S. H. Wu, *et al.*, "Sub-wavelength gan-based membrane high contrast grating reflectors," *Optics express*, vol. 20, no. 18, pp. 20 551–20 557, 2012.

[43] C. J. Chang Hasnain and W. Yang, "High-contrast gratings for integrated optoelectronics," *Advances in Optics and Photonics*, vol. 4, no. 3, pp. 379–440, 2012.

[44] Y. K. Sirenko and S Strom, "Modern theory of gratings," *Resonant Scattering: Analysis Techniques and Phenomena*, 2010.

[45] C. J. Chang Hasnain, Y. Zhou, M. C. Huang, and C. Chase, "High-contrast grating VCSELs," *IEEE Journal of Selected Topics in Quantum Electronics*, vol. 15, no. 3, pp. 869–878, 2009.

[46] M. C. Huang, Y Zhou, and C. J. Chang Hasnain, "A surface-emitting laser incorporating a high-index-contrast subwavelength grating," *Nature photonics*, vol. 1, no. 2, pp. 119–122, 2007.

[47] Y. Zhou, M. Moewe, J. Kern, M. C. Huang, and C. J. Chang Hasnain, "Surface-normal emission of a high-q resonator using a subwavelength high-contrast grating," *Optics express*, vol. 16, no. 22, pp. 17 282–17 287, 2008.

[48] Y. Wang, D. Stellinga, A. B. Klemm, C. P. Reardon, and T. F. Krauss, "Tunable optical filters based on silicon nitride high contrast gratings," *IEEE Journal of Selected Topics in Quantum Electronics*, vol. 21, no. 4, pp. 108–113, 2014.

[49] Y. Zhou, V. Karagodsky, B. Pesala, F. G. Sedgwick, and C. J. Chang Hasnain, "A novel ultra-low loss hollow-core waveguide using

subwavelength high-contrast gratings," *Optics Express*, vol. 17, no. 3, pp. 1508–1517, 2009.

[50] F. Koyama, "High contrast grating for spatial mode filtering and mode control of VCSELs," in *High Contrast Metastructures*, International Society for Optics and Photonics, vol. 8270, 2012, p. 827 005.

[51] A. Liu, W. H. Hofmann, and D. H. Bimberg, "Integrated high-contrast-grating optical sensor using guided mode," *IEEE Journal of Quantum Electronics*, vol. 51, no. 1, pp. 1–8, 2014.

[52] Y. Takashima, M. Haraguchi, and Y. Naoi, "Gan-based high-contrast grating for refractive index sensor operating blue–violet wavelength region," *Sensors*, vol. 20, no. 16, p. 4444, 2020.

[53] T. Sun, W. Yang, V. Karagodsky, W. Zhou, and C. Chang Hasnain, "Low-loss slow light inside high contrast grating waveguide," in *High Contrast Metastructures*, International Society for Optics and Photonics, vol. 8270, 2012, 82700A.

[54] T. Sun and C. Chang Hasnain, *High Contrast Grating for Optical Sensing*. eScholarship, University of California, 2015.

[55] C. M. Bender, "PT-symmetric quantum theory," in *Journal of Physics: Conference Series*, IOP Publishing, vol. 631, 2015, p. 012 002.

[56] C. M. Bender and S. Boettcher, "Real spectra in non-Hermitian Hamiltonians having PT-symmetry," *Physical Review Letters*, vol. 80, no. 24, p. 5243, 1998.

[57] Ş. Özdemir, S Rotter, F Nori, and L Yang, "Parity-time symmetry and exceptional points in photonics," *Nature materials*, vol. 18, no. 8, pp. 783–798, 2019.

[58] R. El-Ganainy, K. G. Makris, M. Khajavikhan, Z. H. Musslimani, S. Rotter, and D. N. Christodoulides, "Non-Hermitian physics and PT–symmetry," *Nature Physics*, vol. 14, no. 1, pp. 11–19, 2018.

[59] L. Feng, R. El-Ganainy, and L. Ge, "Non-Hermitian photonics based on parity–time symmetry," *Nature Photonics*, vol. 11, no. 12, pp. 752–762, 2017.

[60] C. E. Rüter, K. G. Makris, R. ElGanainy, D. N. Christodoulides, M. Segev, and D. Kip, "Observation of parity–time symmetry in optics," *Nature physics*, vol. 6, no. 3, pp. 192–195, 2010.

[61] R El-Ganainy, K. Makris, D. Christodoulides, and Z. H. Musslimani, "Theory of coupled optical pt-symmetric structures," *Optics letters*, vol. 32, no. 17, pp. 2632–2634, 2007.

[62] H. Hodaei, M. A. Miri, M. Heinrich, D. N. Christodoulides, and M. Khajavikhan, "Parity-time–symmetric microring lasers," *Science*, vol. 346, no. 6212, pp. 975–978, 2014.

[63] L. Feng, Z. J. Wong, R. Ma, Y. Wang, and X. Zhang, "Single-mode laser by parity-time symmetry breaking," *Science*, vol. 346, no. 6212, pp. 972–975, 2014.

[64] H. Hodaei, M. A. Miri, A. U. Hassan, *et al.*, "Parity-time-symmetric coupled microring lasers operating around an exceptional point," *Optics letters*, vol. 40, no. 21, pp. 4955–4958, 2015.

[65] B. Peng, Ş. K. Özdemir, F. Lei, *et al.*, "Parity–time-symmetric whispering-gallery microcavities," *Nature Physics*, vol. 10, no. 5, pp. 394–398, 2014.

[66] L. Chang, X. Jiang, S. Hua, *et al.*, "Parity–time symmetry and variable optical isolation in active–passive-coupled microresonators," *Nature photonics*, vol. 8, no. 7, pp. 524–529, 2014.

[67] B Peng, Ş. Özdemir, S Rotter, *et al.*, "Loss-induced suppression and revival of lasing," *Science*, vol. 346, no. 6207, pp. 328–332, 2014.

[68] Y. L. Xu, W. S. Fegadolli, L. Gan, *et al.*, "Experimental realization of bloch oscillations in a parity-time synthetic silicon photonic lattice," *Nature communications*, vol. 7, no. 1, pp. 1–6, 2016.

[69] K. G. Makris, R. El-Ganainy, D. N. Christodoulides, and Z. H. Musslimani, "Pt-symmetric optical lattices," *Physical Review A*, vol. 81, no. 6, p. 063 807, 2010.

[70] E. Lustig, Y. Plotnik, Z. Yang, and M. Segev, "3D parity time symmetry in 2D photonic lattices utilizing artificial gauge fields in synthetic dimensions," in *CLEO: QELS_Fundamental Science*, Optical Society of America, 2019, FTu4B–1.

[71] R. Yao, C.-S. Lee, V. Podolskiy, and W. Guo, "Electrically injected parity time–symmetric single transverse–mode lasers," *Laser & Photonics Reviews*, vol. 13, no. 1, p. 1 800 154, 2019.

[72] M. A. Miri, P. LiKamWa, and D. N. Christodoulides, "Large area single-mode parity–time-symmetric laser amplifiers," *Optics letters*, vol. 37, no. 5, pp. 764–766, 2012.

[73] X.-Y. Zhu, Y. L. Xu, Y. Zou, *et al.*, "Asymmetric diffraction based on a passive parity-time grating," *Applied Physics Letters*, vol. 109, no. 11, p. 111 101, 2016.

[74] T. Shui, W.-X. Yang, S. Liu, L. Li, and Z. Zhu, "Asymmetric diffraction by atomic gratings with optical pt symmetry in the raman-nath regime," *Physical Review A*, vol. 97, no. 3, p. 033 819, 2018.

[75] Y.-M. Liu, F. Gao, C.-H. Fan, and J.-H. Wu, "Asymmetric light diffraction of an atomic grating with pt symmetry," *Optics Letters*, vol. 42, no. 21, pp. 4283–4286, 2017.

[76] L. Feng, Y. L. Xu, W. S. Fegadolli, *et al.*, "Experimental demonstration of a unidirectional reflectionless parity-time metamaterial at optical frequencies," *Nature materials*, vol. 12, no. 2, pp. 108–113, 2013.

[77] X. Gu, R. Bai, C. Zhang, *et al.*, "Unidirectional reflectionless propagation in a non-ideal parity-time metasurface based on far field coupling," *Optics Express*, vol. 25, no. 10, pp. 11 778–11 787, 2017.

[78] Y. Huang, Y. Shen, C. Min, S. Fan, and G. Veronis, "Unidirectional reflectionless light propagation at exceptional points," *Nanophotonics*, vol. 6, no. 5, pp. 977–996, 2017.

[79] W. Chen, J. Zhang, B. Peng, Ş. K. Özdemir, X. Fan, and L. Yang, "Parity-time-symmetric whispering-gallery mode nanoparticle sensor," *Photonics Research*, vol. 6, no. 5, A23–A30, 2018.

[80] Y. C. Zhang and Y.-t. Fang, "Gas sensor based on parity-time-symmetry structure," *Journal of Nanophotonics*, vol. 12, no. 3, p. 036 005, 2018.

[81] K. G. Makris, R El-Ganainy, D. Christodoulides, and Z. H. Musslimani, "Beam dynamics in p t symmetric optical lattices," *Physical Review Letters*, vol. 100, no. 10, p. 103 904, 2008.

[82] F. A. Berezin and M Shubin, *The Schrödinger Equation*. Springer Science & Business Media, 2012, vol. 66.

[83] M. Kulishov, H. Jones, and B. Kress, "Analysis of pt-symmetric volume gratings beyond the paraxial approximation," *Optics express*, vol. 23, no. 7, pp. 9347–9362, 2015.

[84] P. Brandão, J. Nascimento, and S. Cavalcanti, "Nonparaxial electromagnetic bragg scattering in periodic media with pt symmetry," *Superlattices and Microstructures*, vol. 130, pp. 416–427, 2019.

[85] L. Feng, Z. J. Wong, R. Ma, Y. Wang, and X. Zhang, "Parity-time synthetic laser," *arXiv preprint arXiv:1405.2863*, 2014.

[86] W. Liu, M. Li, R. S. Guzzon, *et al.*, "An integrated parity-time symmetric wavelength-tunable single-mode microring laser," *Nature communications*, vol. 8, no. 1, pp. 1–6, 2017.

[87] Z. Lin, H. Ramezani, T. Eichelkraut, T. Kottos, H. Cao, and D. N. Christodoulides, "Unidirectional invisibility induced by PT–symmetric periodic structures," *Physical Review Letters*, vol. 106, no. 21, p. 213 901, 2011.

[88] L. Feng, X. Zhu, S. Yang, *et al.*, "Demonstration of a large-scale optical exceptional point structure," *Optics express*, vol. 22, no. 2, pp. 1760–1767, 2014.

[89] C. Hahn, E. K. Keshmarzi, S. H. Song, C. H. Oh, R. N. Tait, and P. Berini, "Unidirectional bragg gratings using parity-time symmetry breaking in plasmonic systems," *IEEE Journal of Selected Topics in Quantum Electronics*, vol. 22, no. 5, pp. 48–59, 2016.

[90] M. Kulishov, B. Kress, and R. Slavík, "Resonant cavities based on parity-time-symmetric diffractive gratings," *Optics Express*, vol. 21, no. 8, pp. 9473–9483, 2013.

[91] Y. L. Xu, L. Feng, M.-H. Lu, and Y.-F. Chen, "Unidirectional transmission based on a passive pt symmetric grating with a nonlinear silicon distributed bragg reflector cavity," *IEEE Photonics Journal*, vol. 6, no. 1, pp. 1–7, 2013.

[92] Y. Fei, Y.-W. Liu, D.-X. Dong, Y.-Q. Fan, and Y.-Y. Fu, "Broadband unidirectional near-zero reflection induced by logical combination of

parity-time symmetric photonic crystal," *Optics Communications*, p. 126 123, 2020.

[93] H. Cao, D. Zhao, M. Fang, *et al.*, "Unidirectional invisibility induced by complex anti-parity–time symmetric periodic lattices," *Applied Sciences*, vol. 9, no. 18, p. 3808, 2019.

[94] P. Miao, Z. Zhang, J. Sun, *et al.*, "Orbital angular momentum microlaser," *Science*, vol. 353, no. 6298, pp. 464–467, 2016.

[95] B. Lv, J. Fu, B. Wu, *et al.*, "Unidirectional invisibility induced by parity-time symmetric circuit," *Scientific reports*, vol. 7, no. 1, pp. 1–7, 2017.

[96] W. Chen, Ş. K. Özdemir, G. Zhao, J. Wiersig, and L. Yang, "Exceptional points enhance sensing in an optical microcavity," *Nature*, vol. 548, no. 7666, pp. 192–196, 2017.

[97] J. Wiersig, "Enhancing the sensitivity of frequency and energy splitting detection by using exceptional points: Application to microcavity sensors for single-particle detection," *Physical Review Letters*, vol. 112, no. 20, p. 203 901, 2014.

[98] H Jing, Ş. Özdemir, H Lü, and F. Nori, "High-order exceptional points in optomechanics," *Scientific reports*, vol. 7, no. 1, pp. 1–10, 2017.

[99] S. Zhang, X. Zhang, L Jin, and Z Song, "High-order exceptional points in supersymmetric arrays," *Physical Review A*, vol. 101, no. 3, p. 033 820, 2020.

[100] H. Hodaei, A. U. Hassan, S. Wittek, *et al.*, "Enhanced sensitivity at higher-order exceptional points," *Nature*, vol. 548, no. 7666, pp. 187–191, 2017.

[101] M. Vollmer, M. Klaus-Peter, *et al.*, *Infrared thermal imaging: fundamentals, research and applications*. John Wiley & Sons, 2017.

[102] M. Henini and M. Razeghi, *Handbook of infrared detection technologies*. Elsevier, 2002.

[103] C Sierra, M. Torquemada, G Vergara, *et al.*, "Multicolour pbse sensors for analytical applications," *Sensors and Actuators B: Chemical*, vol. 190, pp. 464–471, 2014.

[104] M. Rodrigo, F. Sánchez, M. Torquemada, *et al.*, "Polycrystalline lead selenide x–y addressed uncooled focal plane arrays," *Infrared Physics & Technology*, vol. 44, no. 4, pp. 281–287, 2003.

[105] Y Yang, H. Liu, M. Hao, and W. Shen, "Investigation on the limit of weak infrared photodetection," *Journal of Applied Physics*, vol. 110, no. 7, p. 074 501, 2011.

[106] L. Cao, J. Luo, K. Tu, L.-Q. Wang, and H. Jiang, "Generation of nano-sized core–shell particles using a coaxial tri-capillary electrospray-template removal method," *Colloids and Surfaces B: Biointerfaces*, vol. 115, pp. 212–218, 2014.

[107] J. Qiu, B. Weng, Z. Yuan, and Z. Shi, "Study of sensitization process on mid-infrared uncooled pbse photoconductive detectors leads to high detectivity," *Journal of Applied Physics*, vol. 113, no. 10, p. 103 102, 2013.

[108] B. Weng, J. Qiu, Z. Yuan, P. R. Larson, G. W. Strout, and Z. Shi, "Responsivity enhancement of mid-infrared pbse detectors using caf2 nano-structured antireflective coatings," *Applied Physics Letters*, vol. 104, no. 2, p. 021 109, 2014.

[109] E. L. Dereniak and G. D. Boreman, *Infrared detectors and systems*. Wiley, 1996.

[110] G. Bauhuis, P Mulder, E. Haverkamp, J. Huijben, and J. Schermer, "26.1% thin-film gaas solar cell using epitaxial lift-off," *Solar Energy Materials and Solar Cells*, vol. 93, no. 9, pp. 1488–1491, 2009.

[111] S. Wang, R. Magnusson, J. S. Bagby, and M. Moharam, "Guided-mode resonances in planar dielectric-layer diffraction gratings," *JOSA A*, vol. 7, no. 8, pp. 1470–1474, 1990.

[112] S. Fan and J. Joannopoulos, "Analysis of guided resonances in photonic crystal slabs," *Physical Review B*, vol. 65, no. 23, p. 235 112, 2002.

[113] R. Magnusson and M. Shokooh-Saremi, "Physical basis for wideband resonant reflectors," *Optics express*, vol. 16, no. 5, pp. 3456–3462, 2008.

[114] Y. Ding and R Magnusson, "Resonant leaky-mode spectral-band engineering and device applications," *Optics express*, vol. 12, no. 23, pp. 5661–5674, 2004.

[115] Y. Wang, Y. Huang, J. Sun, S. Pandey, and M. Lu, "Guided-mode-resonance-enhanced measurement of thin-film absorption," *Optics Express*, vol. 23, no. 22, pp. 28 567–28 573, 2015.

[116] Y Ding and R Magnusson, "Band gaps and leaky-wave effects in resonant photonic-crystal waveguides," *Optics Express*, vol. 15, no. 2, pp. 680–694, 2007.

[117] T. Khaleque, M. J. Uddin, and R. Magnusson, "Design and fabrication of broadband guided-mode resonant reflectors in te polarization," *Optics Express*, vol. 22, no. 10, pp. 12 349–12 358, 2014.

[118] M. Moharam, E. B. Grann, D. A. Pommet, and T. Gaylord, "Formulation for stable and efficient implementation of the rigorous coupled-wave analysis of binary gratings," *JOSA a*, vol. 12, no. 5, pp. 1068–1076, 1995.

[119] M. A. Kats, R. Blanchard, S. Ramanathan, and F. Capasso, "Thin-film interference in lossy, ultra-thin layers," *Optics and Photonics News*, vol. 25, no. 1, pp. 40–47, 2014.

[120] C Fischer, M. Sigrist, Q Yu, and M Seiter, "Photoacoustic monitoring of trace gases by use of a diode-based difference frequency laser source," *Optics Letters*, vol. 26, no. 20, pp. 1609–1611, 2001.

[121] B. Buszewski, M. Kesy, T. Ligor, and A. Amann, "Human exhaled air analytics: Biomarkers of diseases," *Biomedical chromatography*, vol. 21, no. 6, pp. 553–566, 2007.

[122] J Riegel, H Neumann, and H.-M. Wiedenmann, "Exhaust gas sensors for automotive emission control," *Solid State Ionics*, vol. 152, pp. 783–800, 2002.

[123] J. Hodgkinson and R. P. Tatam, "Optical gas sensing: A review," *Measurement science and technology*, vol. 24, no. 1, p. 012 004, 2012.

[124] M. Quan, J. Tian, and Y. Yao, "Ultra-high sensitivity fabry–perot interferometer gas refractive index fiber sensor based on photonic crystal fiber and vernier effect," *Optics letters*, vol. 40, no. 21, pp. 4891–4894, 2015.

[125] J. Wang, Y. Li, Z. Wang, J. Han, N. Huang, and H. Liu, "Broadband wavelength conversion in hydrogenated amorphous silicon waveguide with

silicon nitride layer," *Journal of Modern optics*, vol. 65, no. 1, pp. 1–7, 2018.

[126] J. Wang and L. Wang, "Carbon dioxide gas sensor derived from a 547-hole microstructured polymer optical fiber preform," *Optics letters*, vol. 35, no. 19, pp. 3270–3272, 2010.

[127] W. Y. Peng, C. S. Goldenstein, R. M. Spearrin, J. B. Jeffries, and R. K. Hanson, "Single-ended mid-infrared laser-absorption sensor for simultaneous in situ measurements of h 2 o, co 2, co, and temperature in combustion flows," *Applied optics*, vol. 55, no. 33, pp. 9347–9359, 2016.

[128] R. Tao, P. Ma, X. Wang, P. Zhou, and Z. Liu, "Study of wavelength dependence of mode instability based on a semi-analytical model," *IEEE Journal of quantum electronics*, vol. 51, no. 8, pp. 1–6, 2015.

[129] G. Korotcenkov, *Handbook of humidity measurement, volume 1: spectroscopic methods of humidity measurement*. CRC Press, 2018.

[130] U. Platt, J. Stutz, U. Platt, and J. Stutz, *Differential absorption spectroscopy*. Springer, 2008.

[131] V. Selvakumar, L Sujatha, and R Sundar, "Design analysis and electrical characterisation of porous silicon structure for sensor applications," *Sensor letters*, vol. 16, no. 3, pp. 188–193, 2018.

[132] D. Pergande, T. M. Geppert, A. v. Rhein, *et al.*, "Miniature infrared gas sensors using photonic crystals," *Journal of Applied Physics*, vol. 109, no. 8, p. 083 117, 2011.

[133] A. K. Goyal, H. S. Dutta, and S. Pal, "Recent advances and progress in photonic crystal-based gas sensors," *Journal of Physics D: Applied Physics*, vol. 50, no. 20, p. 203 001, 2017.

[134] M. Marciniak, M. Gebski, M. Dems, and T. Czyszanowski, "Subwavelength high contrast gratings as optical sensing elements," *Scientific Bulletin of the Lodz University of Technology Physics No. 1219, Vol. 38, Wydawnictwo Politechniki Łódzkiej, Łódź 2017, ISSN 1505-1013, e-ISSN 2449-982X, doi: 10.34658/physics. 2017.38.*, 2017.

[135] S. Zheng, M. Ghandehari, and J. Ou, "Photonic crystal fiber long-period grating absorption gas sensor based on a tunable erbium-doped fiber ring laser," *Sensors and Actuators B: Chemical*, vol. 223, pp. 324–332, 2016.

[136] X. Wei and S. M. Weiss, "Guided mode biosensor based on grating coupled porous silicon waveguide," *Optics express*, vol. 19, no. 12, pp. 11 330–11 339, 2011.

[137] K. Li, N. Zhang, N. M. Y. Zhang, G. Liu, T. Zhang, and L. Wei, "Ultrasensitive measurement of gas refractive index using an optical nanofiber coupler," *Optics letters*, vol. 43, no. 4, pp. 679–682, 2018.

[138] Á. González-Vila, A. Ioannou, M. Loyez, M. Debliquy, D. Lahem, and C. Caucheteur, "Surface plasmon resonance sensing in gaseous media with optical fiber gratings," *Optics letters*, vol. 43, no. 10, pp. 2308–2311, 2018.

[139] K Tiefenthaler and W Lukosz, "Grating couplers as integrated optical humidity and gas sensors," *Thin Solid Films*, vol. 126, no. 3-4, pp. 205–211, 1985.

[140] Y. Wu, B. Yao, A. Zhang, *et al.*, "Graphene-coated microfiber bragg grating for high-sensitivity gas sensing," *Optics letters*, vol. 39, no. 5, pp. 1235–1237, 2014.

[141] M Folke, L Cernerud, M Ekström, and B Hok, "Non-invasive respiratory monitoring using long-period fiber grating sensors," *Med. Biol. Eng. Comput.*, vol. 41, pp. 377–383, 2003.

[142] S. Neethirajan, D. Jayas, and S. Sadistap, "Carbon dioxide (co 2) sensors for the agri-food industry—a review," *Food and Bioprocess Technology*, vol. 2, pp. 115–121, 2009.

[143] K. Wakatsuki, S. P. Fuss, A. Hamins, and M. R. Nyden, "A technique for extrapolating absorption coefficient measurements to high temperatures," *Proceedings of the Combustion Institute*, vol. 30, no. 1, pp. 1565–1573, 2005.

[144] J. D. Joannopoulos, S. G. Johnson, J. N. Winn, and R. D. Meade, "Molding the flow of light," *Princet. Univ. Press. Princeton, NJ [ua]*, 2008.

[145] V. R. Almeida, Q. Xu, C. A. Barrios, and M. Lipson, "Guiding and confining light in void nanostructure," *Optics letters*, vol. 29, no. 11, pp. 1209–1211, 2004.

[146] M.-C. Tien, J. F. Bauters, M. J. Heck, D. T. Spencer, D. J. Blumenthal, and J. E. Bowers, "Ultra-high quality factor planar si 3 n 4 ring resonators on si substrates," *Optics express*, vol. 19, no. 14, pp. 13 551–13 556, 2011.

[147] O. Painter, J Vučković, and A. Scherer, "Defect modes of a two-dimensional photonic crystal in an optically thin dielectric slab," *JOSA B*, vol. 16, no. 2, pp. 275–285, 1999.

[148] B. C. Kress and P. Meyrueis, *Applied digital optics: from micro-optics to nanophotonics*. John Wiley & Sons, 2009.

[149] C. F. Mateus, M. C. Huang, Y. Deng, A. R. Neureuther, and C. J. Chang-Hasnain, "Ultrabroadband mirror using low-index cladded subwavelength grating," *IEEE Photonics Technology Letters*, vol. 16, no. 2, pp. 518–520, 2004.

[150] D. Rosenblatt, A. Sharon, and A. A. Friesem, "Resonant grating waveguide structures," *IEEE Journal of Quantum electronics*, vol. 33, no. 11, pp. 2038–2059, 1997.

[151] W.-P. Huang, "Coupled-mode theory for optical waveguides: An overview," *JOSA A*, vol. 11, no. 3, pp. 963–983, 1994.

[152] N. Picqué and T. W. Hänsch, "Mid-ir spectroscopic sensing," *Optics and Photonics News*, vol. 30, no. 6, pp. 26–33, 2019.

[153] P. Karioja, T. Alajoki, M. Cherchi, *et al.*, "Multi-wavelength mid-ir light source for gas sensing," in *Photonic Instrumentation Engineering IV*, SPIE, vol. 10110, 2017, pp. 194–202.

[154] T. Jin, J. Zhou, and P. T. Lin, "Real-time and non-destructive hydrocarbon gas sensing using mid-infrared integrated photonic circuits," *RSC advances*, vol. 10, no. 13, pp. 7452–7459, 2020.

[155] M. Brandstetter, A. Genner, K. Anic, and B. Lendl, "Tunable mid-ir lasers: A new avenue to robust and versatile physical chemosensors," *Procedia Engineering*, vol. 5, pp. 1001–1004, 2010.

[156] T. J. Berg *et al.*, "Compact, mid-infrared laser source for remote sensing of gas effluents," Ph.D. dissertation, Montana State University-Bozeman, College of Engineering, 2009.

[157] A. Lochbaum, Y. Fedoryshyn, A. Dorodnyy, U. Koch, C. Hafner, and J. Leuthold, "On-chip narrowband thermal emitter for mid-ir optical gas sensing," *ACS photonics*, vol. 4, no. 6, pp. 1371–1380, 2017.

[158] K. Pierściński, A. Kuźmicz, D. Pierścińska, *et al.*, "Optimization of cavity designs of tapered alinas/ingaas/inp quantum cascade lasers emitting at 4.5 μm," *IEEE Journal of Selected Topics in Quantum Electronics*, vol. 25, no. 6, pp. 1–9, 2019.

[159] O. Malis, C. Gmachl, D. L. Sivco, L. N. Pfeiffer, A. M. Sergent, and K. W. West, "The quantum cascade laser: A versatile high-power semiconductor laser for mid-infrared applications," *Bell Labs Technical Journal*, vol. 10, no. 3, pp. 199–214, 2005.

[160] C. Zheng, M. Pi, F. Song, *et al.*, "Recent progress in infrared absorption spectroscopy for gas sensing with discrete optics, hollow-core fibers and on-chip waveguides," *Journal of Lightwave Technology*, 2023.

[161] E. Shim, A. Gil-Molina, O. Westreich, *et al.*, "Tunable single-mode chip-scale mid-infrared laser," *Communications Physics*, vol. 4, no. 1, p. 268, 2021.

[162] Q. Cao, F. X. Kärtner, and G. Chang, "Towards high power longwave mid-ir frequency combs: Power scalability of high repetition-rate difference-frequency generation," *Optics express*, vol. 28, no. 2, pp. 1369–1384, 2020.

[163] F. Gao, Y. M. Liu, X. D. Tian, C. L. Cui, and J. H. Wu, "Intrinsic link of asymmetric reflection and diffraction in non-Hermitian gratings," *Optics express*, vol. 26, no. 26, pp. 33 818–33 829, 2018.

[164] M. Kulishov and B. Kress, "Free space diffraction on active gratings with balanced phase and gain/loss modulations," *Optics express*, vol. 20, no. 28, pp. 29 319–29 328, 2012.

[165] M. Kulishov, H. Jones, and B. Kress, "Analysis of pt-symmetric volume gratings beyond the paraxial approximation," *Optics express*, vol. 23, no. 7, pp. 9347–9362, 2015.

[166] T. K. Gaylord and M. Moharam, "Analysis and applications of optical diffraction by gratings," *Proceedings of the IEEE*, vol. 73, no. 5, pp. 894–937, 1985.

[167] M. Berry and D. O'Dell, "Diffraction by volume gratings with imaginary potentials," *Journal of Physics A: Mathematical and General*, vol. 31, no. 8, p. 2093, 1998.

[168] M. Berry, "Lop-sided diffraction by absorbing crystals," *Journal of Physics A: Mathematical and General*, vol. 31, no. 15, p. 3493, 1998.

[169] L. Dong, C. Huang, and W. Qi, "Symmetry breaking and restoration of symmetric solitons in partially parity-time-symmetric potentials," *Nonlinear Dynamics*, vol. 98, no. 3, pp. 1701–1708, 2019.

[170] J. Yang, "Symmetry breaking of solitons in one-dimensional parity-time-symmetric optical potentials," *Optics letters*, vol. 39, no. 19, pp. 5547–5550, 2014.

[171] B. Zhu, Q. J. Wang, and Y. D. Chong, "Laser-mode bifurcations induced by pt-breaking exceptional points," *Physical Review A*, vol. 99, no. 3, p. 033 829, 2019.

[172] W. E. Hayenga, H. Garcia-Gracia, E. S. Cristobal, *et al.*, "Electrically pumped microring parity-time-symmetric lasers," *Proceedings of the IEEE*, vol. 108, no. 5, pp. 827–836, 2019.

[173] T. Hasenberg, R. Miles, A. Kost, and L West, "Recent advances in sb-based midwave-infrared lasers," *IEEE journal of quantum electronics*, vol. 33, no. 8, pp. 1403–1406, 1997.

[174] M Rattunde, J Schmitz, C Mermelstein, R Kiefer, and J Wagner, "Iii-sb-based type-i qw diode lasers," in *Mid-infrared semiconductor optoelectronics*, Springer, 2006, pp. 131–157.

[175] M Eibelhuber, T Schwarzl, G Springholz, and W Heiss, "Lead salt microdisk lasers operating in continuous wave mode at 5.3 μ m wavelength," *Applied Physics Letters*, vol. 94, no. 2, p. 021 118, 2009.

[176] B. Weng, J. Ma, L. Wei, J. Xu, G. Bi, and Z. Shi, "Mid-infrared surface-emitting photonic crystal microcavity light emitter on silicon," *Applied Physics Letters*, vol. 97, no. 23, p. 231 103, 2010.

[177] B. Weng, J. Qiu, and Z. Shi, "Continuous-wave mid-infrared photonic crystal light emitters at room temperature," *Applied Physics B*, vol. 123, no. 1, p. 29, 2017.

[178] W. Hunter, "Diffraction gratings and applications, by erwin g. loewen and evgeny popov," *Optics & Photonics News*, vol. 8, no. 12, pp. 52–53, 1997.

[179] A. Mostafazadeh, "Physics of spectral singularities," in *Geometric Methods in Physics*, Springer, 2015, pp. 145–165.

[180] L. Chaos-Cador and G. García-Calderón, "Resonant states for complex potentials and spectral singularities," *Physical Review A*, vol. 87, no. 4, p. 042 114, 2013.

[181] A. Mostafazadeh and H. Mehri-Dehnavi, "Spectral singularities, biorthonormal systems and a two-parameter family of complex point interactions," *Journal of Physics A: Mathematical and Theoretical*, vol. 42, no. 12, p. 125 303, 2009.

[182] C. Linton, *Wave propagation. from electrons to photonic crystals and left-handed materials, by p. markoš and cm soukoulis: Scope: Textbook. level: Final year undergraduates and first year postgraduates*, 2009.

[183] Y. Chong, L. Ge, and A. D. Stone, "Pt-symmetry breaking and laser-absorber modes in optical scattering systems," *Physical Review Letters*, vol. 106, no. 9, p. 093 902, 2011.

[184] Y. Chong, L. Ge, H. Cao, and A. D. Stone, "Coherent perfect absorbers: Time-reversed lasers," *Physical review letters*, vol. 105, no. 5, p. 053 901, 2010.

[185] D. G. Baranov, A. Krasnok, T. Shegai, A. Alù, and Y. Chong, "Coherent perfect absorbers: Linear control of light with light," *Nature Reviews Materials*, vol. 2, no. 12, p. 17 064, 2017.

[186] A. Mostafazadeh, "Resonance phenomenon related to spectral singularities, complex barrier potential, and resonating waveguides," *Physical Review A*, vol. 80, no. 3, p. 032 711, 2009.

[187] A. Mostafazadeh, "Optical spectral singularities as threshold resonances," *Physical Review A*, vol. 83, no. 4, p. 045 801, 2011.

[188] S. C. Hagness and A. Taflove, "Computational electrodynamics: The finite-difference time-domain method," *Norwood, MA: Artech House*, 2000.

[189] M. R. Foreman, J. D. Swaim, and F. Vollmer, "Whispering gallery mode sensors," *Advances in optics and photonics*, vol. 7, no. 2, pp. 168–240, 2015.

[190] D. T. Spencer, J. F. Bauters, M. J. Heck, and J. E. Bowers, "Integrated waveguide coupled si 3 n 4 resonators in the ultrahigh-q regime," *Optica*, vol. 1, no. 3, pp. 153–157, 2014.

[191] X. Ji, F. A. Barbosa, S. P. Roberts, *et al.*, "Ultra-low-loss on-chip resonators with sub-milliwatt parametric oscillation threshold," *Optica*, vol. 4, no. 6, pp. 619–624, 2017.

[192] R. Bogue, "Recent developments in mems sensors: A review of applications, markets and technologies," *Sensor review*, 2013.

[193] M. S. Vitiello, G. Scalari, B. Williams, and P. De Natale, "Quantum cascade lasers: 20 years of challenges," *Optics express*, vol. 23, no. 4, pp. 5167–5182, 2015.

[194] I. Vurgaftman, R Weih, M Kamp, *et al.*, "Interband cascade lasers," *Journal of Physics D: Applied Physics*, vol. 48, no. 12, p. 123 001, 2015.

[195] Y Bai, S Slivken, S. Darvish, and M Razeghi, "Room temperature continuous wave operation of quantum cascade lasers with 12.5% wall plug efficiency," *Applied Physics Letters*, vol. 93, no. 2, p. 021 103, 2008.

[196] M Kim, C. Canedy, W. Bewley, *et al.*, "Interband cascade laser emitting at λ= 3.75 μ m in continuous wave above room temperature," *Applied physics letters*, vol. 92, no. 19, p. 191 110, 2008.

[197] L. Zhao, J. Qiu, B. Weng, C. Chang, Z. Yuan, and Z. Shi, "Understanding sensitization behavior of lead selenide photoconductive detectors by charge separation model," *Journal of Applied Physics*, vol. 115, no. 8, p. 084 502, 2014.

[198] C. Jagadish, S. Gunapala, and D. Rhiger, *Advances in infrared photodetectors*. Elsevier, 2011.

[199] P. Findlay, C. Pidgeon, R Kotitschke, *et al.*, "Auger recombination dynamics of lead salts under picosecond free-electron-laser excitation," *Physical Review B*, vol. 58, no. 19, p. 12 908, 1998.

[200] B. Weng, L. Li, J. Qiu, and Z. Shi, "Recent development of iv-vi mid-infrared photonic crystal laser on silicon," in *2012 Symposium on Photonics and Optoelectronics*, IEEE, 2012, pp. 1–3.

[201] S. Gorer, A. Albu-Yaron, and G. Hodes, "Chemical solution deposition of lead selenide films: A mechanistic and structural study," *Chemistry of materials*, vol. 7, no. 6, pp. 1243–1256, 1995.

[202] F. Cheng, L. Lian, L. Li, *et al.*, "Hybrid growth modes of pbse nanocrystals with oriented attachment and grain boundary migration," *Advanced Science*, vol. 6, no. 9, p. 1 802 202, 2019.

[203] T. Templeman, S. Sengupta, N. Maman, *et al.*, "Oriented attachment: A path to columnar morphology in chemical bath deposited pbse thin films," *Crystal Growth & Design*, vol. 18, no. 2, pp. 1227–1235, 2018.

[204] M Shandalov and Y Golan, "Microstructure and morphology evolution in chemical solution deposited semiconductor films: 3. pbse on gaas vs. si substrate," *The European Physical Journal-Applied Physics*, vol. 31, no. 1, pp. 27–30, 2005.

[205] M Shandalov and Y Golan, "Microstructure and morphology evolution in chemical solution deposited PbSe films on gaas (100)," *The European Physical Journal Applied Physics*, vol. 24, no. 1, pp. 13–20, 2003.

[206] M Shandalov and Y Golan, "Microstructure and morphology evolution in chemical solution deposited semiconductor films: 2. PbSe on as face of gaas (111)," *The European Physical Journal Applied Physics*, vol. 28, no. 1, pp. 51–57, 2004.

[207] G. Hodes, *Chemical solution deposition of semiconductor films*. CRC press, 2002.

[208] S. Pawar, J. Shaikh, R. Devan, *et al.*, "Facile and low cost chemosynthesis of nanostructured PbS with tunable optical properties," *Applied Surface Science*, vol. 258, no. 5, pp. 1869–1875, 2011.

[209] K. Saruwatari, J. Akai, Y. Fukumori, N. Ozaki, H. Nagasawa, and T. Kogure, "Crystal orientation analyses of biominerals using kikuchi patterns in tem," *Journal of Mineralogical and Petrological Sciences*, vol. 103, no. 1, pp. 16–22, 2007.

[210] W. Zhou and Z. L. Wang, *Scanning microscopy for nanotechnology: techniques and applications*. Springer science & business media, 2007.

[211] P. Makuła, M. Pacia, and W. Macyk, *How to correctly determine the band gap energy of modified semiconductor photocatalysts based on uv–vis spectra*, 2018.

[212] J. A. Russell, "Measurement of optical bandgap energies of semiconductors," 2011.

[213] T. Templeman, M. Biton, T. Safrani, M. Shandalov, E. Yahel, and Y. Golan, "Chemically deposited pbse thin films: Factors deterring reproducibility in the early stages of growth," *CrystEngComm*, vol. 16, no. 46, pp. 10 553–10 559, 2014.

[214] G. Yang and B. Weng, "Reactive ion etching of pbse thin films in ch4/h2/ar plasma atmosphere," *Materials Science in Semiconductor Processing*, vol. 124, p. 105 596, 2021.

[215] H. van Wolferen and L. Abelmann, "Laser interference lithography," *Lithography: Principles, processes and materials*, pp. 133–148, 2011.

[216] W. Wu, P Rezai, H. Hsu, and P. Selvaganapathy, "Materials and methods for the microfabrication of microfluidic biomedical devices," in *Microfluidic devices for biomedical applications*, Elsevier, 2013, pp. 3–62.

[217] D Zhuang and J. Edgar, "Wet etching of gan, aln, and sic: A review," *Materials Science and Engineering: R: Reports*, vol. 48, no. 1, pp. 1–46, 2005.

[218] R. J. Shul and S. J. Pearton, *Handbook of advanced plasma processing techniques*. Springer Science & Business Media, 2011.

[219] M. Huff, "Recent advances in reactive ion etching and applications of high-aspect-ratio microfabrication," *Micromachines*, vol. 12, no. 8, p. 991, 2021.

[220] S. Tachi, K. Tsujimoto, and S. Okudaira, "Low-temperature reactive ion etching and microwave plasma etching of silicon," *Applied physics letters*, vol. 52, no. 8, pp. 616–618, 1988.

[221] T. Hemati, G. Yang, and B. Weng, "Study of ion charging effect to improve reactive-ion-etching profile of pbse grating structures," *Available at SSRN 4365925*,

[222] J. Wu, G. Yue, W. Chen, *et al.*, "On-chip optical gas sensors based on group-iv materials," *ACS photonics*, vol. 7, no. 11, pp. 2923–2940, 2020.

Appendix

Journal Papers

[1] **T. Hemati** and B. Weng, "The mid-infrared photonic crystals for gas sensing applications," Photonic Crystals—A Glimpse of the Current Research Trends, 2019

[2] **T. Hemati** and B. Weng, "Theoretical study of leaky-mode resonant gratings for improving the absorption efficiency of the uncooled mid-infrared photodetectors," Journal of Applied Physics, vol. 124, no. 5, p. 053 105, 2018.

[3] **T. Hemati** and B. Weng, "Theoretical design of Coupled High Contrast Grating (CHCG) waveguides to enhance CO2 light-absorption for gas sensing applications," Journal of Applied Physics, vol. 125, no. 15, p. 154 502, 2019.

[4] **T. Hemati** and B. Weng, "Experimental study of the size-dependent photoluminescence emission of CBD-grown PbSe nanocrystals on glass," Nano Express, vol. 1, no. 1, p. 010 030, 2020.

[5] **T. Hemati**, X. Zhang, and B. Weng, "A direct oriented-attachment growth of lead-chalcogenide mid-infrared nanocrystals film on amorphous substrates," Journal of Materials Chemistry C, 2020.

[6] **T. Hemati**, Y. Zou, and B.Weng, "High-q surface light emission from active parity-time-symmetric gratings," Physical Review Applied, vol. 17, no. 4, p. 044 023, 2022.

[7] **T. Hemati**, G. Yang, and B. Weng, "Study of ion charging effect to improve reactive-ion-etching profile of pbse grating structures," Available at SSRN 4365925,

Conferences and Presentations

[1] **T. Hemati**, X. Zhang, and B. Weng, "Towards a low-cost on-chip mid-ir gas sensing solution: Chemical synthesis of lead-salt photonic materials," in Smart Photonic and Optoelectronic Integrated Circuits XXII, International Society for Optics and Photonics, vol. 11284, 2020, p. 1 128 418.

[2] **T. Hemati**. "Active Parity Time(PT)-Symmetric Diffraction Gratings" The Annual OKPVRI Symposium, Norman, OK. April 2022. (Poster Presentation)

[3] **T. Hemati**. "PT-Symmetric Active Gratings – A New Solution for Surface-Emitting Lasers." 65th Annual SVC Technical Conference, Virtual. May 2022. (Oral Presentation)

[4] **T. Hemati**. "Parity Time High Contrast Gratings (PT-HCGs): A New Platform For Integrated Thin Film Gas Sensors." 64th Annual SVC Technical Conference, Virtual. May 2021. (Oral Presentation)

[5] **T. Hemati**. "Parity Time High Contrast Gratings (PT-HCGs): Oriented Growth of Lead Selenide (PbSe) Nanocrystals (NCs) For Mid-Infrared Photodetector Applications." 19th International Conference on Luminescence (ICL 2020), Virtual. July 2021. (Oral Presentation)

[6] **T. Hemati**. "Theoretical Design of Coupled High Contrast Grating (CHCG) Waveguides to Enhance CO_2 Light-Absorption for Gas Sensing Applications." The Annual OKPVRI Symposium, Stillwater, OK. April 2019. (Poster Presentation)

[7] **T. Hemati**. "Numerical Design of High Contrast Grating Couplers as an

Absorption-Based Optical Gas Sensor." Annual GCoE Graduate Student Poster Fair, Norman, OK. October 2018. (Poster Presentation)